CHARACTERIZING THE CELLULAR CONSEQUENCES OF CENTROSOME LOSS: DISCOVERY OF A MITOTIC SURVEILLANCE PATHWAY

by

Bram G. Lambrus

A dissertation submitted to Johns Hopkins University in conformity with the requirements for the degree of Doctor of Philosophy.

Baltimore, Maryland

February, 2019

Abstract

Centrosomes are the major microtubule-organizing centers of the cell, and play a key role in organizing the bipolar mitotic spindle. Precise regulation of centrosome number is therefore critical for accurate chromosome segregation and the maintenance of genomic integrity. The consequences of centrosome loss, however, have been difficult to study due to a lack of specific tools that allow persistent and reversible centrosome depletion. In the first chapter of this thesis, we combined gene targeting with an auxin-inducible degradation system to achieve rapid, titratable, and reversible control of Polo-like kinase 4 (Plk4), a master regulator of centrosome biogenesis. Depletion of Plk4 led to a failure of centrosome duplication that, unexpectedly, produced an irreversible cell cycle arrest within a few divisions. This arrest was not a result of a prolonged mitosis, chromosome segregation errors or cytokinesis failure. Depleting p53 allowed cells that failed centrosome duplication to proliferate indefinitely, indicating the presence of a p53-dependent surveillance mechanism that protects against genome instability by preventing cell growth following centrosome duplication failure. However, the mechanism by which p53 is activated in response to centrosome loss was unknown.

In the second chapter, we describe how we performed a genome-wide CRISPR/Cas9 knockout screens to identify a USP28-53BP1-p53-p21 signaling axis at the core of the centrosome surveillance pathway. We show that USP28 and 53BP1 act to stabilize p53 following centrosome loss and demonstrate this function to be independent of their previously characterized role in the DNA damage response. Surprisingly, the USP28-53BP1-

p53-p21 signaling pathway is also required to arrest cell growth following a prolonged prometaphase. We therefore propose that centrosome loss or a prolonged mitosis activate a common signaling pathway that acts to prevent the growth of cells with an increased propensity for mitotic errors.

Notably, most cancer cells have a disrupted p53 or p21 pathway, which allows them to proliferate indefinitely in the absence of centrosomes. In the last chapter of this thesis, we illustrate an exception to this trend, identifying a subset of breast cancers that exhibit profound sensitivity to centrosome loss that is independent of the mitotic surveillance pathway. We find this sensitivity to be dependent on the overexpression of TRIM37, an E3 ubiquitin ligase encoded within the 17q23 amplicon found in this subset of breast cancers. Timelapse studies show that centrosome depletion in these cells leads to dramatically prolonged mitoses that largely end in mitotic slippage. Subsequent analyses show that pericentriolar material (PCM) is depleted when TRIM37 is overexpressed, and that this suppresses the ability of these cells to organize a bipolar mitotic spindle through compensating, non-centrosomal pathways. Together, these results reveal a synthetic lethal vulnerability in breast cancers harboring the 17q23 amplicon that could be exploited therapeutically. In summary, this thesis describes the development of precise tools with which to study centrosome depletion, and reports the cellular consequences of centrosome loss in distinct cellular contexts.

Primary Reader: Andrew Holland, Ph.D.

Secondary Reader: Seth Margolis, Ph.D.

Acknowledgements

I would first and foremost like to acknowledge my thesis advisor, Dr. Andrew Holland. It has been an incredible delight and privilege to join the lab at its inception and work so closely with Andrew. His intellectual energy and enthusiasm has been a regular source of inspiration – whether exercised while poring over data together, or during philosophical discussions about the state of science and society, his shared insights and curiosity have continually motivated me and enhanced the caliber of my critical thinking. Of course, his mentorship also extends beyond knowledge transmission: Andrew has actively sought to provide a wealth of opportunities to collaborate, establish new techniques in the lab, apply for honors, and present our work in various settings. These opportunities cost him considerable time and money, but afforded me the broad experiences that enabled me to blossom as a scientist. Altogether, I am deeply grateful to Andrew's thoughtful and generous approach to helping me reach my full potential in his lab.

Coming in to work every day was a joy, and this is due in large part to sharing the space with spectacular lab mates. Michelle Levine, in particular, was my bay mate from day one, and has been an incredible role model for humor, positivity, social grace, and generosity over the past five years. I could not have imagined a better partner with whom to go through the trials and triumphs of graduate school. Over the years, we were fortunate to attract a large cohort of wonderful lab mates, each of which has such unique and delightful strengths. To highlight a few, the formidable Thao Phan, who survived my rotation mentorship to blossom in the lab and become a trusted confidant. I cherish our late-night, contemplative

conversations, and hope there will be many more to come. To Lauren Evans, who is a bottomless well of positivity and can always put a positive spin on something when I need it the most. And to Phillip Scott, who has nourished me with countless snacks and, more importantly, his uniquely comedic take on the world.

Beyond the lab, I have been fortunate to have made such wonderful friends through my graduate program. We have shared so many adventures around the city, laughing together when times are good, and supporting one another when they aren't. Some of my fondest grad school memories are of commiseration with these friends after tough times in lab, during which they inevitably help me see the funny side of it all. Cheers especially to Karole D'Orazio and Joyce Lee, who I have always admired for their work-life balance and unfailing sense of humor even in seemingly dire times.

None of this would be possible without the dedication of the BCMB administration, who brought all of us together. It is thanks to the hard work of Arhonda Gogos and Sharon Root in the office, and Carolyn Machamer for spearheading the program for so many years, that this program continues to run smoothly and attract the wonderful people that it does.

I would also like to thank my thesis committee, Dr. Randy Reed, Dr. Geraldine Seydoux, and Dr. Seth Margolis, for their support over the years, and for valuable perspectives that helped us focus on the larger picture. Special thanks to Seth for his readiness to wax philosophical, leading to many fun and enriching discussions on finding meaning in science and career.

Lastly, I would like to thank my earliest scientific mentors: my parents, who are themselves academics. They cultivated my curiosity about the micro- and macroscopic world from as early as I can remember! I can recall many inquisitive discussions at the dinner table,

during which they would gently probe my understanding of topics spanning from electron behavior to planetary orbits, and everything in between. These countless, casually scientific conversations taught me to wonder about the "why" and the "how" underlying anything I observed. Furthermore, they encouraged me to pursue my interests, and were tireless cheerleaders as I progressed in my schooling and research path. They provided love, support, and humor through good times and bad, and on top of that, demonstrate a lifestyle of constant learning, adventure, and giving that I aspire to. Knowing that I am simply the product of a fortunate series of incredibly generous mentors, I can scarcely comprehend how lucky I am to have such wonderful and caring parents. Here's to many more years of growth and adventure together!

Table of Contents

List of Figures

Chapter 1

Introduction

1.1 Overview

1.1.1 Centrosome introduction

Centrosomes are the main microtubule-organizing centers of most animal cells, and are comprised of a pair of centrioles surrounded by pericentriolar material (PCM) (Gonczy, 2012; Nigg and Raff, 2009). Centrioles act as the centrosome organizer and thus their duplication controls centrosome number. Like DNA, centrioles duplicate exactly once per cell cycle, with a single new procentriole forming on the wall of each existing centriole (Tsou and Stearns, 2006). This tightly controlled process ensures the generation of two centrosomes to form the poles of the bipolar mitotic spindle. Errors in centriole duplication lead to abnormal centrosome number, which can result in chromosome segregation errors and the production of aneuploid progeny (Ganem et al., 2009; Silkworth et al., 2009). Aberrations in centrosome number have been associated with several human diseases, including cancer and neurodevelopmental disorders (Nigg and Raff, 2009).

1.1.2 Centrosome duplication

Canonical centriole duplication begins at the G1/S transition with the assembly of a single cartwheel structure on the wall of each pre-existing mother centriole. The cartwheel then templates the formation of a procentriole by providing a scaffold onto which microtubules are loaded (Kitagawa et al., 2011; van Breugel et al., 2011; van Breugel et al., 2014). In addition to this canonical pathway of centriole assembly, *de novo* centriole formation can occur in the absence of existing centrioles (Marshall et al., 2001; Miki-Noumura, 1977; Palazzo et al., 1992; Suh et al., 2002; Szollosi and Ozil, 1991). A striking example of this process occurs in mouse embryos, where cell divisions continue in the absence of centrioles until the 64-cell stage, at which point centrioles are created *de novo* (Szollosi et al., 1972). In vertebrate somatic cells, a variable number of *de novo* centrioles are generated after experimental removal of existing centrioles (Khodjakov et al., 2002; La Terra et al., 2005; Uetake et al., 2007). It is therefore thought that existing centrioles act to suppress *de novo* centriole assembly, although the molecular mechanism for this suppression remains unclear.

Previous approaches to study the immediate consequence of centriole loss in human cells have relied on laser ablation or microsurgery (Khodjakov et al., 2002; La Terra et al., 2005; Uetake et al., 2007). These elegant approaches only transiently remove centrioles from a small number of cells. Permanent centriole loss has been achieved through the knockout of essential centriole components (Bazzi and Anderson, 2014; Izquierdo et al., 2014; Sir et al., 2013). Although informative, these studies did not address the immediate effects of centriole duplication failure and were unable to temporally control formation of new centrioles.

1.1.3 Plk4: the centrosome master regulator

Polo-like kinase 4 (Plk4) has emerged as a conserved, dose-dependent regulator of centriole copy number and offers an attractive target to reversibly modulate centriole number in populations of cells (Bettencourt-Dias et al., 2005; Habedanck et al., 2005). Plk4 is a self-regulating enzyme that phosphorylates itself to promote its own destruction (Brownlee et al., 2011; Cunha-Ferreira et al., 2013; Cunha-Ferreira et al., 2009; Guderian et al., 2010; Holland et al., 2010a; Klebba et al., 2013; Rogers et al., 2009). This auto-regulated destruction plays an important role in controlling the abundance of endogenous Plk4 and thereby helps to limit centriole duplication to once per cell cycle (Holland et al., 2012b).

Chapter 2

Developing a tool to study centriole biology

Modified from: Lambrus BG, Uetake Y, Clutario KM, Daggubati V, Snyder M, Sluder G, Holland AJ. (2015) p53 protects against genome instability following centriole duplication failure. *Journal of Cell Biology*. doi: 10.1083/jcb.201502089.

2.1 Overview

2.1.1 Current limitations in tools to study centriole biology

Centriole function has been difficult to study due to a lack of specific tools that allow persistent and reversible centriole depletion. One attractive target that controls this process is Plk4, the master regulator of centriole biogenesis. RNA interference and knock-in approaches have been used to inhibit Plk4 function, but these strategies are slow-acting and are not readily reversible. Inhibition of Plk4 kinase activity offers a powerful alternative to manipulate Plk4 function. However, specific kinase inhibitors are difficult to develop (Holland and Cleveland, 2014; Mason et al., 2014). In addition, inhibiting Plk4 activity greatly increases protein abundance, making it challenging to dissect the relative contribution of loss of kinase activity and increased protein abundance (Holland et al., 2010a).

In this study, we developed a chemical genetics approach to rapidly and reversibly control Plk4 protein abundance in cells. Manipulating endogenous Plk4 levels allowed the reversible depletion of centrioles from populations of cycling cells and uncovered the existence of a p53-dependent pathway that guards against genome instability by preventing cellular proliferation following centriole duplication failure. By taking advantage of the acute and titratable depletion of Plk4, our data define the threshold level of Plk4 required for centriole assembly and establish the consequence of acute Plk4 depletion on centriole composition.

2.2 A novel system for rapidly and reversibly controlling Plk4 levels

To study the immediate effects caused by Plk4 depletion, we turned to an auxin-inducible degradation system that allows for post-translational control of protein abundance with the plant hormone auxin (Nishimura et al., 2009). In plants, auxin promotes the binding of the F-box protein osTIR1 to proteins containing an auxin-inducible degron (AID). In the presence of auxin, osTIR1 recruits AID-containing substrates to the Skp1, Cullin and F-Box (SCF) ubiquitin ligase, which ubiquitinates the AID-containing protein and targets it for proteasomal degradation. Ectopic expression of osTIR1 in mammalian cells generates an SCF^{TIR1} complex and enables auxin-inducible destruction of AID-tagged transgenes (Holland et al., 2012a), suggesting that the AID system could also be applied to post-translationally regulate the stability and abundance of endogenous Plk4.

We used sequential rounds of gene targeting to knock-in the AID onto the C-terminus of both endogenous Plk4 alleles in non-transformed, telomerase-immortalized, human RPE-1 cells (**Fig. 1A-B**). To facilitate detection, each $Plk4^{AID}$ allele was tagged at the C-terminus with a HA or 3x

FLAG tag. Two Plk4$^{AID\text{-}HA/AID\text{-}3xFLAG}$ (hereafter referred to as Plk4$^{AID/AID}$) clones were obtained and behaved similarly in all assays. Plk4$^{AID/AID}$ cells exhibited normal centrosome copy number and cell cycle profiles (**Fig. 1C-D**), and both Plk4$^{AID\text{-}HA}$ and Plk4$^{AID\text{-}FLAG}$ localized to the centrioles of cells in interphase and mitosis in a manner that was indistinguishable from wild type Plk4 (**Fig. 1E**). We conclude that Plk4^{AID} is capable of supporting Plk4 function(s) in centriole duplication.

We stably expressed osTIR1-9xMyc in Plk4$^{AID/AID}$ cells to place the stability of endogenous Plk4^{AID} under the control of exogenous auxin (**Fig. 2A**).

To analyze Plk4 protein levels, we immunoprecipitated Plk4$^{AID\text{-}3xFLAG}$ from cell lysates using a FLAG antibody and determined the abundance of Plk4 by immunoblot. Addition of auxin (IAA) to Plk4$^{AID/AID}$ cells led to rapid Plk4 degradation, with Plk4 falling below the limit of detection within 10 minutes of IAA addition (**Fig. 2B**). The level of Plk4 at the centrosome was measured at various times after IAA addition using antibodies raised to the FLAG tag or to the C-terminus of Plk4. Staining with the monoclonal FLAG antibody revealed that the level of Plk4 at the centrosomes of interphase cells declined by > 95% within 30 minutes of IAA addition (**Fig. 2C,D**), while staining with a polyclonal antibody to the C-terminus of Plk4 revealed a > 80% reduction during the same time period (**Fig. 1F**). Plk4 destruction occurred in all cell cycle phases **(Fig. 2E)** and required the presence of the osTIR1 F-box protein (**Fig. 1G**). Importantly, the degradation of Plk4 was fully reversible, with the level of Plk4 at the centriole recovering to original levels within 3 hours of IAA removal (**Fig. 2F**).

To examine whether treatment with IAA leads to the expected failure of centriole duplication, we assessed centriole number in cells undergoing mitosis one cell cycle (30 hours) after IAA addition. In untreated Plk4$^{AID/AID}$ cells, centriole duplication occurred successfully in > 90% of cells (0 μM IAA, **Fig. 3A,B**). By contrast, IAA addition caused a failure of centriole duplication in > 90% of Plk4$^{AID/AID}$ cells (500 μM IAA, **Fig. 3A,B**). We conclude that Plk4$^{AID/AID}$ cells offer a new tool to achieve rapid and reversible depletion of endogenous Plk4.

2.3 A graded reduction in protein levels reveals a threshold level of Plk4 required for centriole duplication

Reduced expression of Plk4 has been associated with tumorigenesis, but it remains unknown how much Plk4 protein is required for centriole duplication (Ko et al., 2005; Liu et al., 2012; Pellegrino et al., 2010). Since Plk4 autoregulates its own stability, generating a progressive reduction in Plk4 protein levels is challenging, as a reduced abundance of Plk4 mRNA may not lead to a comparable downregulation of Plk4 protein (Holland et al., 2012a). We therefore set out to use auxin-inducible destruction to generate a graded reduction in Plk4 levels. We used quantitative microscopy with directly labeled Plk4 primary antibodies to determine the abundance of Plk4 at the centriole in cells treated with various concentrations of IAA. Exposing Plk4$^{AID/AID}$ cells to increasing concentrations of IAA resulted in gradual reduction in the average level of Plk4 at the centriole (**Fig. 3A**). We examined whether centriole duplication occurred successfully with different levels of Plk4 protein. In cells treated with 1 μM IAA, the average level of Plk4 at the centrosome was 81% of that in untreated cells (**Fig. 3A,B**). Under these conditions, centrioles duplicated in > 75% of cells. However, at 10 μM IAA, while centrosomal Plk4 levels were maintained at 57% of that in control cells, < 10% of cells underwent centriole

duplication (**Fig. 3A,B**). We conclude that Plk4 levels are finely balanced and that a < 2-fold reduction in the level of Plk4 at the centrosome leads to a failure of centriole duplication.

2.4 The centriole localization of STIL is uniquely sensitive to the levels of Plk4

RNAi of Plk4 leads to slow protein depletion making it challenging to distinguish between direct and indirect effects of Plk4 removal. The ability to rapidly remove Plk4 from cells provided an opportunity to identify proteins that directly depend on Plk4 for recruitment to the centriole. We used immunofluorescence microscopy to examine the abundance of 10 proteins (CPAP, CEP135, CEP152, CEP192, SAS6, CNAP1, CEP164, Centrin, γ-tubulin and STIL) at the centrosome 1 hour after Plk4 destruction with IAA. Since the abundance of several centriole proteins are reduced after mitosis (Arquint and Nigg, 2014; Arquint et al., 2012; Strnad et al., 2007; Tang et al., 2009; Tang et al., 2011), our measurements were made in S/G2 cells that were marked by the presence of CENP-F (Hussein and Taylor, 2002). Of the 10 proteins examined, the localization of STIL was uniquely sensitive to a reduction in Plk4 levels: the abundance of STIL at the centriole was reduced by > 75% 1 hour after IAA addition, while total protein levels remained unchanged (**Fig. 3C**). These data are consistent with a recent study showing that Plk4 binds to STIL (Ohta et al., 2014). STIL has been proposed to recruit SAS6 to the centriole though a direct, phosphorylation dependent interaction (Arquint et al., 2012; Dzhindzhev et al., 2014; Ohta et al., 2014; Tang et al., 2011; Vulprecht et al., 2012). However, while STIL levels declined dramatically by one hour after acute Plk4 destruction, we observed only a modest change in centriole SAS6 levels, suggesting STIL is not required to maintain existing SAS6 at the centriole (**Fig. 3C**).

2.5 Cells lacking Plk4 undergo a cell cycle arrest

We next examined the chronic effect of Plk4 depletion in RPE1 cells. While $Plk4^{+/+}$ cells proliferated normally in the presence of IAA, addition of IAA to $Plk4^{AID/AID}$ cells resulted in a cell cycle arrest 48 hours after treatment began (**Fig. 5A**). Interphase $Plk4^{AID/AID}$ cells exhibited a dramatic reduction in centriole number by 24 hours after IAA addition (**Fig. 5B**). Centriole number decreased further by 48 hours after Plk4 degradation, giving rise to 22% of cells that lack centrioles. After this time, centriole content changed only slowly, consistent with the fact that the vast majority of cells cease proliferating by 48 hours after IAA addition.

To evaluate the long-term growth potential of cells that lack endogenous Plk4, we performed clonogenic survival assays. IAA addition prevented colony formation in $Plk4^{AID/AID}$ cells, but only modestly affected the survival of $Plk4^{+/+}$ and $Plk4^{+/AID}$ cells (**Fig. 4A-B**). To determine whether Plk4 depletion leads to an irreversible cell cycle arrest, we treated $Plk4^{AID/AID}$ cells with IAA for either one hour or four days and then restored Plk4 levels by washing out IAA. While one hour of IAA treatment had no affect on cell growth, washout of IAA after 4 days of treatment was unable to restore cell proliferation (**Fig. 5C**). We conclude that chronic depletion of Plk4 leads to an irreversible cell cycle arrest.

To examine the effect of centriole loss on cell division, we created $Plk4^{AID/AID}$ cells co-expressing TagRFP-tubulin, EGFP-Histone H2B, and EGFP-Cep63 [to mark parental centrioles (Sir et al., 2011)] and monitored cells by time-lapse microscopy. Untreated control cells progressed though mitosis with an average time of 44 minutes and contained a single EGFP-

Cep63 focus at each spindle pole (**Fig. 5D,G**). In the first 24 hours after Plk4 destruction, all cells formed bipolar spindles and divided normally, albeit with a modest mitotic delay (average time of 58 minutes to divide) (**Fig. 5D,E**). However, by the second day after IAA addition the duration of mitosis increased to an average time of 84 minutes (**Fig. 5D**). Nevertheless, all cells progressed to anaphase and successfully executed cytokinesis (**Fig. 5E)**. Although there was an increase in chromosome segregation errors in auxin-treated cells, the frequency of these errors was too small to account for the growth arrest (**Fig. 5E**). Interestingly, in a significant fraction of divisions, multi-lobed nuclei formed after apparently normal anaphase chromosome movements (**Fig. 5F-G**). Importantly, these cell division defects were not caused by drug treatment alone, as IAA had little effect on mitotic timing or nuclear shape in $Plk4^{+/+}$ RPE1 cells (**Fig. 4C-D**).

2.6 The cell cycle arrest following centriole duplication failure is not caused by a prolonged mitosis.

Using fixed imaging, we examined the number of centrioles at various time points after IAA treatment. As expected, untreated control cells divided with two centrioles at each spindle pole (**Fig. 6A-B**). By contrast, at one day after IAA addition, > 90% of $Plk4^{AID/AID}$ cells divided with a single centriole at each spindle pole, while at days 2 and 3 after IAA addition > 65% of cells divided with an asymmetric spindle comprised of an acentriolar pole and a pole containing a single centriole (**Fig. 6A-B**). Cell divisions were rarely observed to take place in the absence of centrioles.

Previous work has shown that prolonging prometaphase to > 90 minutes leads to a durable G1 arrest in RPE1 cells (Uetake and Sluder, 2010). We therefore investigated whether an increased

mitotic duration could account for the cell cycle arrest observed after centriole duplication failure. We first set out to determine the window of tolerance for prometaphase duration in $Plk4^{AID/AID}$ cells. $Plk4^{AID/AID}$ cells were treated with 0.08 μM nocodazole for 6 hours and the proliferative fate of daughter cells monitored using time-lapse microscopy. Similar to the parental RPE1 cells, prolonging the duration of prometaphase in $Plk4^{AID/AID}$ cells to > 97 minutes caused a cell cycle arrest in all resulting daughters (**Fig. 7A**). Addition of IAA to parental RPE1 cells shortened the window of prometaphase tolerance to 60 minutes (**Fig. 7B**). Consequently, we considered 60 minutes to be the prometaphase threshold for IAA-treated cells.

We next traced the lineage of individual $Plk4^{AID/AID}$ cells treated with IAA (**Fig. 7C**). Only cells that entered the first division within 6 hours of IAA addition were considered in our analysis. As a consequence, the first mitosis nearly always occurred with two centrioles at each spindle pole and all daughter cells continued to proliferate (**Fig. 6B-C**). In subsequent divisions, centriole number was successively reduced as expected from failed centriole duplication and continued cell growth. 48% of daughter cells arrested after the second mitosis, while 78% of daughters arrested after the third mitosis and all daughter cells arrested after the fourth mitosis (**Fig. 6C**). The delayed growth arrest after Plk4 destruction strongly suggests that a stress associated with a failure of centriole duplication, not loss of Plk4 *per se*, is responsible for the proliferative arrest.

In the second division after Plk4 destruction, nearly all daughters of mothers that spent > 60 minutes in prometaphase arrested as expected (**Fig. 6D**). However, 37% of the daughters of mothers that spent < 60 minutes in prometaphase also arrested and this fraction increased to 52% and 100% in the third and fourth divisions, respectively. It was previously shown that continuous

inhibition of p38 MAPK activity with the small molecule SB203580 overcame the proliferative block caused by a prolonged prometaphase induced by transient nocodazole treatment. However, inhibition of p38 MAPK activity did not prevent or delay the cell cycle arrest caused by Plk4 loss (**Fig. 7D**). We conclude that the cell cycle arrest caused by centriole duplication failure is not simply due to a prolonged prometaphase duration (Uetake and Sluder, 2010).

Previous work has shown that DNA damage, Hippo pathway activation or excessive oxidative stress can cause a cell cycle arrest (Ganem et al., 2014). However, addition of IAA for three days did not lead to a detectable increase in DNA damage (measured by γH2A.X phosphorylation) or Hippo pathway activation (revealed by LATS2 or YAP phosphorylation) in $Plk4^{AID/AID}$ cells **(Fig. 6E)**. In addition, culturing $Plk4^{AID/AID}$ cells in 3% O_2, rather than 21% O_2, did not prevent the proliferative arrest following Plk4 destruction (**Fig. 6F**). Taken together, our data suggest that DNA damage, Hippo pathway activation, and oxidative stress are unlikely to be the cause of the cell cycle arrest that occurs following a failure of centriole duplication.

2.7 Repression of p53 allows Plk4-depleted cells to proliferate and become acentriolar

RPE1 cells maintain a normal p53-response. $Plk4^{AID/AID}$ cells but not $Plk4^{+/+}$ cells showed stabilization of p53 at two and three days after IAA addition (**Fig. 8A**). We therefore tested whether stabilization of p53 contributes to the irreversible cell cycle arrest that occurs following Plk4 depletion and centriole duplication failure. Preventing p53 accumulation using a stably expressed p53 shRNA (**Fig. 8B**) allowed the continued growth of cells lacking Plk4 (**Fig. 9A**) and led to a partial recovery of the clonogenic survival of this population (**Fig. 8C-D**). Our

findings indicate that a failure of centriole duplication increases p53 levels, eliciting a p53-dependent cell cycle arrest. This is consistent with prior work showing that knockout cells lacking proteins essential for centriole duplication also fail to proliferate in the presence of p53 (Bazzi and Anderson, 2014; Izquierdo et al., 2014).

$Plk4^{AID/AID}$;p53 shRNA cells proliferated indefinitely in the absence of Plk4, and by 6 days after IAA addition Centrin foci were undetectable in > 90% of cells (**Fig. 9B-C**). To confirm that chronically treated $Plk4^{AID/AID}$;p53 shRNA cells lacked centrioles, we performed immunostaining for a variety of centriole components (CPAP, SAS6, STIL, CEP135, CEP152, CEP192), but failed to observe centriole foci in the vast majority of cells (data not shown). We therefore used thin-section electron microscopy to evaluate the presence of centrioles. While centrioles were identified in 37/138 transverse sections of control cells, we never observed centrioles in 320 sections from chronically IAA-treated cells. Thus, the failure to detect Centrin foci almost certainly reflects an absence of centrioles in the vast majority of chronically treated $Plk4^{AID/AID}$;p53 shRNA cells (hereafter referred to as acentriolar cells). Consistent with a lack of centrioles, the PCM component γ-tubulin was diffusely localized throughout the cytosol of interphase cells lacking centrioles and failed to concentrate at acentriolar spindle poles (**Fig. 9C**). However, 55% of interphase acentriolar cells contained a single focus of the PCM component Pericentrin, suggesting that Pericentrin may have the capacity to self-organize in the absence of centrioles (**Fig. 8E**).

To directly examine the divisions of cells lacking centrioles, acentriolar cells co-expressing TagRFP-tubulin, EGFP-Histone H2B and EGFP-Cep63 were monitored by time-lapse

microscopy. Untreated Plk4$^{AID/AID}$;p53 shRNA cells entered mitosis with two microtubule asters and assembled robust bipolar spindles (**Fig. 9E**). By contrast, in acentriolar cells microtubule nucleation occurred randomly around the chromatin, before self-organizing into a bipolar spindle with Pericentrin, but not γ-tubulin, concentrated at the poles (**Fig. 9C,E; Fig. 8E**). Acentriolar divisions exhibited an increased mitotic duration (average of 147 minutes, compared with 42 minutes for untreated cells) and were associated with a higher frequency of chromosome segregation errors (40% in acentriolar cells vs 17% in control cells) and cytokinesis failure (22% in acentriolar cells vs 1% in control cells) compared with untreated control Plk4$^{AID/AID}$;p53 shRNA cells (**Fig. 9D**). Consistent with the increased incidence of cytokinesis failure, a sub-population of acentriolar cells contained a tetraploid DNA content (**Fig. 8F**)**.** These mitotic errors are likely to be the cause of the reduced growth rate and increased doubling time of acentriolar cells (**Fig. 9A, Fig. 8G**). These data are in accord with the view that centrioles are not strictly essential for mitosis in vertebrate cells, but increase the fidelity of chromosome segregation and cytokinesis (Debec et al., 2010; Khodjakov and Rieder, 2001; Sir et al., 2013).

2.8 Restoration of endogenous Plk4 levels in acentriolar cells results in *de novo* centriole formation.

In vertebrate somatic cells, *de novo* centriole assembly is initiated following the eradication of the existing centrioles by laser ablation or microsurgery (Khodjakov et al., 2002; La Terra et al., 2005; Uetake et al., 2007). In this case a variable number of *de novo* centrioles are spontaneously generated. We therefore examined the effect of restoring endogenous Plk4 levels in acentriolar cells. Endogenous Plk4 levels returned to normal within 12 hours of IAA washout (**Fig. 10A**) and promoted the penetrant formation of *de novo* centrioles: by two days after IAA washout, *de*

novo centriole assembly occurred in 74% of cells and increased to > 95% of cells by four days after IAA removal (**Fig. 10B, Fig. 8H**). Knockdown of the cartwheel component STIL prevented *de novo* centriole assembly, suggesting that, similar to canonical centriole duplication, *de novo* centrioles assemble through a cartwheel-dependent mechanism (**Fig. 10C**). Taken together, these data show that Plk4 levels are rate limiting for both canonical and *de novo* centriole assembly.

De novo centriole assembly occurred stochastically throughout the cytosol of cells, resulting in the formation of a variable number of centrioles (**Fig. 10B, Fig. 8H**). While cells with 1-4 de novo centrioles always divided normally, cells with supernumerary *de novo* centrioles underwent frequent (6-18%) multi-polar divisions (**Fig. 10D-F**). Since the progeny of multi-polar divisions are invariably inviable (Ganem et al., 2009), aberrant mitotic divisions are likely to limit the proliferative potential of cells with supernumerary *de novo* centrioles. The decreased growth potential of cells with supernumerary centrioles may explain why the fraction of cells with a normal centriole number gradually increases in abundance after IAA washout (**Fig. 10B)**.

De novo centriole assembly required cell cycle progression, as arresting cells in G1 phase with mimosine or the CDK2/4 inhibitor PD0332991 greatly reduced the frequency of *de novo* centriole formation by two days after IAA washout (**Fig. 11A-C**) (Fry et al., 2004; Watson et al., 1991). To examine the composition of *de novo* centrioles we performed immunostaining for several centriole components at 1, 2, 3 and 4 days after IAA washout. By two days after IAA washout, Plk4, CPAP, CEP135, CEP152, CEP164 and CEP192 co-localized with at least one Centrin-marked, *de novo* centriole in > 75% of cells (**Fig. 10G, Fig. 11D**). By contrast, only 40-55% of cells with *de novo* centrioles contained centriole-localized STIL or SAS6, consistent with

the fact that STIL and SAS6 are absent from centrioles during G1 phase (Arquint and Nigg, 2014; Arquint et al., 2012; Strnad et al., 2007; Tang et al., 2011). Importantly, all of the *de novo* centrioles observed in transverse sections by EM exhibited a normal morphology, with triplet microtubules arranged with nine-fold rotational symmetry (n = 83 total *de novo* centrioles, 13 of which were sectioned transversely and could be assessed for rotational symmetry) (**Fig. 12A-B**).

To examine the kinetics of *de novo* centriole assembly, we generated acentriolar cells stably expressing EGFP-Centrin and performed time-lapse imaging following IAA washout. Approximately 9 hours prior to mitosis, a variable number of EGFP-Centrin foci formed dispersed throughout the cytosol (**Fig. 13A-B**). These foci increased in size and intensity until they were indistinguishable from EGFP-Centrin foci observed at normal centrioles in control cells. Immunofluorescence staining showed that the newly formed Centin foci co-localized with CEP192 and are thus likely to represent *de novo* centrioles (**Fig. 13C**). Once *de novo* centrioles had formed, no additional Centrin foci were generated, consistent with the observation that *de novo* centriole assembly is inhibited by the presence of centrioles (**Fig. 13A**) (La Terra et al., 2005; Marshall et al., 2001). To test if a single centriole is capable of suppressing *de novo* centriole formation, we transiently treated EGFP-Centrin expressing $Plk4^{AID/AID}$;p53 shRNA cells with IAA to generate a fraction of cells with a single centriole, then removed IAA and monitored *de novo* centriole formation by time lapse microcopy. Strikingly, while 80% of acentriolar cells underwent de novo centriole formation within 36 hours of IAA washout, only 15% of cells with a single centriole underwent *de novo* centriole assembly in the same period (**Fig. 11E**).

In the first mitotic division after IAA washout, the majority of single *de novo* centrioles segregated on the mitotic spindle (**Fig. 13D**). After the first division, *de novo* centrioles clustered to a single location. Later in the cell cycle, centrioles dispersed around the nuclear envelope and underwent duplication, with each single EGFP-Centrin focus becoming a duplex of two centrioles (**Fig. 13A,C**). Pairs of Centrin foci always contained a single focus of the proximal centriole marker CNAP1, consistent with an engaged "mother-daughter" configuration (**Fig. 13E**). CEP164 is a distal appendage protein that usually marks the mature mother centriole (Graser et al., 2007). Surprisingly, however, duplicated pairs of *de novo* centrioles did not always contain a CEP164-positive centriole (**Fig. 11F**). By two days after IAA washout, duplicated centriole pairs recruited PCM material and acted as MTOCs (**Fig. 13D**). We conclude that the *de novo* centrioles are functionally indistinguishable from canonical centrioles.

2.9 Discussion

In this study, we have developed a chemical genetic approach to reversibly deplete Plk4 and centrioles in a proliferating population of human cells. This is the first time the auxin-inducible destruction system has been used to reversibly manipulate the levels of an endogenous protein in vertebrate cells. In principle, the strategy we have taken could be applied to control the levels of many proteins that are not amenable to traditional chemical inhibition. In the future, combining the AID-system with CRISPR/Cas9 genome engineering will greatly increase the efficiency with which bi-allelic targeting of endogenous genes can be achieved, paving the way for rapid and tunable control of protein function.

The long-term consequence of centriole depletion has not been studied in a non-transformed vertebrate cell line. By inducing chronic depletion of Plk4, we reveal the presence of a p53-dependent pathway that arrests the growth of untransformed cells following a failure of centriole duplication (**Fig. 9A**). Furthermore, by exploiting the reversibility of Plk4 depletion, we show that the cell-cycle arrest caused by centriole loss is irreversible (**Fig. 5C**). A recent study arrived at similar conclusions using a potent inhibitor of Plk4 kinase activity to deplete centrioles from proliferating cells (Wong et al., 2015a). Mouse embryos lacking the essential centriole protein CPAP lack centrioles and cilia and die during midgestation due to widespread p53-dependent apoptosis (Bazzi and Anderson, 2014). Similarly, deletion of CPAP in the developing mouse brain also resulted in increased cell death, which was rescued by removal of p53 (Insolera et al., 2014). The contrast between the apoptotic response in mouse embryos and the arrest we observed in human cells suggests that embryonic and adult cell types have different proclivities for initiating apoptosis or senescence after centriole loss. Interestingly, in contrast to the situation in mouse and human cells, *Drosophila* cells lacking centrioles do not arrest or die (Basto et al., 2006; Lecland et al., 2013), suggesting that cell-cycle checkpoints for eliminating acentriolar cells are more stringent in vertebrates.

While mouse embryos proceed through many cell divisions without centrioles before initiating apoptosis, we found that many human somatic cells ceased dividing prior to the total loss of centrioles (**Fig. 6B**). Importantly, we did not observe detectable increases in Hippo pathway activation, DNA damage or cytokinesis failure in the 2-3 cell cycles that occur after Plk4 degradation (**Fig. 5E and 6E**). We did, however, observe an increase in chromosome segregation errors in cells with a reduced centriole number (9% at day 1, 19% at day 2, and 14% at day 3

after IAA addition) (**Fig. 5E**). While chromosome segregation errors can lead to a p53-dependent arrest (Thompson and Compton, 2010), the frequency of these errors was too low to account for the reduction in proliferation after Plk4 loss (**Fig. 5E**). In mouse embryos that lack centrioles, the stabilization of p53 was proposed to arise as a result of a modest (~10 minute) increase in mitotic duration (Bazzi and Anderson, 2014). However, using single-cell lineage tracing, we show that an extended mitosis cannot, by itself, explain the cell cycle arrest that occurs in human cells that fail centriole duplication (**Fig. 6D**). Further investigation will therefore be required to establish the underlying cause of the proliferative arrest that occurs following Plk4 loss.

Removal of p53 allowed human cells to proliferate indefinitely despite the absence of centrioles (**Fig. 9A**). As centrosomes increase the speed of spindle assembly, these acentriolar cells formed bipolar spindles at a considerably slower rate than cells containing centrioles. In addition, acentriolar cells displayed chromosomal instability and frequent cytokinesis failure (**Fig. 9D**). Similar mitotic errors have been reported in acentriolar *Drosophila* cells and transformed vertebrate cell lines, highlighting the important role of centrioles in ensuring the fidelity of cell division in adult cells (Basto et al., 2006; Debec et al., 2010; Khodjakov and Rieder, 2001; Sir et al., 2013). Surprisingly, however, acentriolar mouse embryos showed no detectable increase in chromosome segregation errors (Bazzi and Anderson, 2014). The first five rounds of cell division in the mouse embryo are naturally acentriolar (Szollosi et al., 1972) and it is therefore possible that mouse embryonic divisions are less dependent on centrioles for faithful chromosome segregation.

Overexpression of Plk4 did not promote *de novo* centriole formation in acentriolar mouse zygotes (Coelho et al., 2013), but was capable of inducing *de novo* centriole formation in unfertilized fly eggs (Peel et al., 2007; Rodrigues-Martins et al., 2007) and activated *Xenopus* oocytes (Eckerdt et al., 2011). Here we have shown that restoring endogenous levels of Plk4 induces *de novo* centriole formation in acentriolar human somatic cells. We speculate that *de novo* centrioles are created from Plk4 foci that form stochastically in the cytosol of acentriolar cells (**Fig. 11G**). Once these foci surpass a threshold level of Plk4 activity, cartwheel assembly would be initiated, leading to centriole formation. Consistent with this idea, we were able to observe recruitment of the cartwheel components STIL and SAS6 to Plk4 foci as an early event occurring prior to incorporation of Centrin into *de novo* centrioles (**Fig. 11G**).

De novo centrioles assembled very efficiently (within 2-3 cell cycles) following restoration of Plk4 levels (**Fig. 10B**). This is in accordance with the previous work examining the kinetics of *de novo* centriole formation in somatic human cells (La Terra et al., 2005; Uetake et al., 2007) and green algae (Marshall et al., 2001). Procentrioles formed in S phase are normally modified during mitosis to activate their ability to recruit PCM material and function as MTOCs in the next cell cycle (Wang et al., 2011). In our experiments, cells that lack centrioles undergo a prolonged prometaphase, providing increased time for newly created *de novo* centrioles to be modified and converted into MTOCs. Consistently, we observed that in the first cell cycle, the vast majority of *de novo* centrioles recruited small amounts of PCM material in mitosis and were capable of segregating themselves on the mitotic spindle (**Fig. 13D**). *De novo* centrioles duplicated in the second cell cycle after their creation, consistent with a previous report

demonstrating that newly formed centrioles are modified in mitosis to license their duplication (**Fig. 13A,D**) (Wang et al., 2011).

A single centriole was shown to suppress *de novo* centriole assembly in the vast majority of cells, supporting the conclusion that existing centrioles inhibit the *de novo* assembly pathway (**Fig. 11E**) (La Terra et al., 2005; Marshall et al., 2001). Like canonical centriole assembly, *de novo* centriole formation requires Plk4 activity (Wong et al., 2015b). An intriguing possibility, therefore, is that existing centrioles sequester an activator of Plk4 and thereby act to inhibit the cytosolic pool of Plk4 and suppress *de novo* centriole formation. The ability to induce timed *de novo* centriole biogenesis in populations of cycling acentriolar cells offers an excellent tool to dissect the molecular events involved in centriole formation and how centrioles antagonize the *de novo* pathway.

2.10 Figures and Legends

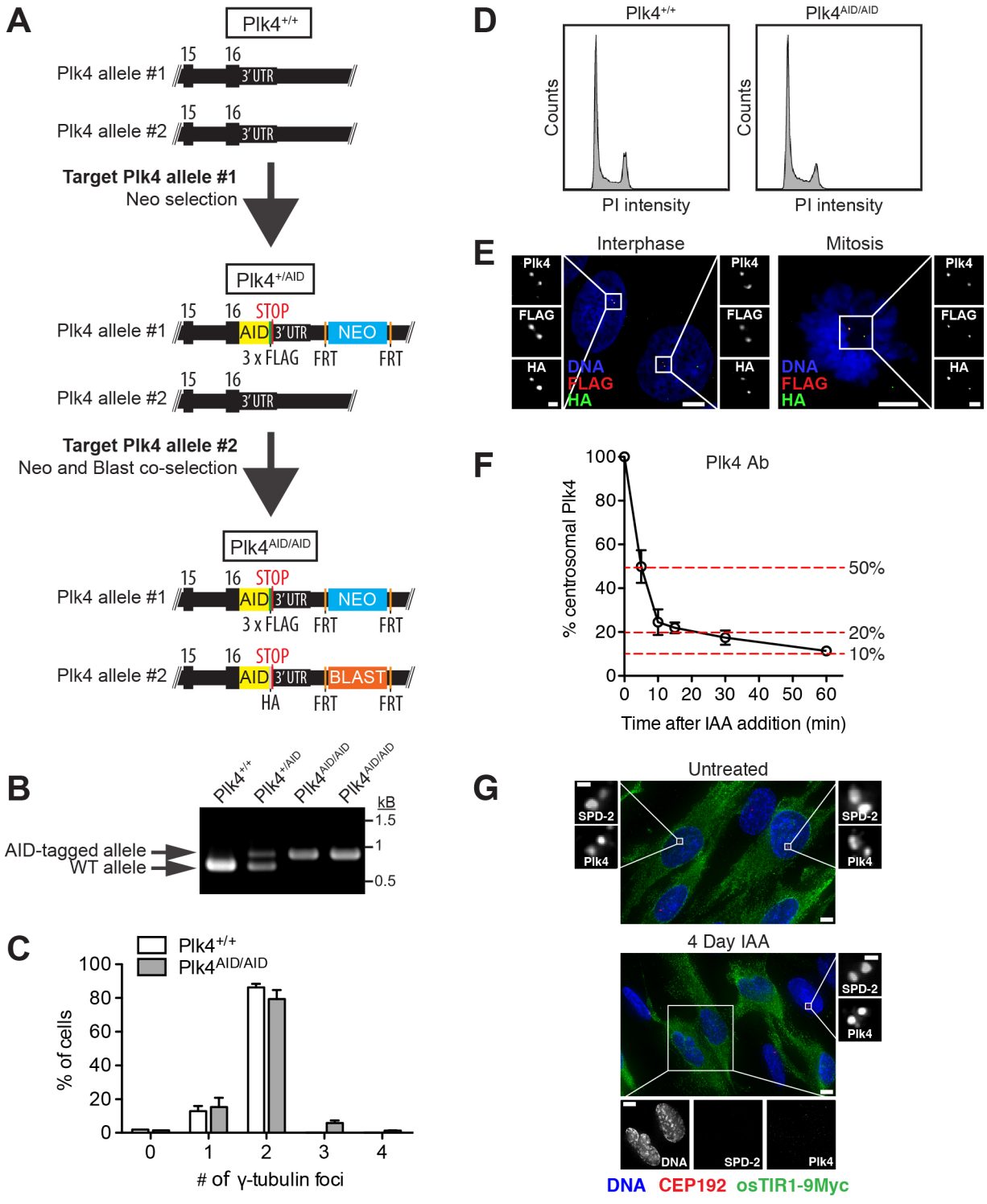

Figure 1. Generation of Plk4$^{AID/AID}$ cells.

(A) Schematic outlining the strategy for the construction of $Plk4^{AID/AID}$ RPE1 cells.

(B) Genotyping of Plk4-AID heterozygous and homozygous cells. $Plk4^{AID/AID}$ cells possess a single band corresponding to the Plk4-AID allele.

(C) Quantification of the number of γ-tubulin foci in $Plk4^{+/+}$ and $Plk4^{AID/AID}$ cells. Each bar represents the mean of > 100 cells from at least two independent experiments. Error bars represent the S.E.M.

(D) Flow cytometry cell cycle analysis showing normal asynchronous cell cycle profiles for $Plk4^{+/+}$ and $Plk4^{AID/AID}$ cells.

(E) Selected images of $Plk4^{AID/AID}$ cells immunostained for Plk4, FLAG and HA. HA, FLAG and Plk4 antibody signals co-localize in interphase and mitotic cells. Scale bars: 5 μm (main); 1 μm (inset).

(F) Quantification of the level of Plk4 at the centrosome at the indicated times after IAA addition. Each condition represents the mean of > 70 cells from at least two independent experiments. Error bars represent the S.E.M.

(G) Selected images of untreated control or IAA-treated cells immunostained with CEP192, Plk4 and Myc. 4 days after IAA addition, CEP192 and Plk4 are no longer detectable in cells expressing the F-box protein osTIR1-9Myc, but are present in neighboring cells lacking osTIR1-9Myc. Scale bars: 5 μm (main); 1 μm (inset).

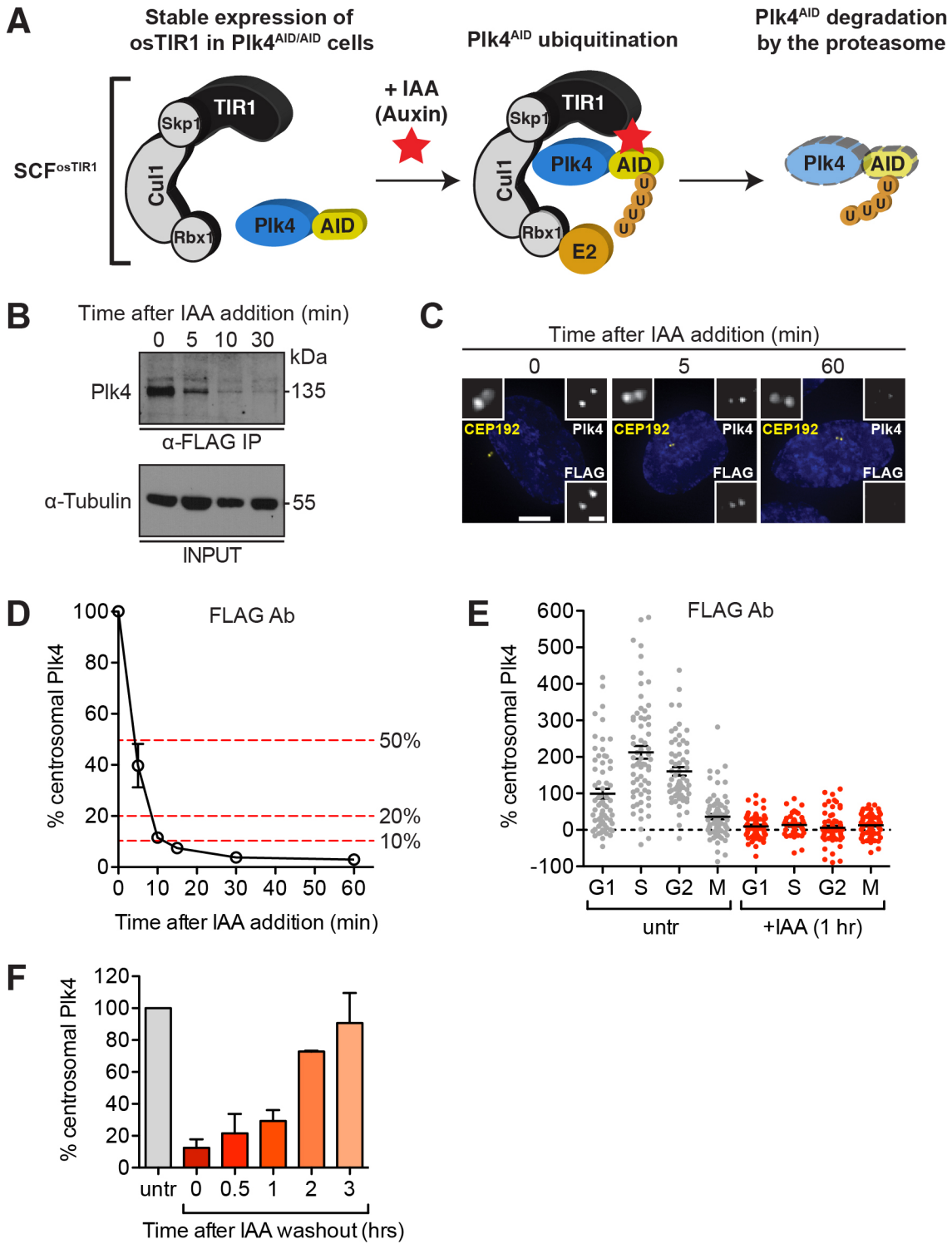

Figure 2. Inducible destruction of endogenous Plk4.

(A) Schematic outlining the strategy for the auxin-inducible destruction of Plk4.

(B) Western blot showing the levels of immunoprecipitated Plk4-AID-FLAG at the indicated times after IAA addition.

(C) Plk4$^{AID/AID}$ cells immunostained for CEP192, Plk4 and FLAG after treatment with IAA for the indicated time. Scale bars: 5 μm (main); 1 μm (inset).

(D) Quantification of the level of FLAG-tagged Plk4-AID at the centrosome at the indicated times after IAA addition. Each condition represents the mean of > 70 cells from at least two independent experiments.

(E) Quantification of the level of FLAG-tagged Plk4-AID at the centrosome at the indicated cell cycle stages. Horizontal line represents the mean of > 70 cells from two independent experiments.

(F) Quantification of Plk4 protein levels at the centrosome at the indicated time after IAA washout. Plk4 levels return to normal within 3 hours of auxin removal. Each bar represents the mean of > 70 cells from at least two independent experiments. All error bars in the figure represent the S.E.M.

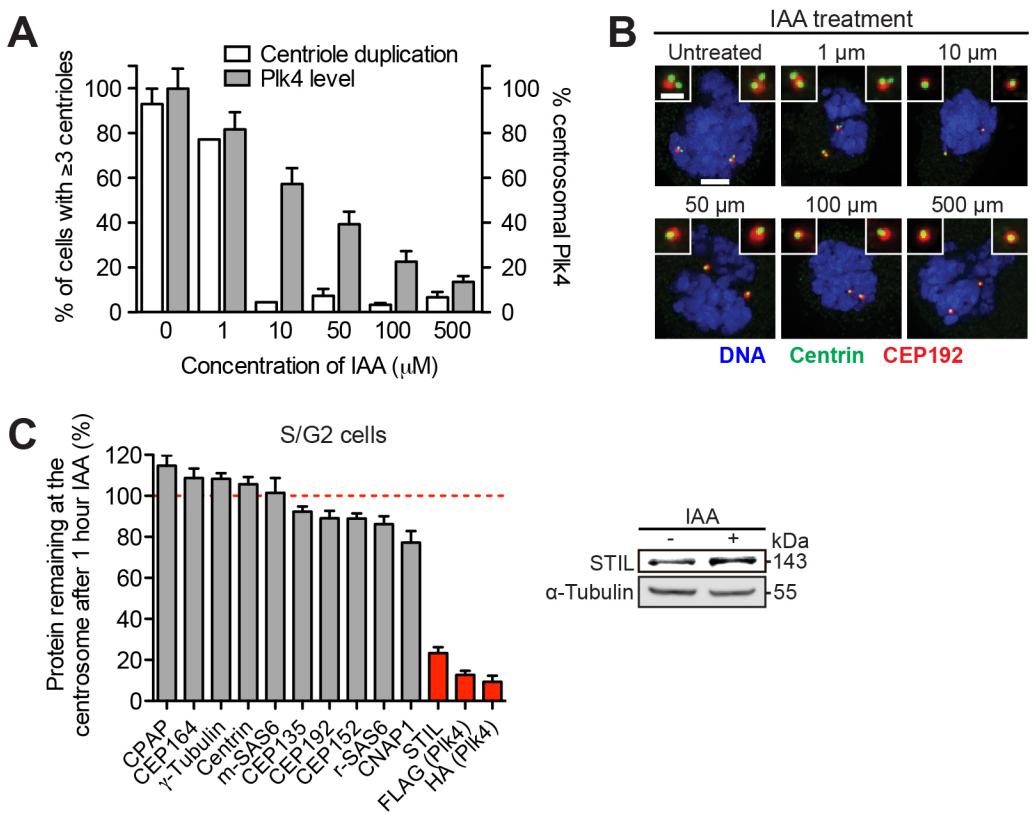

Figure 3. The centriole localization of STIL requires Plk4.

(A) Quantification of Plk4 protein levels at the centrosome of interphase cells at 24 hours after addition of the indicated concentrations of IAA (grey bars). The fraction of mitotic cells that underwent successful centriole duplication (≥ 3 centrioles) was quantified in the same samples (open bars). Bars represent the mean of > 40 cells from two independent experiments.

(B) Representative images of Plk4$^{AID/AID}$ cells immunostained with CEP192 and Centrin after treatment with the indicated dose of IAA for 24 hours. Scale bars: 5 μm (main); 1 μm (inset).

(C) Quantification of relative protein abundance at the centrosome of S or G2 phase (CENP-F positive) cells 1 hour after IAA addition. Centriole recruitment of STIL requires Plk4. r-SAS6 = rabbit SAS6 antibody; m-SAS6 = mouse SAS6 antibody. Bars represent the mean of > 35 cells from two independent experiments. Immunoblot shows no change in the level of endogenous STIL after Plk4 degradation. All error bars in the figure represent the S.E.M.

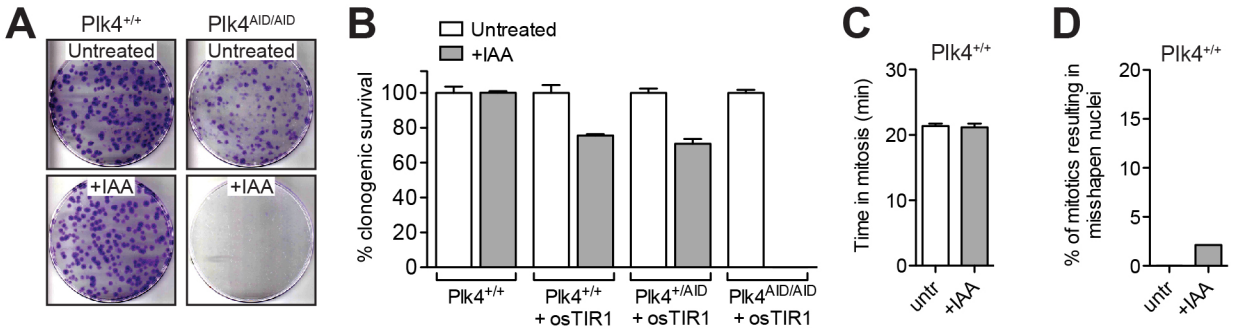

Figure 4. Destruction of Plk4 leads to a long-term growth arrest.

(A) Representative images of crystal violet stained colonies formed two weeks after addition of IAA.

(B) Quantification of the percent clonogenic survival of the indicated cell lines. Bars represent the mean of at least two independent experiments carried out in triplicate.

(C) – (D) Quantification of mitotic duration and the frequency of divisions resulting in the formation of misshapen nuclei in IAA-treated Plk4$^{+/+}$ cells. IAA has a negligible impact on mitotic fidelity. Bars represent the mean of > 50 cells from two independent experiments.

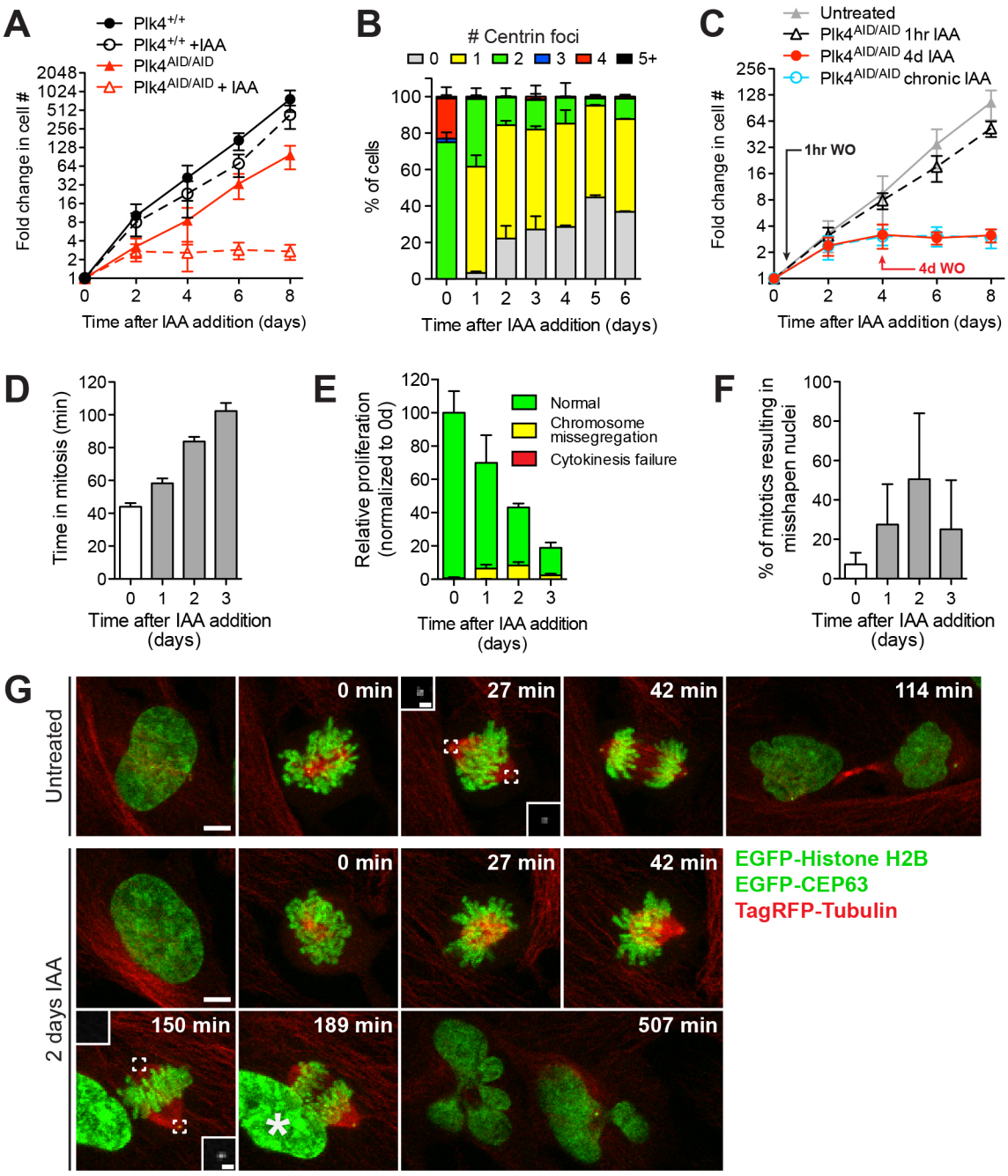

Figure 5. Plk4 depletion leads to a failure of centriole duplication followed by a cell-cycle arrest.

(A) Graph showing the fold increase in cell number after IAA addition. Plk4 destruction leads to a cell-cycle arrest in Plk4$^{AID/AID}$ cells. Points show the mean of at least two independent experiments performed in triplicate.

(B) Quantification of the number of Centrin foci per cell in interphase at indicated times after IAA addition. Bars represent the mean of > 100 cells from two independent experiments.

(C) Graph showing the fold increase in cell number after IAA washout (WO) and restoration of Plk4 levels. Centriole loss leads to an irreversible cell-cycle arrest. Points show the mean of at least two independent experiments performed in triplicate.

(D) Quantification of the duration of mitosis. Measurements were taken over a 24-hour period at indicated times after IAA addition. Bars represent the mean of > 60 cells from two independent experiments.

(E) Quantification of relative cell proliferation and fraction of cells undergoing chromosome missegregation or cytokinesis failure. Measurements were taken over a 24-hour period at indicated times after IAA addition. Bars represent the mean of > 40 cells from two independent experiments.

(F) Quantification of the frequency of divisions resulting in the formation of misshapen nuclei. Measurements were taken over a 24-hour period at indicated times after IAA addition. Bars represent the mean of > 40 cells from two independent experiments. All error bars in the figure represent the S.E.M.

(G) Selected images from a time-lapse series of untreated or IAA-treated $Plk4^{AID/AID}$ cells co-expressing histone TagRFP-Tubulin, EGFP-Histone H2B and EGFP-CEP63. Insets show EGFP-CEP63 at the centrosome. Time is indicated in minutes relative to nuclear envelope breakdown (time point 0). Note that the cell treated with IAA for 2 days exhibits an asymmetric spindle with one acentriolar pole. The interphase nucleus labeled with an asterisk at 189 min later left the field of view. Scale bars: 5 μm (main); 1 μm (inset).

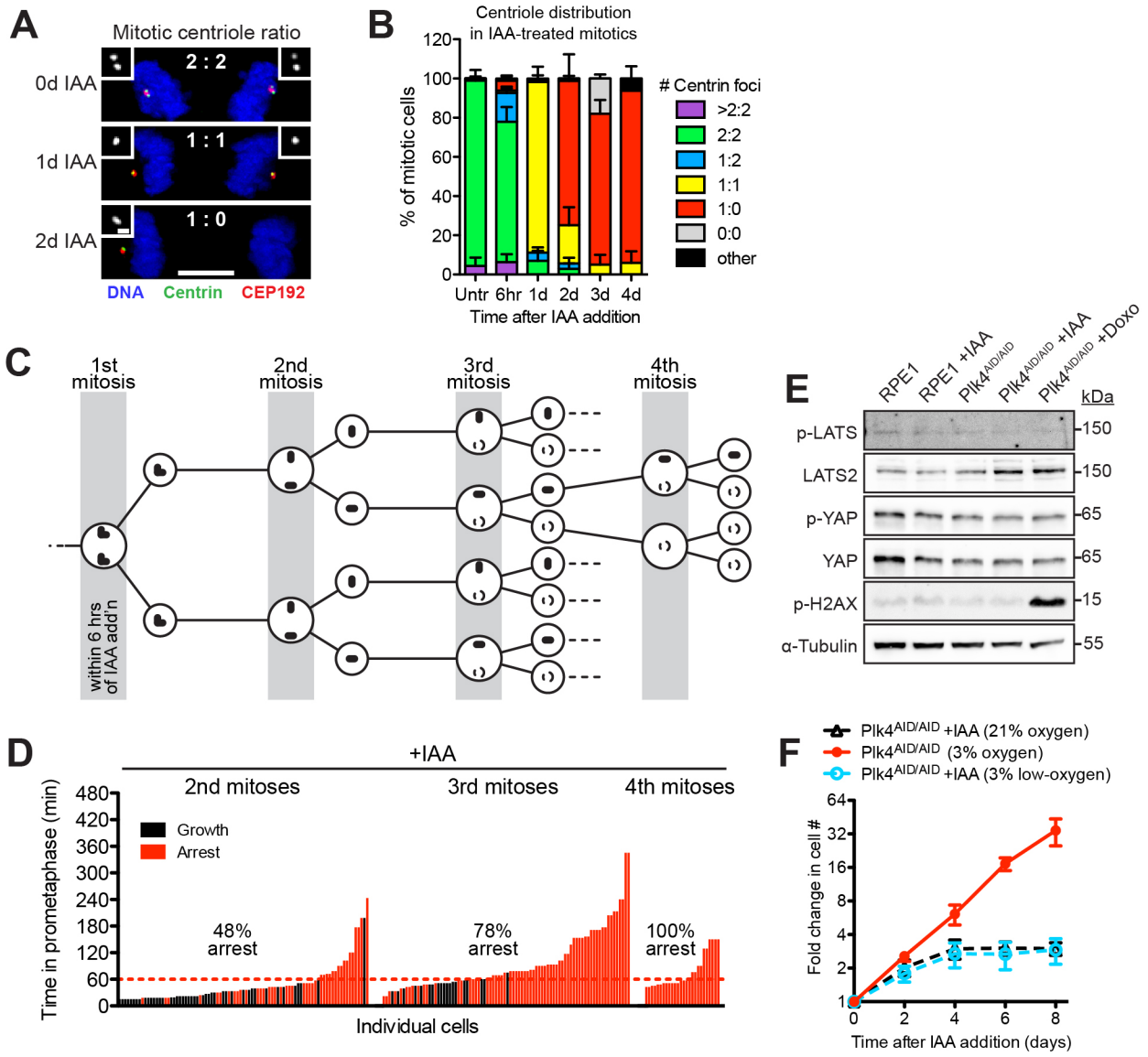

Figure 6. The IAA-induced cell-cycle arrest is not caused by a prolonged mitosis.

(A) Representative images of anaphase cells at indicated times after IAA addition. Cells were co-stained with Centrin and CEP192. Scale bars: 5 μm (main); 0.5 μm (inset).

(B) Quantification of the percentage of cell divisions occurring with the indicated number of centrioles at each spindle pole. Measurements were obtained from fixed samples at the indicated times after IAA addition. Bars represent the mean of > 60 cells from two independent experiments.

(C) Schematic showing the expected dynamics of centriole dilution following IAA treatment. Cells that undergo mitosis within 6 hours of IAA addition almost always contain 4 centrioles, which dilute out as shown in subsequent divisions.

(D) Graph showing the prometaphase duration and proliferative capacity of IAA-treated $Plk4^{AID/AID}$ cells. Each bar represents a daughter cell; its height represents the prometaphase duration of the mother cell, and its color represents the fate of the daughter. Only cells that underwent their first mitosis within 6 hours of IAA treatment were analyzed. The dashed red line indicates the maximum time that IAA-treated cells spend in prometaphase before undergoing a cell cycle arrest (See Supplemental Figure S3D). Data is taken from two independent experiments (n=199 prometaphases).

(E) Immunoblot showing the levels of phosphorylated LATS, YAP and Histone H2AX in IAA-treated $Plk4^{AID/AID}$ and parental RPE1 cells. Doxorubicin treatment was used as a control to induce DNA damage.

(F) Graph showing the fold increase in cell number in IAA-treated $Plk4^{AID/AID}$ cells grown in normal (21%) or low (3%) oxygen conditions. Points show the mean of two independent experiments performed in triplicate. All error bars in the Figure represent the S.E.M.

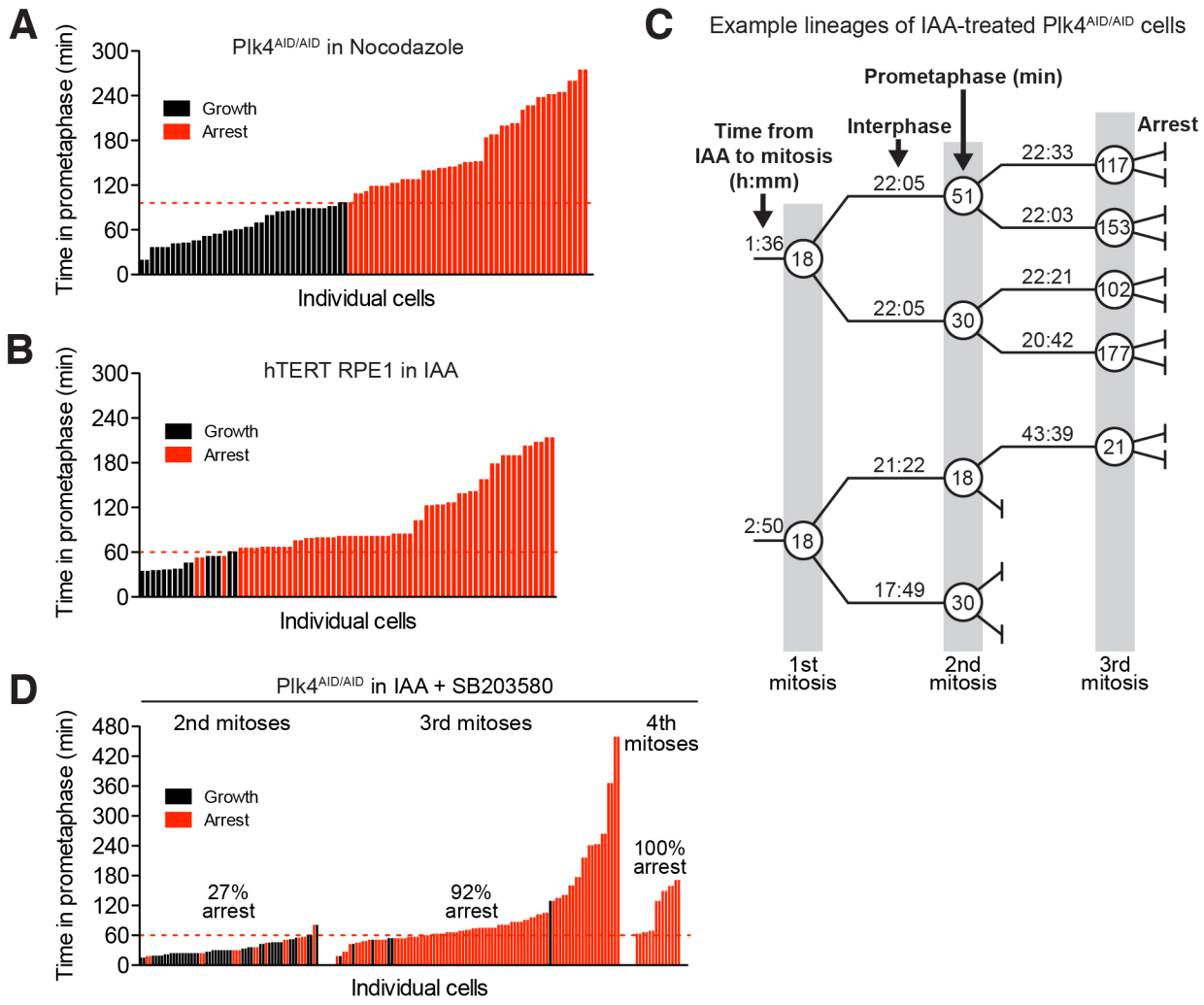

Figure 7. Inhibiting the activity of p38 MAPK does not prevent the cell cycle arrest caused by centriole duplication failure.

(A-B) Graph showing the prometaphase duration and proliferative capacity of Plk4$^{AID/AID}$ cells or parental RPE1 cells. Each bar represents a daughter cell; its height represents the prometaphase duration of the mother cell, and its color represents the fate of the daughter. The dashed red line indicates the maximum time that cells spend in prometaphase before undergoing a cell cycle arrest.

Plk4$^{AID/AID}$ cells were treated with 0.08 μM Nocodazole for the first 6 hours of imaging, while IAA was administered to parental RPE1 cells throughout the experiment. Data were acquired in a single experiment (n=87 and n=77 prometaphases, respectively)

(C) Example lineages taken from the analysis presented in Figure 4D. Note that daughter cells can undergo symmetric or asymmetric fates.

(D) Cells were analyzed as in (*A*-*B*). Only cells that underwent their first mitosis within 6 hours of IAA treatment were analyzed. IAA and SB203580 were administered throughout the experiment. Data was taken from two independent experiments (n=166 prometaphases).

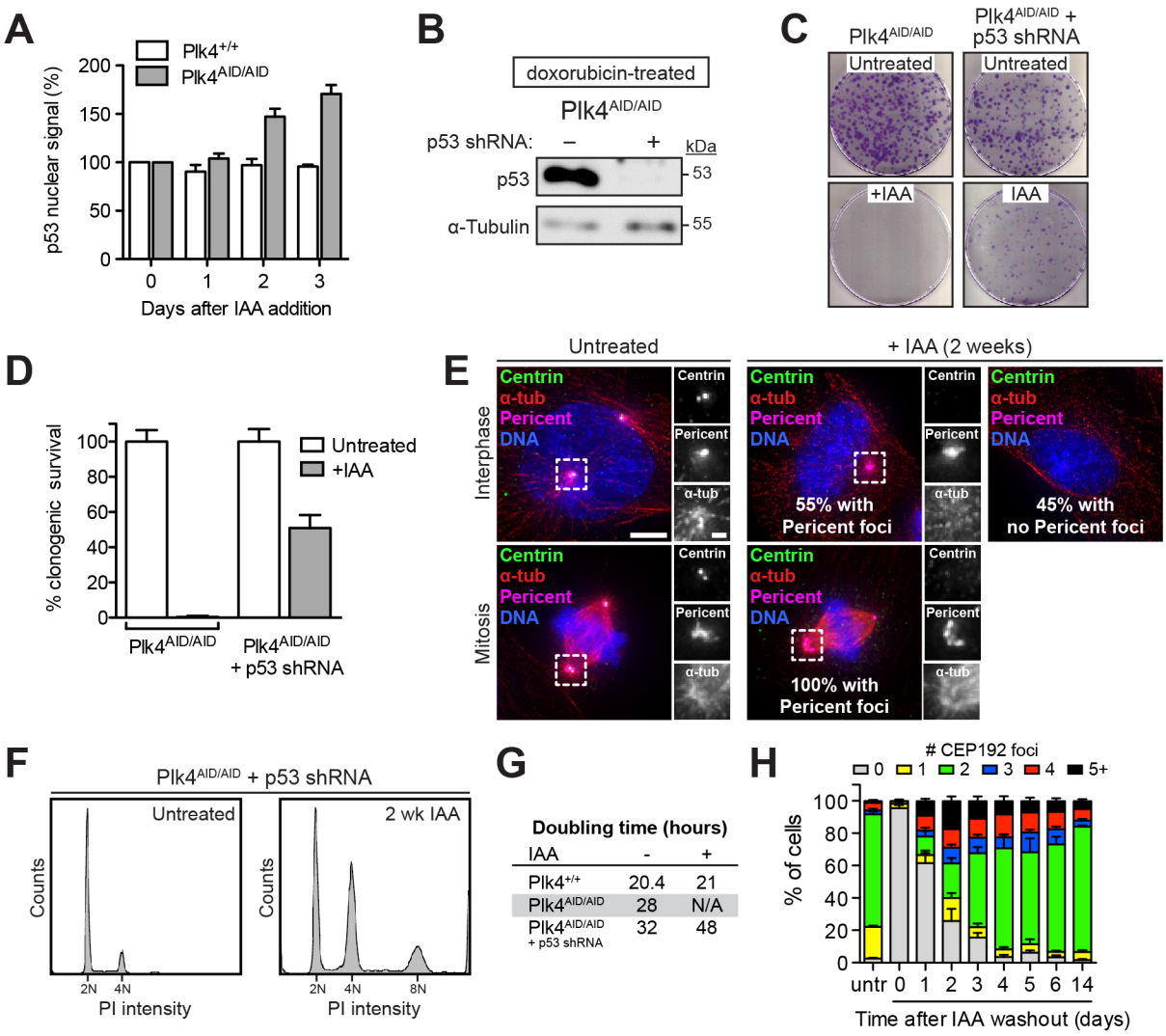

Figure 8. Cell cycle progression and spindle assembly in the absence of centrioles.

(A) Quantification of the relative level of nuclear p53 in fixed samples at the indicated times after IAA addition. p53 levels increase following Plk4 degradation. Bars represent the mean of > 200 cells from at least two independent experiments.

(B) Immunoblot showing the level of p53 in doxorubicin-treated cells.

(C) Representative images of crystal violet stained colonies formed two weeks after addition of IAA.

(D) Quantification of the percent clonogenic survival of the indicated cell lines. p53 knockdown partly rescues the clonogenic survival of cells lacking Plk4. Bars represent the mean of at least two independent experiments carried out in triplicate. All error bars in the Figure represent the S.E.M.

(E) Representative images of untreated control or acentriolar cells immunostained with α-Tubulin, Pericentrin and Centrin. Scale bars: 5 μm (main); 1 μm (inset).

(F) Flow cytometry cell cycle analysis showing an increase in polyploidy in acentriolar cells.

(G) Table displaying the doubling time of the indicated cell lines in the presence and absence of auxin. Doubling times were calculated from the growth curves shown in Figure 3A and 5A.

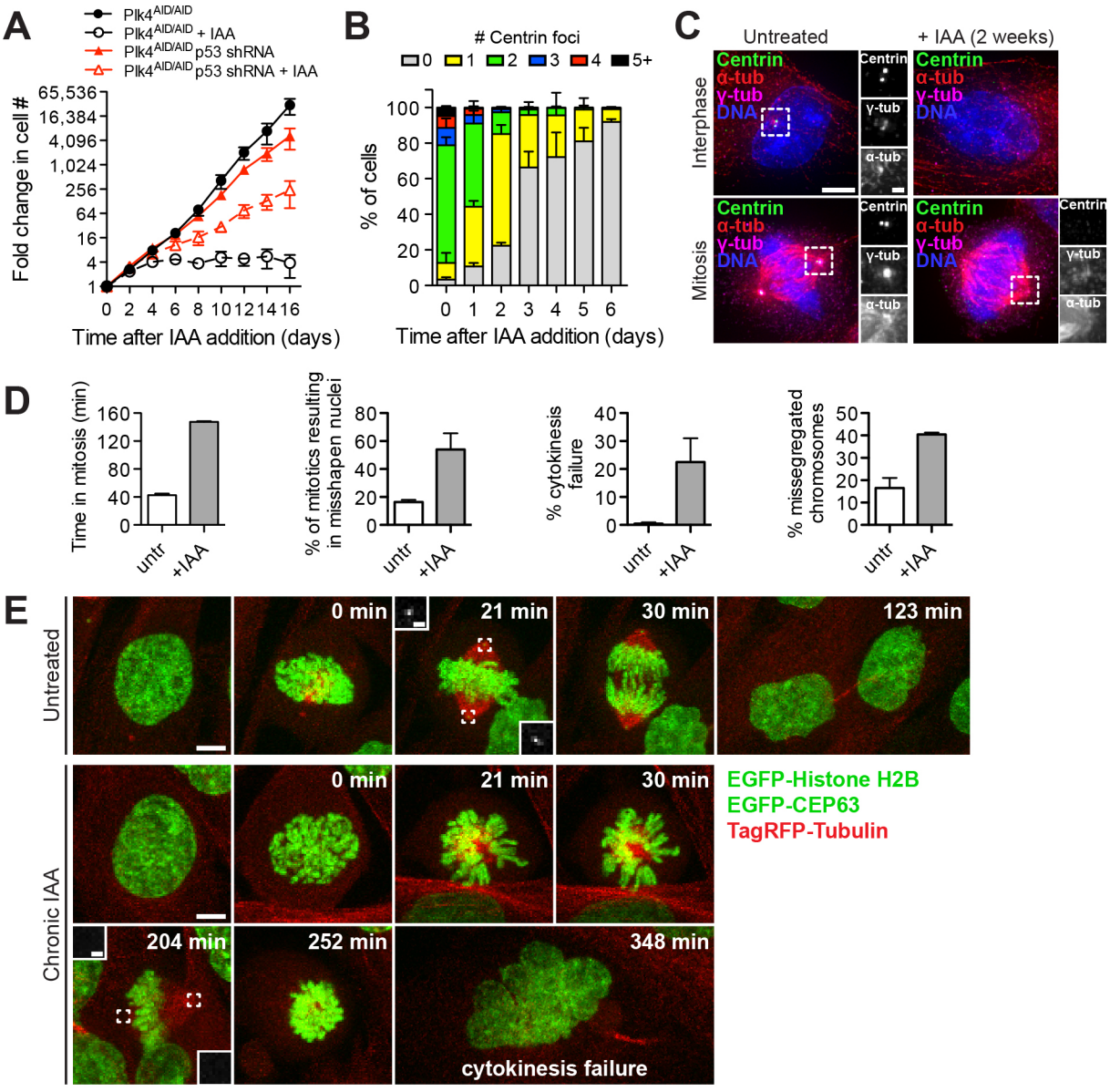

Figure 9. Depletion of p53 allows continued growth in the absence of Plk4.

(A) Graph showing the fold increase in cell number after IAA addition. Points show the mean of at least two independent experiments performed in triplicate.

(B) Quantification of the number of Centrin foci per cell in interphase at indicated times after IAA addition. Bars represent the mean of > 150 cells from two independent experiments.

(C) Selected images of untreated control or acentriolar Plk4$^{AID/AID}$;p53 shRNA cells immunostained with α-Tubulin, γ-Tubulin and Centrin. Scale bars: 5 μm (main); 1 μm (inset).

(D) Quantification of the duration of mitosis, the frequency of divisions resulting in the formation of misshapen nuclei and the frequency of cytokinesis failure and chromosome missegregation in acentriolar Plk4$^{AID/AID}$;p53 shRNA cells. Bars represent the mean of > 100 cells from two independent experiments. All error bars in the Figure represent the S.E.M.
(E) Selected images from a time-lapse series of untreated control or acentriolar Plk4$^{AID/AID}$;p53 shRNA cells co-expressing histone TagRFP-Tubulin, EGFP-Histone H2B and EGFP-CEP63. Insets show EGFP-CEP63 at the centrosome. The acentriolar cell spends longer in mitosis and fails cytokinesis. Time is indicated in minutes relative to nuclear envelope breakdown (time point 0). Scale bars: 5 μm (main); 1 μm (inset).

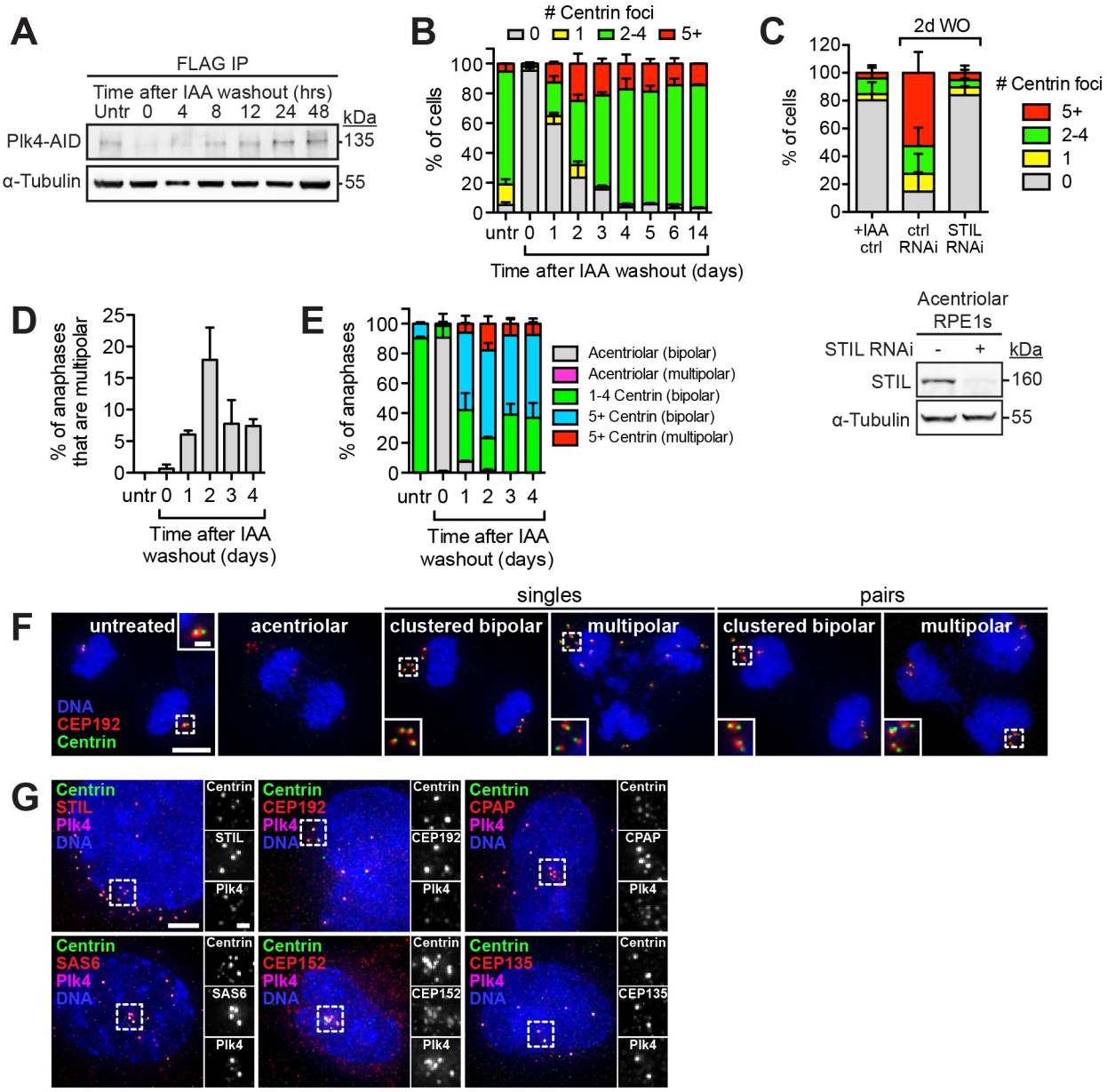

Figure 10. Restoration of Plk4 levels in acentriolar cells leads to *de novo* centriole formation.

(A) Immunoblot showing the level of immunoprecipitated endogenous Plk4-AID-FLAG at the indicated times after IAA washout in acentriolar, Plk4$^{AID/AID}$;p53 shRNA cells.

(B) Quantification of the number of Centrin foci per interphase cell at indicated times after IAA washout, in $Plk4^{AID/AID}$;p53 shRNA cells. Bars represent the mean of > 200 cells from three independent experiments.

(C) (Top) Quantification of the number of Centrin-marked *de novo* centrioles in interphase cells at 2 days after IAA washout (WO). Cells were transfected with the STIL siRNA 24 hours prior to IAA washout. (Bottom) Immunoblot showing depletion of STIL at 48 hours after transfection with STIL siRNA.

(D-E) Quantification of the fraction of bipolar and multipolar divisions in $Plk4^{AID/AID}$;p53 shRNA at indicated times after IAA washout. Bars represent the mean of > 120 cells from two independent experiments. All error bars in the Figure represent the S.E.M.

(F) Selected images of anaphase phenotypes. Both single and pairs of *de novo* centrioles clustered at the poles of the mitotic spindle. Cells were co-stained with Centrin and CEP192. Scale bars: 5 μm (main); 1 μm (inset).

(G) Selected images of Centrin-marked *de novo* centrioles at 1 day after IAA washout. Cells were co-stained with Plk4, STIL, SAS6, CPAP, CEP192, CEP152 and CEP135. Scale bars: 5 μm (main); 1 μm (inset).

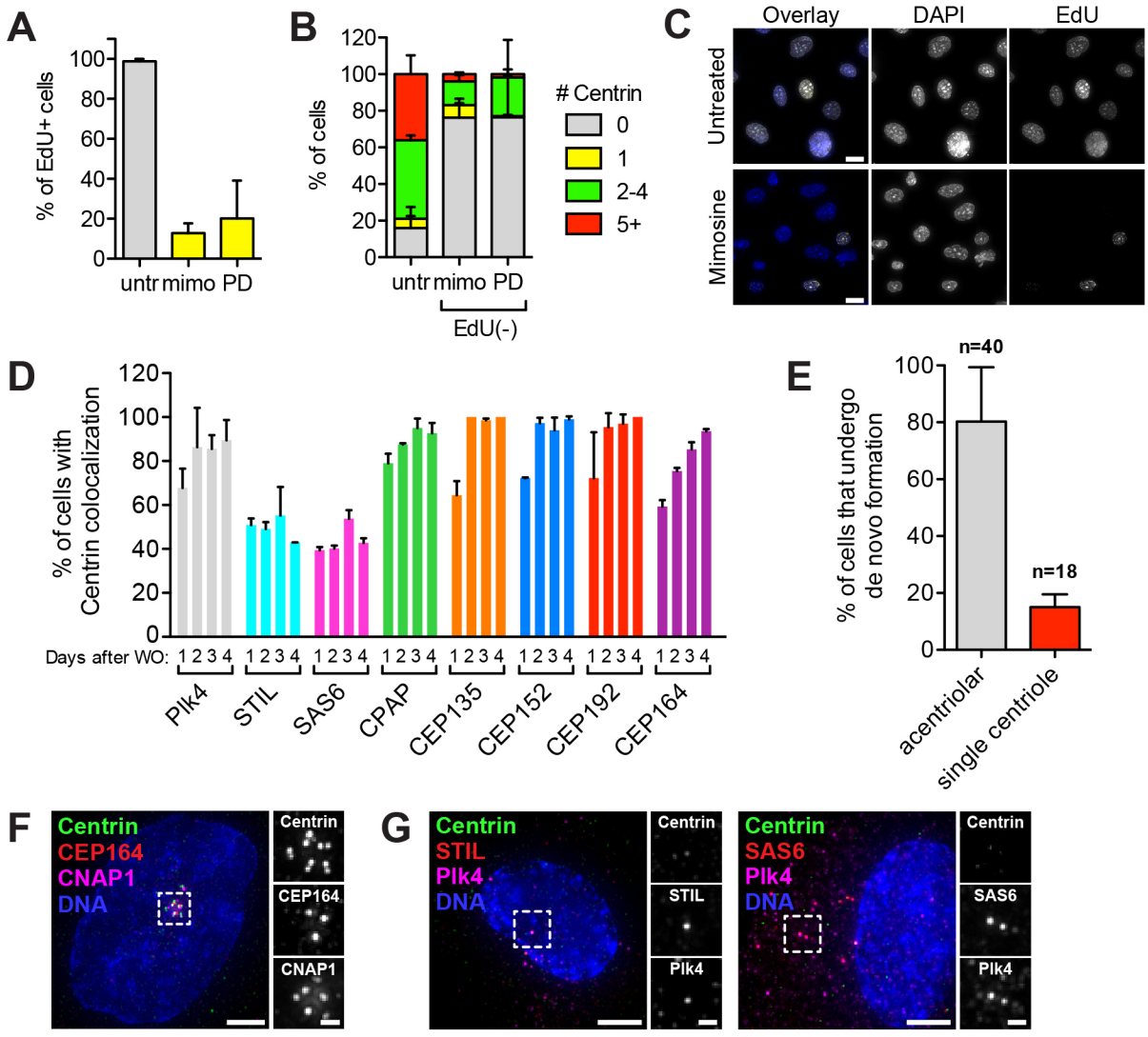

Figure 11. *De novo* centriole formation requires cell cycle progression.

(A) Quantification of the fraction of EdU-positive cells. Measurements were made two days after release from IAA in the presence or absence of mimosine or PD0332991. Bars represent the mean of > 30 cells.

(B) Quantification of the fraction of Centrin foci in interphase cells. Measurements were made two days after release from IAA in the presence or absence of mimosine or PD0332991. Bars represent the mean of > 30 cells.

(C) Selected images of control untreated and mimosine treated cells at 2 days after IAA washout. Cells were co-stained with DAPI and EdU. Scale bars, 20 μm.

(D) Quantification of the fraction of interphase cells with Centrin-marked *de novo* centrioles that co-localize with the indicated centriole components. Quantification was derived from fixed images taken 1, 2, 3 and 4 days after IAA washout. Bars represent the mean of > 40 cells from two independent experiments.

(E) Quantification of the fraction of cells that underwent *de novo* centriole formation. Acentriolar and single centriole-containing cells expressing EGFP-Centrin were tracked for 60 hours by time-lapse microscopy. Bars represent the mean of two independent experiments. All error bars in the Figure represent the S.E.M.

(F) Image of *de novo* centrioles at 3 days after IAA washout. Cells were co-stained with CEP164, CNAP1 and Centrin. Scale bars: 5 μm (main); 1 μm (inset).

(G) Selected images of control *de novo* centrioles at 1 day after IAA washout. Cells were co-stained with Centrin, Plk4 and STIL. Plk4 and STIL form foci that do not co-localize with Centrin and likely represent sites of nascent *de novo* centriole formation. Scale bars: 5 μm (main); 1 μm (inset).

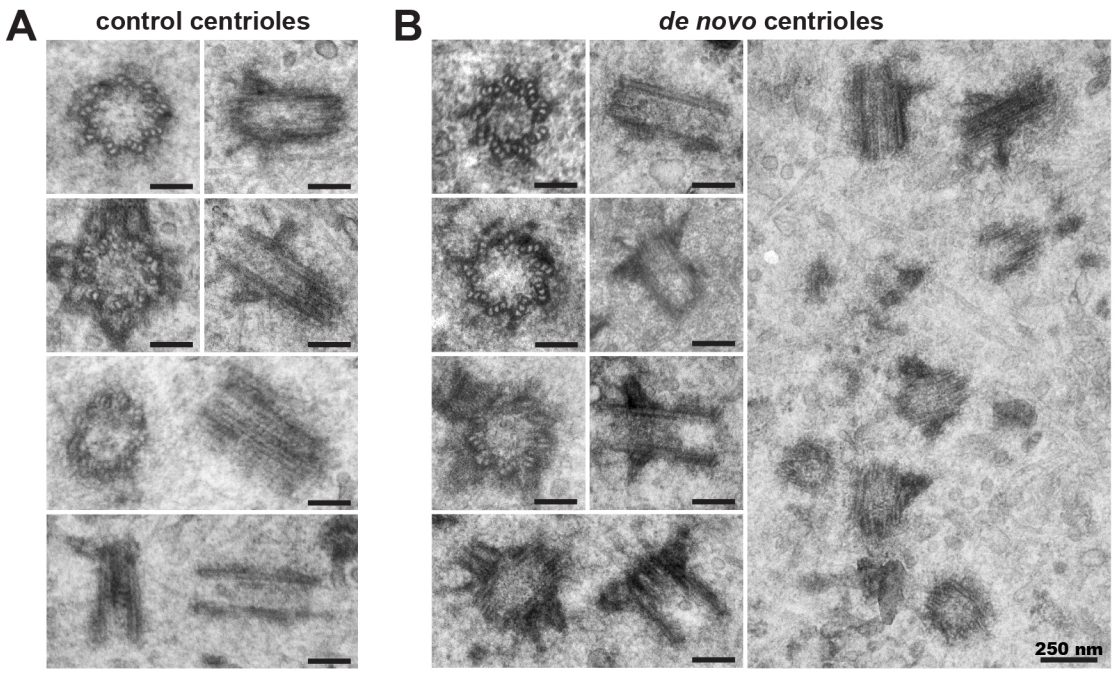

Figure 12. *De novo* formed centrioles have a normal structure.

(A) – (B) Thin section transmission electron micrographs of *(A)* existing centrioles or *(B)* de novo centrioles formed at 3 days after IAA washout. Scale bars 100 nm unless indicated otherwise.

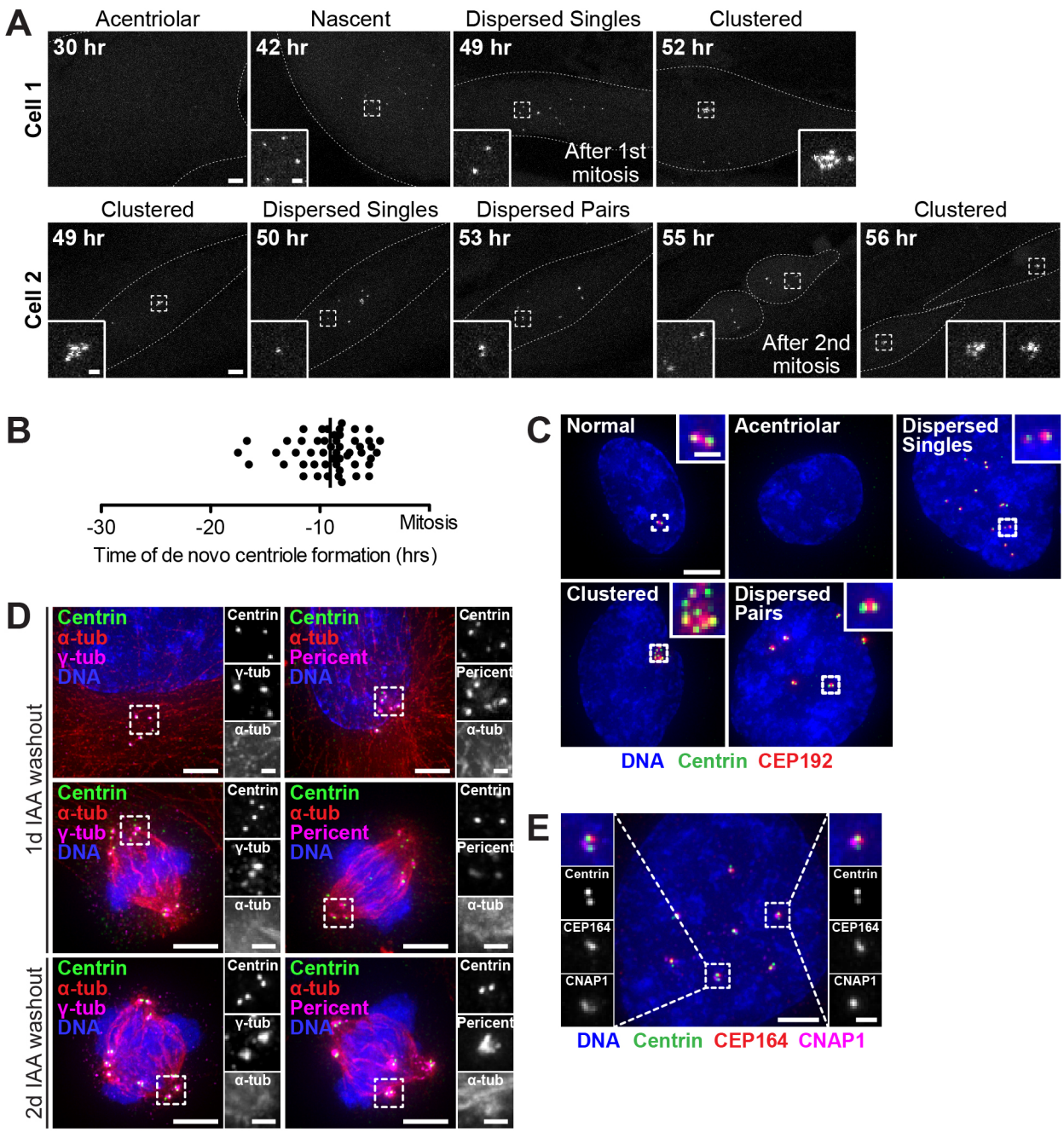

Figure 13. *De novo* centrioles recruit PCM and act as MTOCs.

(A) Selected images from a time-lapse series showing de novo centriole formation in cells expressing histone EGFP-Centrin. *De novo* centrioles duplicate in the second cycle after they are born. Time is indicated in hours relative to the time of IAA washout (time point 0). Scale bars: 5 μm (main); 1 μm (inset).

(B) Quantification of the time of *de novo* centriole formation relative to the time of cell division. Measurements were made using time-lapse movies of EGFP-Centrin expressing cells from two independent experiments. Line represents the mean of > 50 cells.

(C) Selected images illustrating the different configurations adopted by *de novo* centrioles. Cells were co-stained with Centrin and CEP192 to identify centrioles. Scale bars: 5 μm (main); 1 μm (inset).

(D) Selected images of *de novo* centrioles in interphase and mitotic cells at 1 and 2 days after IAA washout. The mitotic spindle segregates freestanding de novo centrioles in the first division and pairs of replicated centrioles in the second cell division. Cells were co-stained with α-Tubulin, Centrin and γ-Tubulin or Pericentrin. Scale bars: 5 μm (main); 1 μm (inset).

(E) Selected images of pairs of *de novo* centrioles in interphase cells at 2 days after IAA washout. Cells were co-stained with Centrin, CNAP1 and CEP164. Scale bars: 5 μm (main); 1 μm (inset).

Chapter 3

Identification of a mitotic surveillance pathway

Modified from: Lambrus BG*, Daggubati V*, Uetake Y, Scott PM, Clutario KM, Sluder G, Holland AJ. (2016) A USP28–53BP1–p53–p21 signaling axis arrests growth after centrosome loss or prolonged mitosis. *Journal of Cell Biology*. doi: 10.1083/jcb.201604054. (*Co-first authors).

3.1 Introduction

As discussed in the previous chapter, inhibition of Plk4 kinase activity or induced degradation of Plk4 leads to centrosome loss and a p53-dependent cell cycle arrest within a few cell divisions (Lambrus et al., 2015; Wong et al., 2015c). This arrest was not due to mitotic errors, Hippo pathway activation, p38-mediated stress signaling, or DNA damage (Lambrus et al., 2015; Wong et al., 2015c). Genetic inactivation of the centriole protein SAS4 in the mouse embryo or in the developing mouse brain also results in centrosome loss, delayed spindle assembly and p53-dependent apoptosis (Bazzi and Anderson, 2014; Insolera et al., 2014). Together, these studies implicate the existence of a new signaling pathway that activates p53 in response to a signal linked to centrosome loss. For simplicity, we hereafter refer to this pathway as the 'centrosome surveillance pathway'.

While centrosomes are required for the sustained proliferation of non-transformed mammalian cells, a wide array of tumor cells are able to continue to proliferate after centrosome loss (Wong et al., 2015c). Cell divisions that lack centrosomes are error-prone (Debec et al., 2010; Khodjakov and Rieder, 2001; Lambrus et al., 2015; Sir et al., 2013), suggesting that the centrosome surveillance pathway could protect against genome instability by preventing the growth of cells with too few centrosomes. Nevertheless, it remains unclear how p53 is activated in response to centrosome loss in mammalian cells. In this manuscript, we explore the genetic basis for signaling through the centrosome surveillance pathway.

3.2 A chemical genetic system to activate the centrosome surveillance pathway

We set out to develop a chemical genetic system to specifically inhibit Plk4 kinase activity and induce centrosome loss in human cells. Mutation of a single amino acid in the ATP-binding pocket of Plk4 creates an analog-sensitive (AS) kinase that can be inhibited with non-hydrolyzable, bulky ATP analogs **(Fig. 14A)** (Holland et al., 2010b; Moyer et al., 2015). We used CRISPR/Cas9 to knock-in the Plk4 AS mutation (L89G) into the endogenous Plk4 locus in non-transformed hTERT-RPE1 cells **(Fig. 14B)**. A clone was identified carrying a frame-shift, knockout mutation in one Plk4 allele and an AS knock-in mutation in the second allele. The $Plk4^{AS/-}$ cells (hereafter referred to as $Plk4^{AS}$) proliferated at the same rate as the parental cells and contained normal numbers of centrioles **(Fig. 14C-D)**. As expected, inhibition of Plk4 kinase activity with 3MB-PP1 led to an increase in Plk4 levels at the centrosome and a failure of centriole duplication (**Fig. 15A and 1C**).

While RPE1 cells proliferated normally in the presence of 3MB-PP1, addition of 3MB-PP1 to Plk4^{AS} cells resulted in a penetrant G1 cell cycle arrest after 3 days **(Fig. 14D and Fig. 15B)**. As a consequence, centriole loss ceased after 4 days of treatment with 3MB-PP1 **(Fig. 14C)**. To evaluate the long-term growth potential of cells that lack Plk4 kinase activity, we performed clonogenic survival assays. 3MB-PP1 addition prevented colony formation in Plk4^{AS} RPE1 cells, but did not affect the survival of parental RPE1 cells **(Fig. 15C).** The arrest was not caused by oxidative stress, as growth in low oxygen (3% O_2) did not allow continued growth following centrosome loss **(Fig. 15D)**. A similar growth arrest was previously reported in RPE1 cells that lose centrosomes as a result of destruction of endogenous Plk4 or treatment with the ATP-competitive Plk4 inhibitor centrinone (Lambrus et al., 2015; Wong et al., 2015c). We conclude that inhibition of Plk4^{AS} kinase activity provides a system to activate the centrosome surveillance pathway in RPE1 cells.

3.3 Genome-scale CRISPR/Cas9 knockout screen to identify components of the centrosome surveillance pathway

To identify novel components of the centrosome surveillance pathway, we used Plk4^{AS} RPE1 cells to perform a genome-wide, loss-of-function CRISPR/Cas9 screen. We generated Plk4^{AS} cells stably expressing the SpCas9 endonuclease and transduced them with a genome-wide sgRNA library (Shalem et al., 2014). Knockout libraries of RPE1 Plk4^{AS} cells were cultured in the presence of DMSO or 3MB-PP1 for 42 days. Cells that lacked genes required for the centrosome surveillance pathway were expected to proliferate in the absence of Plk4 kinase activity and enrich in the 3MB-PP1 treated population compared to DMSO treated controls **(Fig. 16A)**. Deep sequencing revealed that the sgRNA distribution in 3MB-PP1 treated cells was

significantly different compared with DMSO treated cells **(Fig. 16B)**. The two highest-ranking genes in the screen were p53 and 53BP1 (FDR <0.05.) **(Fig. 16C, D and Fig. 15E)**. Importantly, 53BP1 interacts directly with p53, but has not been previously implicated in the centrosome surveillance pathway (Iwabuchi et al., 1994; Joo et al., 2002).

To confirm 53BP1 as a novel hit, we repeated the CRISPR/Cas9 screen in SpCas9-expressing hTERT-RPE1 cells using the Plk4 inhibitor centrinone (Wong et al., 2015c). p53 and 53BP1 emerged again as the top hits from this screen (FDR <0.05) **(Fig. 16E-G)**. To validate the role of 53BP1 in the centrosome surveillance pathway, we generated knockouts of p53 and 53BP1 in $Plk4^{AS}$ cells. Inactivation of p53 or 53BP1 dramatically increased the clonogenic survival of $Plk4^{AS}$ cells treated with 3MB-PP1 **(Fig. 16H and 15F)**. Thus, our unbiased, genome-scale screening identified 53BP1 as a novel component of the centrosome surveillance pathway.

3.3.1 53BP1 is required to stabilize p53 following centrosome loss

Knockout of p53 did not alter the levels of 53BP1 and vice-versa, showing these proteins are not required for one another's stability **(Fig. 17A, B)**. To test whether cells lacking 53BP1 lose centrosomes in the absence of Plk4 activity, we examined centriole number in p53 and 53BP1 knockout $Plk4^{AS}$ cells over the course of a week following Plk4 inhibition. Treatment of $p53^{-/-}$ or $53BP1^{-/-}$ $Plk4^{AS}$ cells with 3MB-PP1 led to a gradual reduction in centriole number as cells failed centriole duplication, but continued to divide. At 6 days after 3MB-PP1 treatment, >90% of p53 and 53BP1 knockout cells lacked centrioles **(Fig. 17C-D)**.

Centrosome loss increased total cellular and nuclear p53 levels **(Fig. 17E and 18A)**. Importantly, knockout of 53BP1 prevented p53 stabilization in response to centrosome loss, suggesting that 53BP1 functions upstream of p53 in the centrosome surveillance pathway **(Fig. 17F and 18A)**. Knockout of 53BP1 did not, however, prevent stabilization of p53 in response to doxorubicin-induced DNA damage **(Fig. 18A)**, showing that 53BP1 is not required for all p53-dependent responses.

3.3.2 USP28 functions together with 53BP1 to stabilize p53 following centrosome loss

We considered the possibility that during the selection period for the CRIPSR/Cas9 screen, sgRNAs that provide a modest growth advantage in cells lacking centrosomes may be outcompeted by the faster growth of cells containing sgRNAs targeting p53 or 53BP1. To investigate whether weaker hits may have been overlooked, we created knockouts for the top 40 ranked genes and analyzed the ability of each sgRNA to promote the growth of $Plk4^{AS}$ cells in the presence of 3MB-PP1 **(Fig. 14E)**. Other than p53 and 53BP1, USP28 (ranked #29) was the only other sgRNA target that provided a significant growth advantage in $Plk4^{AS}$ cells grown in 3MB-PP1 **(Fig. 17G-H and 15E-F)**. Importantly, USP28 is a deubiquitinating enzyme that has been shown to interact with 53BP1 (Zhang et al., 2006).

Knockout of USP28 did not alter basal levels of p53, or prevent p53 stabilization in response to doxorubicin-induced DNA damage **(Fig. 16I, 18A-B)**. However, $USP28^{-/-}$ cells failed to stabilize p53 in response to centrosome loss **(Fig. 17J and 18A**). Cell lacking USP28 grew continually in the absence of Plk4 activity and consequently >90% of USP28 knockout cells lacked centrioles

after 6 days of 3MB-PP1 treatment **(Fig. 17K-L and 18C)**. These data demonstrate that USP28 acts together with 53BP1 to stabilize p53 in response to centrosome loss.

To examine whether USP28 or 53BP1 knockout alters basal p53 stability, we examined p53 levels after cycloheximide addition in $USP28^{-/-}$ and $53BP1^{-/-}$ cells. Loss of USP28 and 53BP1 did not alter basal p53 stability in $Plk4^{AS}$ cells **(Fig. 18D).** Furthermore, inhibiting p53 binding to MDM2 with Nutlin-3 elevated p53 levels to a similar extent in wild type, $USP28^{-/-}$, and $53BP1^{-/-}$ $Plk4^{AS}$ cells **(Fig. 18E)**. We conclude that USP28 and 53BP1 do not alter p53 regulation by MDM2 or modulate basal p53 stability.

Inhibition of Plk4 kinase activity could have consequences in addition to prompting a failure of centriole duplication. We therefore tested whether loss of SAS6, a conserved structural component required for centriole assembly, also prevents cell growth, and whether this can be overcome by inactivating components of the centrosome surveillance pathway (Dammermann et al., 2004; Leidel et al., 2005). Consistent with its essential role in cell growth, we were unable to generate SAS6 knockout clones in hTERT-RPE1 cells **(Fig. 18F)**. We did, however, identify multiple clones of $USP28^{-/-}$, $53BP1^{-/-}$ and $p53^{-/-}$ cells that lacked SAS6 and centrosomes. These data suggest that centrosome loss, and not loss of Plk4 kinase activity *per se*, is responsible for activating the centrosome surveillance pathway.

3.3.3 p21 acts downstream of p53 in the centrosome surveillance pathway

The cyclin-dependent kinase inhibitor p21 (CDKN1A) is a transcriptional target of p53 that is responsible for promoting a p53-dependent G1 arrest in response to a variety of stress stimuli.

Since p21 also emerged as a weak hit in the CRISPR/Cas9 screen (ranked #146) **(Fig. 15E)**, we reasoned that p21 could contribute to the p53-dependent cell cycle arrest that occurs following centrosome loss. Indeed, p21 levels increased after Plk4 inhibition **(Fig. 18A)**. Knockout of p21 did not alter p53 abundance or prevent p53 stabilization following centrosome loss, consistent with p21 acting downstream of p53 **(Fig. 17M-N and 18A)**. p21 knockout increased the clonogenic survival of $Plk4^{AS}$ cells in the presence of 3MB-PP1 **(Fig. 17G-H and 15F)**. In addition, $p21^{-/-}$ cells grew continually in the presence of 3MB-PP1 and by 6 days after 3MB-PP1 treatment, >90% of $Plk4^{AS}$; $p21^{-/-}$ cells lacked centrioles **(Fig. 17L, O and 18C)**.

3.3.4 The centrosome surveillance pathway is not activated by DNA damage

As USP28, 53BP1 and p53 have all been shown to play a role in the DNA damage signaling pathway, we asked whether cells that fail centrosome duplication acquire DNA damage. We first used immunoblotting to examine changes in the abundance of γ-H2AX. While a brief treatment with doxorubicin increased γ-H2AX levels, no increase was observed in $Plk4^{AS}$ cells treated with 3MB-PP1 **(Fig. 19A)**. In addition, doxorubicin-induced DNA damage led to robust phosphorylation of the ATM target sites p53 Ser15 and KAP1 Ser824, but phosphorylation of these sites was undetectable in $Plk4^{AS}$ cells grown in the presence of 3MB-PP1 (Banin et al., 1998; Canman et al., 1998; White et al., 2006; Ziv et al., 2006) **(Fig. 19A)**. We next examined 53BP1 foci formation using immunofluorescence microscopy. While doxorubicin treatment led to a >4-fold increase in the number of cells with >5 53BP1 foci, no significant increase in foci formation was observed in $Plk4^{AS}$ cells following centrosome duplication failure **(Fig. 19B)**. Taken together, our data offer no evidence for elevated DNA damage in cells that lose centrosomes.

Next, we tested whether proteins that function in the DNA damage pathway are required to arrest the cell cycle following centrosome loss. Chronic treatment with the ATM inhibitor KU-55933 did not prevent a cell cycle arrest following centrosome loss **(Fig. 20A-B)**. Additionally, ATM, RNF8, Chk1 and Chk2 are components of the DNA damage response, but knockout of these genes did not abolish the centrosome surveillance pathway **(Fig. 14E)**. Importantly, while $Chk2^{-/-}$ $Plk4^{AS}$ cells did not proliferate in 3MB-PP1, loss of Chk2 attenuated DNA damage signaling and rescued cell growth in doxorubicin **(Fig. 19C-E)**. This suggests that the DNA damage response and centrosome surveillance are genetically separable pathways.

The E3 ubiquitin ligase RNF168 is required for the recruitment of 53BP1 to sites of DNA double-strand breaks (Doil et al., 2009; Huen et al., 2007; Kolas et al., 2007; Mailand et al., 2007; Mallette et al., 2012; Mallette and Richard, 2012). We created RNF168 knockout $Plk4^{AS}$ cells and confirmed that while 53BP1 is present at normal levels in these cells, it fails to localize to sites of DNA damage **(Fig. 19F-G)**. Importantly, RNF168 knockout cells ceased proliferating following centrosome loss, demonstrating that localization of 53BP1 to sites of DNA damage is not required for it to function in the centrosome surveillance pathway **(Fig. 19H)**. These data suggest that 53BP1 plays a DNA damage-independent role in signaling through the centrosome surveillance pathway.

Finally, we tested the ability of cells lacking p53, 53BP1 or USP28 to proliferate following doxorubicin-induced DNA damage. As expected, treatment of $Plk4^{AS}$ cells with doxorubicin dramatically reduced the fraction of cells that entered into S phase, as well as clonogenic survival

(Fig. 19I, 20C). While $p53^{-/-}$ cells progressed into S phase and formed colonies in the presence of doxorubicin, $USP28^{-/-}$ and $53BP1^{-/-}$ cells did not. This demonstrates that the DNA damage response remains partly intact in cells lacking USP28 and 53BP1. Taken together, our evidence strongly indicates that DNA damage is not responsible for activating the centrosome surveillance pathway.

3.4 The cell cycle arrest induced by prolonged prometaphase requires the same signaling components as the centrosome surveillance pathway

To evaluate the effect of centrosome loss on mitotic duration, we grew $p53^{-/-}$, $53BP1^{-/-}$ and $USP28^{-/-}$ $Plk4^{AS}$ cells in 3MB-PP1 for 6 days and measured the length of mitosis in cells that lack centrosomes. Loss of centrosomes dramatically extended the duration of mitosis (average of 153, 129 and 149 minutes in $p53^{-/-}$, $53BP1^{-/-}$ and $USP28^{-/-}$ cells, respectively) (**Fig. 21A**). Previous work has shown that prolonging prometaphase to >90 minutes leads to p53-dependent arrest in RPE1 cells (Uetake and Sluder, 2010). This suggests that this mitotic timer may be dysfunctional in $p53^{-/-}$, $53BP1^{-/-}$ and $USP28^{-/-}$ cells. To investigate this possibility, we first set out to determine the window of tolerance for prometaphase duration in the $Plk4^{AS}$ RPE1 cells used in this study. $Plk4^{AS}$ cells were treated with nocodazole for 6 hours, and following drug washout, the proliferative fate of daughter cells monitored by time-lapse microscopy. While 13% of daughters whose mothers spent <120 minutes in prometaphase failed to proliferate, prolonging the duration of prometaphase to >120 minutes caused a cell cycle arrest in 88% of the resulting daughters **(Fig. 21A)**. Although this response is not as robust as reported in unmodified hTERT-RPE1 cells, the mitotic timer is clearly functioning in $Plk4^{AS}$ cells (Uetake and Sluder, 2010; Wong et al., 2015c).

We next investigated whether the newly identified components of the centrosome surveillance pathway are also required to arrest cells after an increased mitotic duration. Consistent with previous work, nearly all $p53^{-/-}$ daughter cells proliferated regardless of the prometaphase duration in the preceding division **(Fig. 21B)** (Uetake and Sluder, 2010). Remarkably, knockout of USP28 and 53BP1 almost completely abolished the G1 arrest after a prolonged prometaphase. We conclude that the stresses generated by both centrosome loss and an extended prometaphase act through the same signaling components to stabilize p53 and cause a cell cycle arrest.

Since the centrosome surveillance pathway and the mitotic timer require the same components, we investigated whether activation of the mitotic timer could account for the cell cycle arrest that occurs in $Plk4^{AS}$ cells following centrosome loss. To examine the effect of centrosome loss on cell division time, we monitored $Plk4^{AS}$ cells by time-lapse microscopy at 1, 2 and 3 days after Plk4 inhibition. Untreated control cells progressed though mitosis with an average time of 25 minutes (**Fig. 21C**). Mitotic duration increased as cells progressed through successive divisions in the absence of Plk4 activity (average of 40 minutes at day 1, 60 minutes at day 2 and 65 minutes at day 3 after 3MB-PP1 addition). Nevertheless, no mitosis exceeded a duration required to activate the mitotic timer (>120 minutes), suggesting that activation of the centrosome surveillance pathway cannot be simply explained by an increase in duration of a single division.

3.5 Distinct signal transduction cascades activate p53 in response to centrosome amplification or centrosome loss

We previously showed that Plk4 overexpression promotes centrosome amplification and a p53-dependent cell cycle arrest in hTERT-RPE1 cells (Holland et al., 2012b). We therefore tested whether the proteins required to block proliferation following centrosome loss are also required to prevent cell growth in the presence of extra centrosomes. While knockout of p53, and to a lesser extent p21, allowed for the growth of Plk4 overexpressing cells with supernumerary centrosomes, knockout of 53BP1 and USP28 did not (**Fig. 20D**). A recent study showed that extra centrosomes trigger activation of the Hippo pathway kinase LATS2, which in turn stabilizes p53 (Ganem et al., 2014). However, knockout of LATS1 or LATS2 did not prevent growth arrest in cells following either centrosome loss or gain **(Fig. 20E-F)**. Taken together, these data suggest that distinct signaling pathways activate p53-p21 in response to centrosome loss or the presence of excess centrosomes **(Fig. 21D)**.

3.6 Discussion

Our results reveal the existence of a USP28-53BP1-p53-p21 signaling axis that arrests cell cycle progression following centrosome loss. USP28 and p53 both bind to 53BP1 through the tandem C-terminal BRCT repeats (Joo et al., 2002; Knobel et al., 2014). We, therefore, speculate that 53BP1 could recruit USP28 to deubiquitinate and stabilize p53 in response to centrosome loss **(Fig. 21D)**. Although DNA breaks trigger p53 activation, several lines of evidence strongly suggest that DNA damage is not responsible for activating the centrosome surveillance pathway. First, there is no detectable DNA damage in cells that fail centrosome duplication. Second, knockout of *bona fide* DNA damage components, including ATM, Chk1, Chk2, RNF8 and

RNF168 do not prevent cell cycle arrest following centrosome loss. Third, preventing 53BP1 localization to sites of DNA damage prevents DNA damage-dependent functions of 53BP1, but does not prevent the growth arrest after a failure of centrosome duplication. Finally, while loss of USP28 or 53BP1 prevents activation of p53 in response to centrosome loss, their loss does not prevent p53 stabilization and cell cycle arrest in cells treated with the DNA damaging agent doxorubicin.

At present the mechanism by which cells 'sense' centrosome loss remains unclear. While it is possible that the centrosome surveillance pathway directly monitors centrosome number, we feel this is unlikely for two reasons. First, p53, 53BP1, and USP28 do not localize to the centrosome in RPE1 cells **(Fig. 20G)**. Second, our evidence suggests that there are distinct pathways that activate p53 in cells with either too few or too many centrosomes, arguing against a common mechanism for detecting the wrong number of centrosomes. We, therefore, favor the interpretation that p53 activation is indirectly triggered by a stress associated with cell cycle progression following centrosome loss.

We have shown that, as well as being required for the centrosome surveillance pathway, USP28, 53BP1, and p53 are also required to prevent the growth of cells that delay in mitosis. This raises the possibility that the centrosome surveillance pathway is activated by a prolonged mitosis. Nevertheless, cells that fail centriole duplication delay in mitosis, but do not exceed a mitotic duration in a single division that is sufficient to activate the mitotic timer (Lambrus et al., 2015; Wong et al., 2015c). Since cells that fail centrosome duplication typically undergo 3-4 cell divisions before they cease proliferating, it is possible that the cumulative stress from successive

delayed cell divisions eventually passes a threshold that triggers an arrest in cells failing centrosome duplication. Interestingly, 53BP1 localizes to unattached kinetochores in prometaphase, suggesting that it could play a signaling role during mitosis **(Fig. 20G)** (Jullien et al., 2002). Determining whether kinetochore localization of 53BP1 is required for the centrosome surveillance pathway and mitotic timer is an important area of future work.

3.7 Figures and Legends

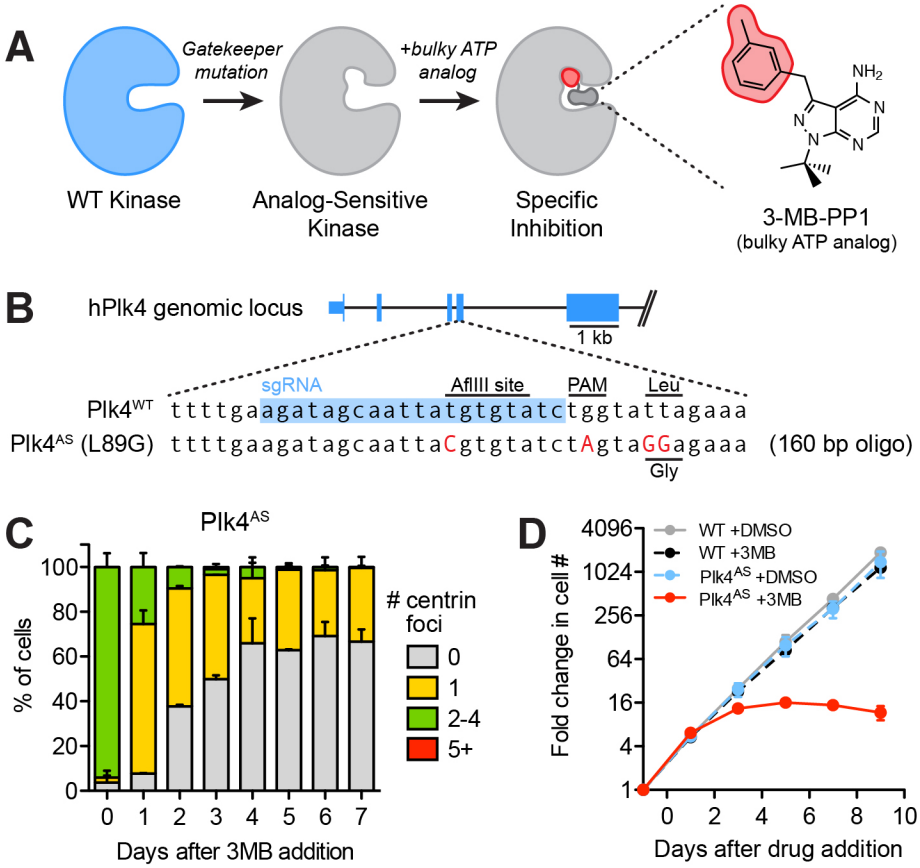

Figure 14. Inhibition of analog-sensitive Plk4 leads to centrosome loss and growth arrest.

(A) Principle of analog-sensitive Plk4 and its inhibition by 3MB-PP1.

(B) Schematic of sgRNA and repair template oligo used to knock-in the analog-sensitive mutation at endogenous Plk4 genomic loci. sgRNA sequence is highlighted in blue, and edited nucleotides are displayed in red.

(C) Centriole number distribution in interphase $Plk4^{AS}$ cells at time points after addition of 3MB-PP1. Data are means ± SEM of three independent experiments ($N = 3$) with >80 cells per experiment.

(D) Fold increase in cell number after 3MB-PP1 addition. Data are means ± SEM ($N = 2$, performed in triplicate).

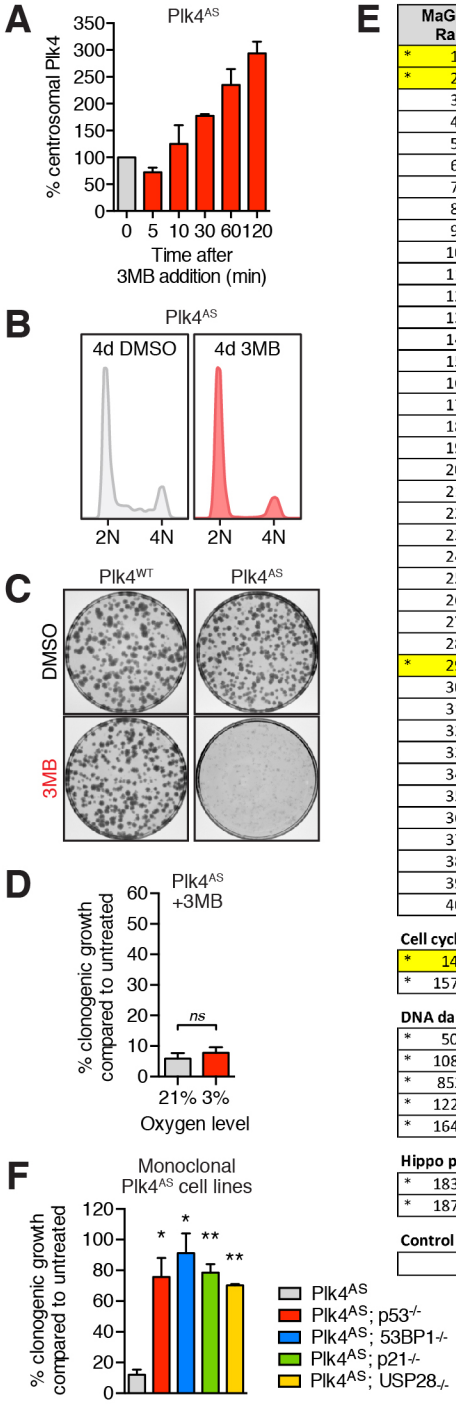

E

MaGeCK Rank	Gene name	*p*-value	FDR	# enriched sgRNAs	% clonogenic growth
* 1	TP53BP1 (53BP1)	2.26 * 10-7	0.0050	3	63.0 ± 1.1
* 2	TP53 (p53)	4.29 * 10-6	0.047	3	71.8 ± 10.4
3	CD5	8.96 * 10-5	0.54	1	6.5
4	B4GALT7	9.86 * 10-5	0.54	3	4.1
5	RND1	2.54 * 10-4	0.79	1	6.0
6	SLC23A3	3.11 * 10-4	0.79	3	5.1
7	TRPC7	4.05 * 10-4	0.79	1	4.7
8	DMRTC1B	4.21 * 10-4	0.79	3	7.1
9	GOLGA6B	4.21 * 10-4	0.79	2	6.5
10	PDIK1L	5.38 * 10-4	0.79	1	3.3
11	GNA12	6.85 * 10-4	0.79	2	9.4
12	LTBP3	6.85 * 10-4	0.79	3	4.6
13	DNASE1	6.85 * 10-4	0.79	3	3.8
14	DCTD	6.85 * 10-4	0.79	3	6.1
15	SLC10A3	6.85 * 10-4	0.79	3	3.5
16	CHRD	6.85 * 10-4	0.79	3	5.4
17	ZNF618	8.18 * 10-4	0.79	2	6.3
18	TIGD4	9.40 * 10-4	0.79	1	6.0
19	CPPED1	1.04 * 10-3	0.79	3	1.8
20	POTEG	1.04 * 10-3	0.79	2	2.1
21	MAP1LC3B2	1.04 * 10-3	0.79	2	6.4
22	AGAP6	1.04 * 10-3	0.79	2	4.9
23	SPDYE2L	1.04 * 10-3	0.79	2	7.9
24	OR5J2	1.04 * 10-3	0.79	3	0.8
25	FGGY	1.04 * 10-3	0.79	2	3.2
26	TMEFF1	1.04 * 10-3	0.79	2	5.4
27	ATP5D	1.04 * 10-3	0.79	2	0.9
28	DEFA1B	1.04 * 10-3	0.79	2	3.1
* 29	USP28	1.04 * 10-3	0.79	2	52.0 ± 5.0
30	UBASH3B	1.08 * 10-3	0.79	1	15.7
31	GPALPP1	1.21 * 10-3	0.81	1	11.0
32	KIAA1704	1.36 * 10-3	0.81	1	11.0
33	ASB13	1.48 * 10-3	0.81	2	1.9
34	KRTAP5-10	1.50 * 10-3	0.81	3	3.6
35	USP17L1P	1.58 * 10-3	0.81	3	4.4
36	VWA1	1.62 * 10-3	0.81	2	9.3
37	CDKN1C	1.70 * 10-3	0.81	3	4.9
38	STK3	1.74 * 10-3	0.81	1	9.5
39	CCDC148	1.87 * 10-3	0.81	1	4.4
40	HBM	1.87 * 10-3	0.81	3	3.4
Cell cycle regulators					
* 146	CDKN1A (p21)	0.0100	0.81	1	22.9 ± 5.3
* 15787	CDKN2A	0.969	0.97	0	7.9 ± 1.9
DNA damage response					
* 508	ATM	0.0244	0.86	2	4.7 ± 1.4
* 10878	RNF8	0.969	0.97	0	4.4 ± 1.3
* 8523	RNF168	0.969	0.97	0	1.6 ± 0.61
* 12233	CHEK1 (Chk1)	0.969	0.97	0	4.5 ± 2.5
* 16442	CHEK2 (Chk2)	0.969	0.97	0	3.9 ± 0.59
Hippo pathway					
* 18386	LATS2	0.9687	0.97	0	3.3 ± 1.7
* 18739	LATS1	0.969	0.97	0	1.9 ± 0.10
Control					
	Plk4AS				6.9 ± 2.8

Figure 15. Inhibition of Plk4 kinase activity activates the centrosome surveillance pathway and prevents cell growth.

(A) Graph showing the relative levels of Plk4 at the centrosomes of interphase cells at various times after addition of 3MB-PP1. Data are means ± SEM ($N = 2$, >20 cells per experiment).

(B) Flow cytometry cell cycle analysis of Plk4^{AS} cells after 4 days in DMSO or 3MB-PP1.

(C) Representative images of crystal violet stained colonies.

(D) Graph showing the relative clonogenic survival of 3MB-PP1 treated Plk4^{AS} cells grown in either 21% or 3% O_2. Data are means ± SEM (N = 2, performed in duplicate).

(E) Table of rank-ordered candidate hits from the CRISPR/Cas9 screen in Plk4^{AS} cells. Genes were ordered using the MaGeCK algorithm (Li et al., 2014). The top-most enriched sgRNA was used to validate each gene and the % clonogenic survival of 3MB-PP1 treated Plk4^{AS} cells expressing each individual sgRNA is shown. In most cases, % clonogenic growth values represent the mean of a single sgRNA performed in duplicate. For genes marked with an *, % clonogenic growth values represent the mean of at least two independent sgRNAs performed in duplicate.

(F) Graph showing the relative clonogenic survival of 3MB-PP1 treated Plk4^{AS}; p53$^{-/-}$, Plk4^{AS}; 53BP1$^{-/-}$, Plk4^{AS}; p21$^{-/-}$, Plk4^{AS}; USP28$^{-/-}$ cells. Data are means ± SEM (N = 3, performed in duplicate).

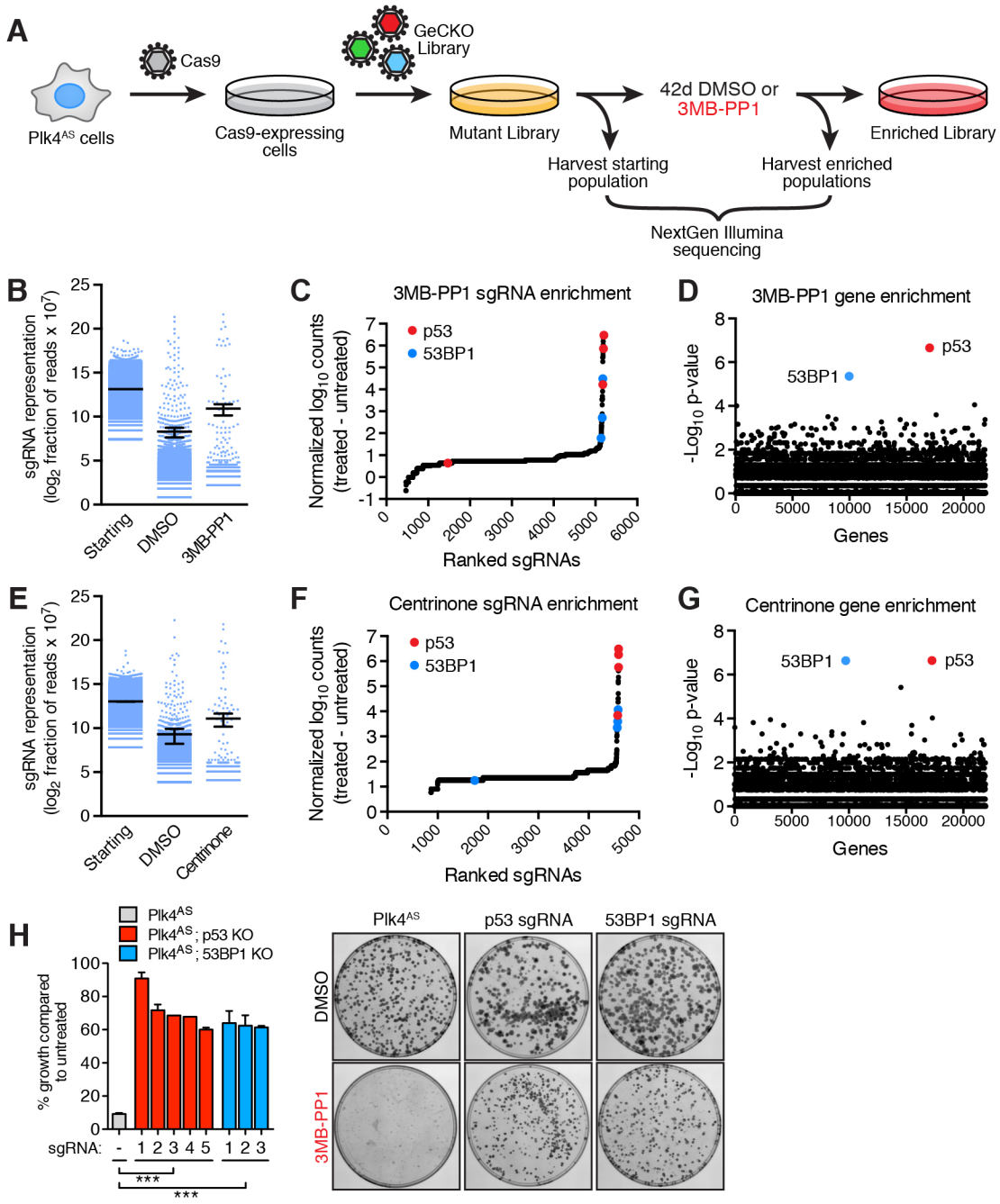

Figure 16. A genome-wide CRISPR/Cas9 screen identifies 53BP1 and p53 as components of the centrosome surveillance pathway.

(A) Schematic of the pooled, positive section CRISPR/Cas9 screen used to identify components of the centrosome surveillance pathway.

(B) Graph showing the distribution of individual sgRNAs. Data are means ± SD.

(C) Rank-ordered dot plot showing relative enrichment of individual sgRNAs following 3MB-PP1 treatment.

(D) Identification of top candidate genes after 3MB-PP1 treatment using the MaGeCK ranking *p*-value analysis.

(E) Graph showing the distribution of individual sgRNAs. Data are means ± SD.

(F) Rank-ordered dot plot showing relative enrichment of individual sgRNAs following centrinone treatment.

(G) Identification of top candidate genes after centrinone treatment using the MaGeCK ranking *p*-value analysis.

(H) Graph showing the relative clonogenic growth of 3MB-PP1 treated $Plk4^{AS}$ cells expressing individual sgRNAs. Data are means ± SEM ($N = 2$, performed in duplicate). Representative images of crystal violet stained colonies.

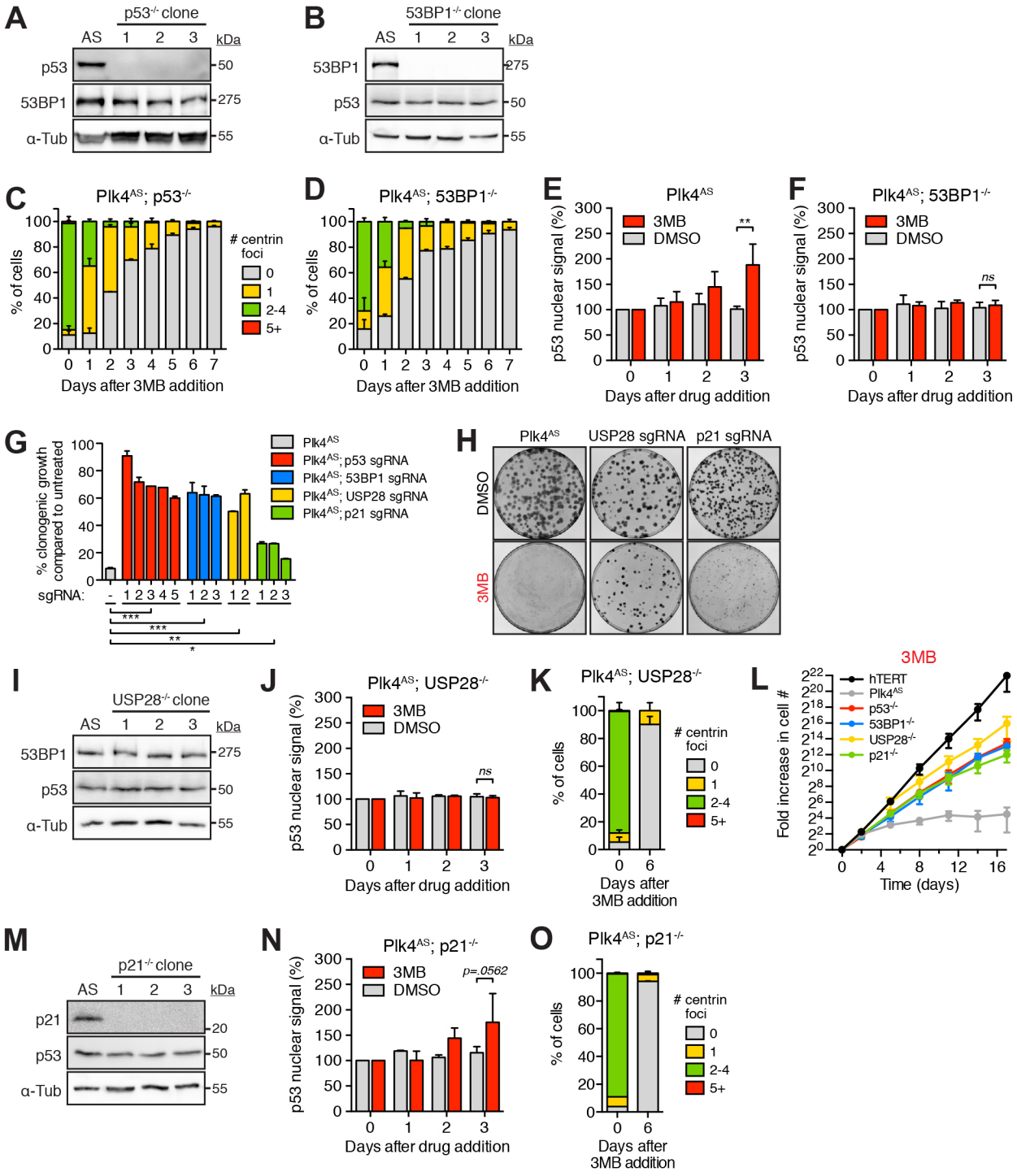

Figure 17. p21 and USP28 are required for the centrosome surveillance pathway.

(A-B) Immunoblot showing the level of p53 or 53BP1 in Plk4^{AS}; p53$^{-/-}$ and Plk4^{AS}; 53BP1$^{-/-}$ cells.

(C-D) Centriole number distribution in interphase Plk4^{AS}; p53$^{-/-}$ and Plk4^{AS}; 53BP1$^{-/-}$ cells at times after addition of 3MB-PP1. Data are means ± SEM (N = 3, >80 cells per experiment).

(E-F) Relative abundance of nuclear p53 in Plk4^{AS} and Plk4^{AS}; 53BP1$^{-/-}$ cells at times after addition of DMSO or 3MB-PP1. Data are means ± SEM (N = 3, >180 cells per experiment).

(G) Relative clonogenic survival of 3MB-PP1 treated Plk4^{AS} cells expressing individual sgRNAs. Data are means ± SEM (N = 2, performed in duplicate).

(H) Representative images of crystal violet stained colonies.

(I) Immunoblot showing the level of p53 or 53BP1 protein in Plk4^{AS}; USP28$^{-/-}$ cells.

(J) Relative abundance of nuclear p53 in Plk4^{AS}; USP28$^{-/-}$ cells at times after addition of DMSO or 3MB-PP1. Data are means ± SEM (N = 3, >180 cells per experiment).

(K) Centriole number distribution in interphase Plk4^{AS}; USP28$^{-/-}$ cells at 6 days after addition of 3MB-PP1. Data are means ± SEM (N = 3, >80 cells per experiment).

(L) Fold increase in cell number after 3MB-PP1 addition. Data are means ± SEM (N = 2, performed in triplicate).

(M) Immunoblot showing the level of p21 or p53 in Plk4^{AS}; p21$^{-/-}$ cells.

(N) Relative abundance of nuclear p53 in Plk4^{AS}; p21$^{-/-}$ cells at times after addition of DMSO or 3MB-PP1. Data are means ± SEM (N = 3, >180 cells per experiment).

(O) Centriole number distribution in interphase Plk4^{AS}; p21$^{-/-}$ cells at 6 days after addition of 3MB-PP1. Data are means ± SEM (N = 3, >80 cells per experiment).

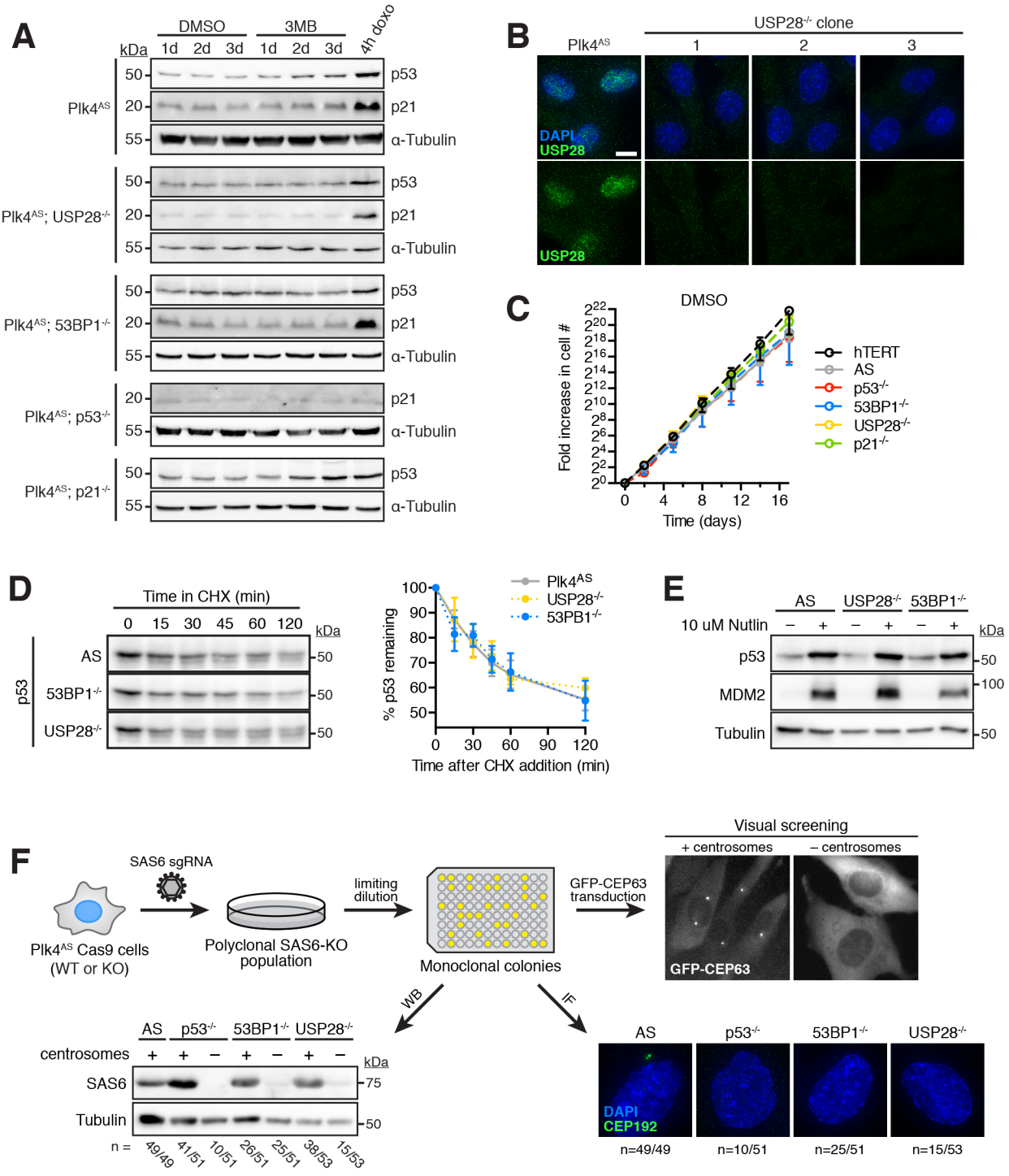

Figure 18. USP28$^{-/-}$ and 53BP1$^{-/-}$ cells activate p53 in response to DNA damage, but not following centrosome loss.

(A) Immunoblot showing the level of p21 and p53 at times after addition of DMSO or 3MB-PP1.

(B) Images showing loss of nuclear USP28 staining in Plk4^{AS}; USP28$^{-/-}$ cells. Scale bar = 5 μm.

(C) Graph showing the fold increase in cell number after DMSO addition. Data are means ± SEM (N = 2, performed in triplicate).

(D) Immunoblot showing the abundance of p53 in Plk4^{AS} cells at times after cycloheximide (CHX) addition. Graph show quantification of p53 levels at each time point. Data are means ± SEM (N = 3).

(E) Immunoblot showing the abundance of p53 and MDM2 in Plk4^{AS} cells at 16 hours after Nutlin-3 treatment.

(F) Plk4^{AS}; p53$^{-/-}$, Plk4^{AS}; 53BP1$^{-/-}$, and Plk4^{AS}; USP28$^{-/-}$ cells expressing SpCas9 were transduced with an sgRNA targeting SAS6. Monoclonal lines were isolated by limiting dilution. Each clone was transduced with a GFP-CEP63 expressing lentivirus and scored for the presence or absence of centrosomes. Individual clones were isolated and analyzed for SAS6 protein levels by immunoblot and fixed and stained with CEP192 antibodies to verify whether or not centrosome were present. As expected, cells lacking SAS6 always lacked centrosomes. Numbers represent the fraction of clones for each line that either did or did not contain centrosomes. All of the Plk4^{AS} clones recovered contained SAS6 and centrosomes (49/49). However, SAS6 knockout cells lacking centrosomes were identified in the p53 (10/51), 53BP1 (25/51), and USP28 (15/53) knockout background.

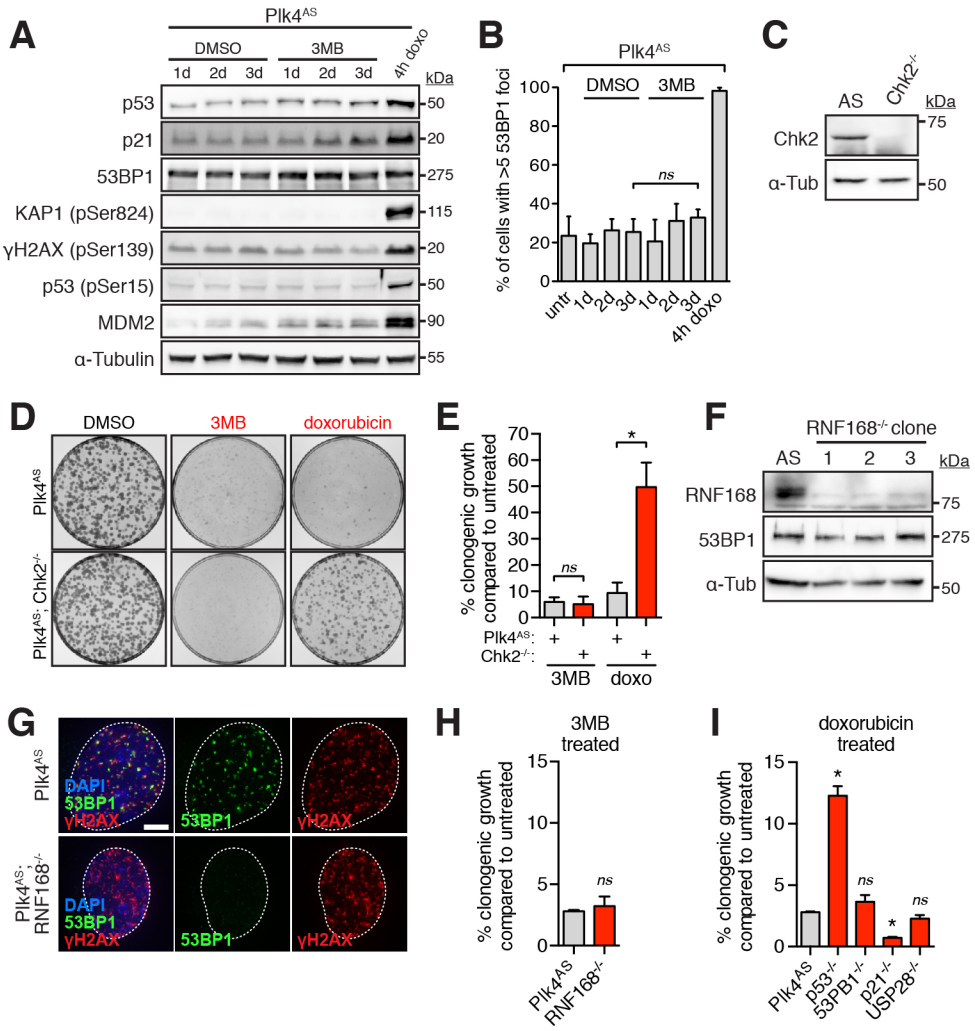

Figure 19. The DNA damage response and centrosome surveillance pathway are genetically separable.

(A) Immunoblot showing the level of various proteins at 1, 2 or 3 days after addition of DMSO or 3MB-PP1.

(B) Fraction of cells with >5 53BP1 foci at times after addition of DMSO or 3MB-PP1. Data are means ± SEM ($N = 3$, >50 cells per experiment).

(C) Immunoblot showing protein levels in Plk4^{AS}; Chk2$^{-/-}$ cells.

(D) Representative images of crystal violet stained colonies.

(E) Relative clonogenic survival of 3MB-PP1 or doxorubicin (10 ng/ml) treated Plk4^{AS} cells. Data are means ± SEM (N = 3).

(F) Immunoblot showing protein levels in Plk4^{AS}; RNF168$^{-/-}$ cells.

(G) Images show the loss of 53BP1 foci formation in doxorubicin-treated Plk4^{AS}; RNF168$^{-/-}$ cells. Scale bar = 5 μm.

(H) Graph shows the relative clonogenic survival of Plk4^{AS} and Plk4^{AS}; RNF168$^{-/-}$ cells treated with 3MB-PP1. Data are means ± SEM (N = 3).

(I) Graph showing the relative clonogenic survival of doxorubicin-treated (10 ng/ml) Plk4^{AS} cells. Data are means ± SEM (N = 3).

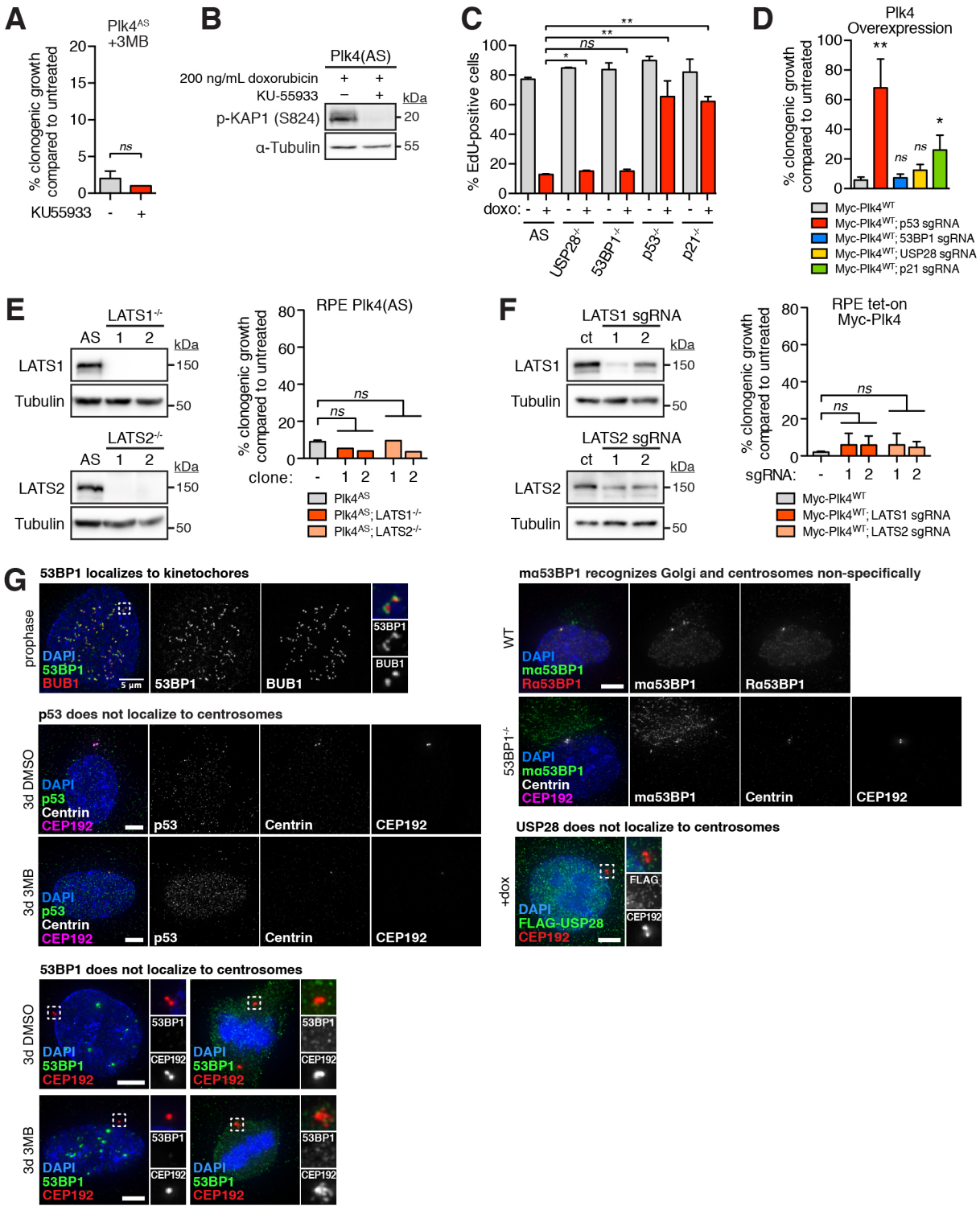

Figure 20. Knockout of 53BP1 or USP28 does not allow growth in cells overexpressing Plk4.

(A) Graph shows the relative clonogenic survival of 3MB-PP1 treated Plk4^{AS} cells grown in the presence or absence of the ATM inhibitor KU-55933. Data are means ± SEM (N = 2, performed in duplicate).

(B) Immunoblot showing the level of phosphorylation of the ATM substrate, KAP1 S824, in cells treated with doxorubicin in the presence or absence of KU-55933.

(C) Plk4^{AS} cells were treated with doxorubicin (10 ng/ml) for 24 hours and then labeled with EdU for a further 12 hours. Graph shows the fraction of EdU-positive cells. Data are means ± SEM (N = 2, >150 cells per experiment).

(D) Graph shows the relative clonogenic survival of Myc-Plk4^{WT} overexpressing cells. Data are means ± SEM (N = 2, performed in duplicate).

(E) Immunoblot showing protein levels in Plk4^{AS}; LATS1$^{-/-}$ and Plk4^{AS}; LATS2$^{-/-}$ cells. Graph shows the relative clonogenic survival of 3MB-PP1 treated Plk4^{AS}; LATS1$^{-/-}$ and Plk4^{AS}; LATS2$^{-/-}$ cells. Data represents two independent knockout clones for LATS1 and LATS2.

(F) Immunoblot showing protein levels in Myc-Plk4^{WT} cells expressing individual sgRNAs targeting LATS1 and LATS2. Graph shows the relative clonogenic growth of induced Myc-Plk4^{WT} cells. Data are means ± SEM (N = 2).

(G) Images showing the localization of p53, 53BP1 and USP28 in interphase and mitosis. Scale bar = 5 μm.

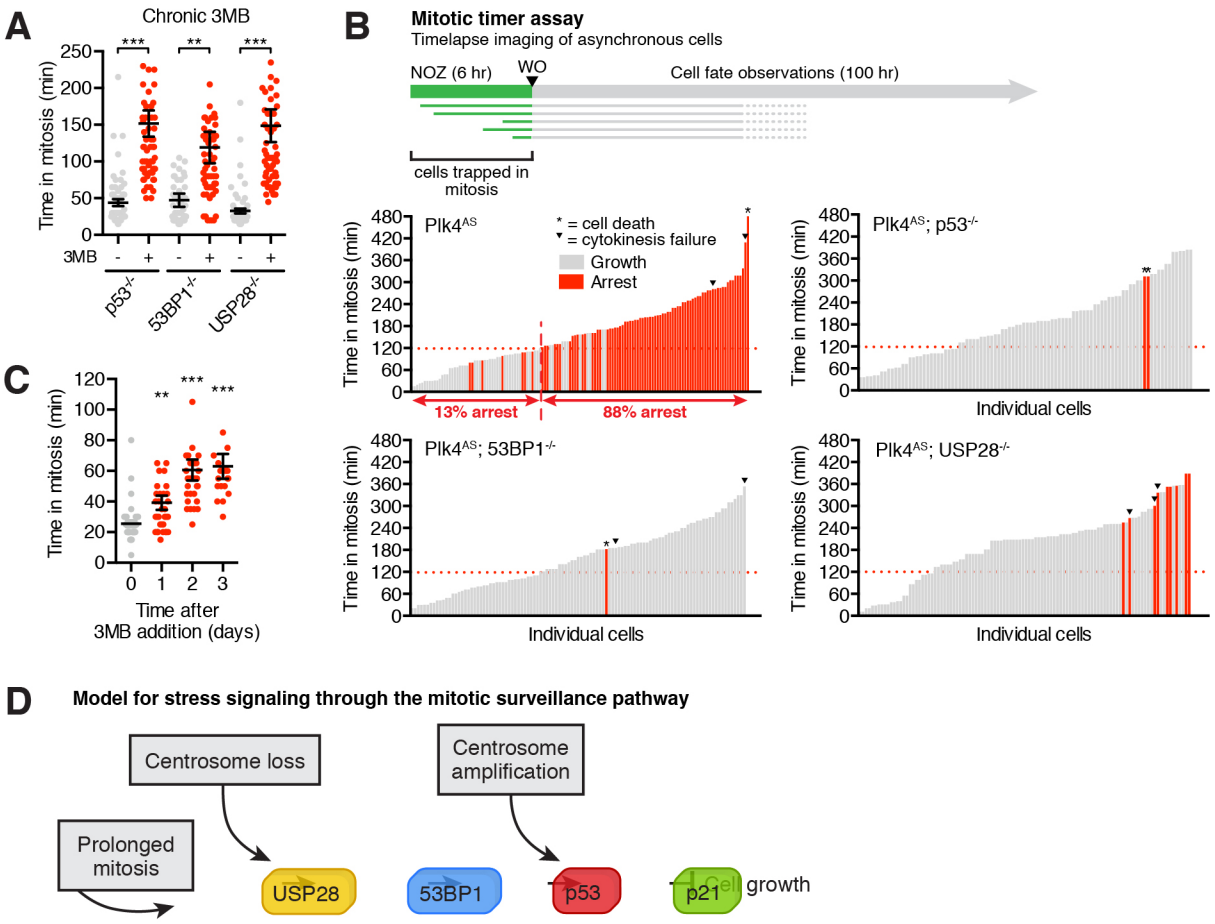

Figure 21. Prolonged prometaphase and centrosome loss signal through the same components to arrest the cell cycle.

(A) Mitotic duration in Histone H2B-EGFP expressing p53$^{-/-}$, 53BP1$^{-/-}$ and USP28$^{-/-}$ Plk4^{AS} cells, grown in either DMSO or 3MB-PP1 for six days. Data are means ± SEM (N = 2, >25 cells per experiment).

(B) Schematic of the mitotic timer experiment. Graph shows the prometaphase duration and proliferative capacity of 3MB-PP1-treated Plk4^{AS} cells. Each bar represents a daughter cell; its height represents the prometaphase duration of the mother cell, and its color represents the fate of the daughter. The dashed red line indicates the maximum time that mother cells spend in prometaphase before > 85% of daughter cells undergo a cell cycle arrest.

(C) Mitotic duration in Histone H2B-EGFP expressing Plk4^{AS} cells. Measurements were taken over a 24 hr period at indicated times after 3MB-PP1 addition. Data are means ± SEM (N = 2, >25 cells per experiment).

(D) A model for stress signaling inputs into the mitotic surveillance pathway.

Chapter 4

Centrosome loss is synthetic lethal with high TRIM37 expression in 17q23-amplified breast cancer cells

4.1 Introduction

Breast cancer is the most commonly diagnosed cancer in the US, with 268,670 new cases expected in 2018. Breast cancer is comprised of several distinct subtypes that lead to differences in response to various treatment modalities and clinical outcomes. Before the rise of high-throughput technologies, the prognosis of breast cancers relied heavily on physical characteristics, such as tumor size and histological grade, as well as expression patterns of estrogen, progesterone, and HER2 receptors (Tang et al., 2008). We are now in the emerging age of genomics, where tumors can be more precisely characterized by defining the specific genetic alterations that drive disease progression (Kittaneh et al., 2013; Massard et al., 2017). These methods have aided efforts to better understand the relationship between cancer genotype and therapeutic responsiveness. One notable success story in this field is the identification of an Achilles' heel in tumors containing BRCA1/2 null mutations. Treatment of BRCA1/2 null tumors with PARP inhibitors results in a potent synthetic lethal effect. However, as only 5-10%

of breast tumors are caused by inherited mutations in BRCA1/2, there is a need to identify additional molecular vulnerabilities that can be exploited therapeutically.

The recognition of this need has driven major efforts to define breast cancer subgroups and their molecular drivers. One such sweeping study analyzed >2000 breast cancer samples, integrating multiple levels of genomic and transcriptomic information such as copy number and gene expression to classify them into 10 subgroups (Curtis et al., 2012). One subgroup of interest is defined by an amplification of the 17q23 chromosomal locus, which was associated with high levels of genome instability and poor prognosis. The prevalence of this amplification has been reported to range from 18-20% (Kallioniemi et al., 1994; Monni et al., 2001). The amplicon can be up to 4 MB in size, and may contain up to 50 genes. Expression profiling of the amplicon identified several genes that were consistently overexpressed in tumors containing the amplicon, of which *RPS6KB1*, *TBX2*, and *PPM1D* genes appear to be likely oncogenic drivers (Monni et al., 2001; Sinclair et al., 2003). The *TRIM37* gene is also highly expressed from this region, and encodes a 108 kDa E3 ubiquitin ligase. Recent studies have implicated TRIM37 in controlling the microtubule nucleating capacity of cells, though its relevant targets remain unclear (Meitinger et al., 2016a).

Centrosomes are the major microtubule-organizing centers of the cell, and help to catalyze the formation of the bipolar mitotic spindle. While centrosomes increase the efficiency of spindle assembly, centrosome-independent pathways exist to facilitate spindle formation (Heald et al., 1997; Khodjakov et al., 2000; Prosser and Pelletier, 2017). Microtubule nucleation can also occur through chromosome- and microtubule-mediated pathways, which are able to spawn

sufficient microtubules for spindle assembly when centrosomes are absent. These three pathways for microtubule nucleation are at least partially redundant, though deficiencies in any one pathway results in mitotic delays which could result in genome instability.

While non-transformed cells are able to undergo successful mitoses in the absence of centrosomes, dividing under these conditions triggers a cell cycle arrest (Lambrus et al., 2015; Wong et al., 2015b). This is due to the activation of a mitotic surveillance pathway that signals through a 53BP1-USP28-p53-p21 axis, which triggers a G1 arrest following prolonged mitoses (Fong et al., 2016a; Lambrus et al., 2016; Meitinger et al., 2016a). Cells that do not have an intact mitotic surveillance pathway, however, are able to proliferate robustly in the absence of centrosomes. As the majority of cancers have disrupted p53 or p21 pathways and grow well in the absence of centrosomes, centrosome depletion is not a generally effective therapeutic strategy against cancers (Wong et al., 2015b). In this chapter, we describe our surprising discovery of a novel synthetic lethal relationship in which centrosome loss induced with PLK4 inhibition promotes cell death in breast cancers with high levels of the TRIM37 oncoprotein.

4.2 MCF-7 breast cancer cells are hypersensitive to centrinone, independent of the mitotic surveillance pathway

While evaluating the response of various cell lines to centrosome loss, we discovered that MCF-7 breast cancer cells exhibited a striking growth arrest when treated with the PLK4 inhibitor centrinone (**Fig. 22A-B**). To test whether this growth arrest was dependent on the mitotic surveillance pathway, we generated knockouts for the core components of this pathway (*TP53BP1*, *USP28*, and *TP53)* in MCF-7 cells (**Fig. 23A-B**). In contrast to RPE-1 cells, which

readily proliferate in centrinone when the mitotic surveillance pathway is disrupted (Fong et al., 2016b; Lambrus et al., 2016; Meitinger et al., 2016b), the growth of MCF-7 cells was not enhanced by loss of mitotic surveillance components (**Fig. 22A-B, Fig. 23A**).

4.3 The sensitivity of MCF-7 cells to centrinone is dependent on overexpression of the TRIM37 oncoprotein

The hypersensitivity of MCF-7 cells to PLK4 inhibition stands in contrast to the majority of tumor cancer cell lines, which proliferate robustly in the absence of centrosomes (Moyer et al., 2015; Wong et al., 2015c). This led us to consider whether MCF-7s may be sensitized to centrosome loss by their genetic background. MCF-7s notably possess an amplification of chromosomal locus 17q23, an amplicon found in ~20% of breast cancers (Kallioniemi et al., 1994; Kuukasjarvi et al., 1997). In MCF-7s, this region spans 4 MB and contains ~40 protein-encoding genes (Monni et al., 2001; Parssinen et al., 2007; Sinclair et al., 2003). Among these is *TRIM37*, a gene encoding a 108 kDa E3 ubiquitin ligase previously implicated in centrosome function (Balestra et al., 2013; Meitinger et al., 2016b), although its centrosomal substrates are not known. Knockdown of TRIM37 leads to PCM accumulation, enabling more robust and rapid spindle assembly in cells that lack centrosomes (Fong et al., 2016b; Meitinger et al., 2016b). We therefore reasoned that conversely, high levels of TRIM37 may reduce PCM levels and suppress spindle assembly efficiency, thereby increasing sensitivity to centrosome loss. To test this synthetic lethal relationship, we generated an MCF-7 cell line stably expressing a TRIM37 shRNA, which reduced TRIM37 levels by 90% (**Fig. 22C**). TRIM37 knockdown in MCF-7 cells resulted in a nearly four-fold improvement (increased from 25% to 88% in $p53^{-/-}$ background) in growth in centrinone compared to cells expressing a scrambled shRNA (**Fig. 22E-F**). This effect

was further supported by a marked rescue of cell viability by TRIM37 knockdown in centrinone-treated MCF-7 cells (**Fig. 22E**). We conclude that elevated expression of TRIM37 renders MCF-7 cells hypersensitive to centrinone treatment.

4.4 TRIM37 overexpression is synthetic lethal with PLK4 inhibition in HCT116 and RPE-1 cells

To test whether increased expression of TRIM37 is sufficient to cause synthetic lethality with PLK4 inhibition, we generated HCT116 $p53^{-/-}$ cells with constitutive overexpression of TRIM37 or eGFP. While either centrinone treatment or TRIM37 overexpression alone only slightly impaired the growth of HCT116 $p53^{-/-}$ cells, combined treatment resulted in dramatic growth inhibition (**Fig. 22G, Fig. 23C-D**). This demonstrates that TRIM37 overexpression is sufficient to drive synthetic lethality in cells that normally tolerate centrosome loss.

To confirm the lethal effect of centrinone in cells with high levels of TRIM37 was due to inhibition of PLK4 and not an off-target effect on another kinase, we generated doxycycline-inducible $p53^{-/-}$ RPE-1 cells carrying an endogenously expressed analogue-sensitive (AS) allele of PLK4 ($PLK4^{AS}$) (Lambrus et al., 2016). While inhibition of $PLK4^{AS}$ with the bulky ATP analogue 3MB-PP1, or overexpression of TRIM37, had a minor impact on cell proliferation, inhibition of PLK4 in combination with TRIM37 overexpression led to a dramatic suppression of cell growth (12 colonies, vs. 115 in 3MB alone and 97 with TRIM37 overexpression alone) (**Fig. 22H, Fig. 23E-F**). This shows that inhibition of PLK4 is synthetic lethal with TRIM37 overexpression.

4.5 PLK4 inhibition is synthetic lethal in 17q23 amplified breast cancer cells

To test whether the synthetic lethal effect is present in other breast cancer lines containing the 17q23 amplicon, we assayed BT474 and MDA-MB-361 cells, which express TRIM37 at levels similar to that observed in MCF-7 cells (**Fig. 24A**). In accord with the response observed in MCF-7 cells, BT474 and MDA-MB-361 cells exhibited a strong growth defect in centrinone that was rescued by TRIM37 knockdown (**Fig. 22I-J, Fig. 24B**). Furthermore, an analysis of relative growth of these three 17q23-amplified breast cancer lines shows severe growth inhibition in centrinone, compared to the same treatment in p53-deficient RPE-1s and DLD-1 and U2OS cells that do not carry the 17q23 amplicon (**Fig. 24C**). Together, these results show that tumor cells carrying the 17q23 amplicon express high levels of TRIM37 and consequently exhibit a strong sensitivity to centrosome loss induced by PLK4 inhibition.

4.6 MCF-7s undergo prolonged and aberrant mitosis upon centrinone treatment

To determine how PLK4 inhibition leads to a growth arrest in MCF-7 cells, we monitored MCF-7 $p53^{-/-}$ cells expressing H2B-iRFP and EGFP-tubulin by timelapse microscopy. We chose to use the p53-/- background to study mitotic defects without influence from the mitotic surveillance pathway. MCF-7 cells were first treated with centrinone or DMSO for 3 days, then filmed for 24 hours (**Fig. 25A**). While DMSO-treated MCF-7 cells progressed through mitosis normally, 47.4% of the centrinone-treated cells failed to form a bipolar spindle and either remained arrested in mitosis for the duration of the movie or slipped out of mitosis without undergoing anaphase (**Fig. 25B-C**). Importantly, knockdown of TRIM37 restored bipolar spindle formation in centrinone-treated MCF-7 cells, resulting in a dramatic decrease in mitotic duration (from an

average of 6.2 to 2.2 hrs) and cell division errors (from 47.4% to 9.9%) (**Fig. 25C-E**). These data suggest that high levels of TRIM37 antagonize spindle assembly in MCF-7 cells lacking centrosomes.

4.7 Identifying TRIM37 proximity partners using proximity-dependent biotinylation

To understand the mechanism by which high TRIM37 levels drive synthetic lethality with centrosome loss, we sought to identify TRIM37 interactors using proximity-dependent biotin labeling, a method which exploits a mutated, promiscuous form of *Escherichia coli* biotin ligase (BirA*) to biotinylate proteins within a ~10 nm radius (Roux et al., 2012). We generated a doxycycline-inducible lentiviral construct containing TRIM37 tagged with mTurbo, an optimized version of BirA* with enhanced efficiency (Branon et al., 2018). Biotin-labeling experiments were performed in RPE-1 cells, where mTurbo-TRIM37 was expressed ~2-4-fold above endogenous levels (**Fig. 26A**). To identify TRIM37 proximity partners, expression of mTurbo-TRIM37 or mTurbo alone was induced for 24 hrs before biotin was supplied for labeling for 6 hrs. To compare between mitotic and interphase interacting partners, we enriched for mitotic cells by adding dimethylenastron (an Eg5 inhibitor) 2 hrs after biotin addition. Mitotic and interphase biotinylated samples were harvested separately, captured with streptavidin-coated beads and bound proteins identified by mass spectrometry.

We thresholded for hits with > 2-fold higher peptide representation in mTurbo-TRIM37 samples compared to mTurbo alone. This identified 184 TRIM37 proximity interaction partners, 7 of which have been previously reported as TRIM37 interactors (**Fig. 27A**). The top 30 hits with the

most spectral counts are listed in **Fig. 26B**. Gene ontology analyses showed a statistical enrichment of centrosomal proteins within this data set (**Fig. 26C**), which was corroborated by a clear enrichment of biotinylated proteins at the centrosome in biotin-labeled cells expressing mTurbo-TRIM37 (**Fig. 26D**). One of the most enriched hits is CEP192, a well-established component of the pericentriolar material (PCM) of centrosomes. This is consistent with a previous study which showed that depletion of TRIM37 allows the accumulation of PCM foci containing CEP192 (Meitinger et al., 2016b).

4.8 Overexpression of TRIM37 reduces PCM levels and suppresses microtubule nucleation in MCF-7 cells

To directly test if TRIM37 regulates the abundance of PCM proteins, we first examined cell-wide levels of the PCM components CEP192, CEP152, Pericentrin, and CDK5RAP2 in cells with reduced or elevated TRIM37 expression. Knockdown of TRIM37 resulted in a modest increase in the levels of most PCM components in MCF-7 cells, while acute overexpression of TRIM37 in RPE-1 cells dramatically suppressed the levels of the same proteins (**Fig. 27A**). To determine the impact of elevated TRIM37 levels in mitosis, we measured the abundance of PCM at mitotic centrosomes in MCF-7 cells. Depletion of TRIM37 led to an increase in centrosomal CEP192, Pericentrin, and CDK5RAP2 to a level comparable to that observed in RPE-1 cells (**Fig. 27B-C**). To determine whether this increase in PCM abundance has an effect on microtubule nucleation, we performed microtubule regrowth assays on control and TRIM37-depleted MCF-7 cells. We found that, consistent with the observed increase in PCM levels, mitotic centrosomes in TRIM37-depleted cells nucleated nearly twice the amount of alpha-tubulin compared to control cells (**Fig. 28A-B**). The levels of EB1, a plus-end tracking marker of

growing microtubules, were also increased more than 3-fold on centrosomes in TRIM37-depleted cells. We conclude that TRIM37-dependent suppression of PCM levels in MCF-7 cells leads to reduced microtubule nucleation from the centrosome.

4.9 Non-centrosomal PCM aids in mitotic spindle assembly when centrosomes are depleted

We next sought to analyze whether PCM suppression results in decreased microtubule nucleation in the absence of centrosomes, which we hypothesize to underlie the synthetic lethality of high TRIM37 levels with centrinone treatment. MCF-7 control and TRIM37-knockdown cells were treated with centrinone for 5 days to remove centrosomes, then examined by immunofluorescence for the presence of acentrosomal PCM aggregates that aid in spindle assembly. We found that in cells lacking centrosomes, 30-40% of TRIM37-depleted MCF-7s exhibited non-centrosomal PCM aggregates interacting with spindle microtubules, while this was almost never observed in control MCF-7 cells (**Fig. 27D-E**). These observations are consistent with a model in which high TRIM37 expression suppresses cellular PCM levels that are required to coordinate mitotic spindle assembly in the absence of centrosomes.

To further test the proposal that reduced microtubule nucleation by the PCM is synthetic lethal with centrosome loss, we depleted the core PCM protein CEP192 with two independent shRNAs in RPE-1 $p53^{-/-}$ $PLK4^{AS}$ cells. CEP192 levels were reduced to a similar level to that observed in wild type MCF-7 cells (**Fig. 29A-C, Fig. 27C**). As predicted, depletion of CEP192 increased the sensitivity of RPE-1 $p53^{-/-}$ cells to centrosome loss (58% growth in centrinone-treated control RPE-1 cells, compared to 24% and 28% in two-independent CEP192-shRNA clones) (**Fig. 27F**).

Furthermore, timelapse analysis showed that RPE-1 shCEP192 cells lacking centrosomes exhibited delayed mitotic centrosome maturation and an inability to form a bipolar spindle (**Fig. 27G-H**). These phenotypes that were strikingly similar to those observed in MCF-7 cells depleted of centrosomes (**Fig. 25**). We conclude that reducing cellular PCM levels increases sensitivity to centrosome loss.

4.10 TRIM37 levels are cell cycle regulated

Given that centrosomal PCM expands dramatically prior to mitotic entry (Woodruff et al., 2014), we considered the possibility that TRIM37 abundance may be regulated in a cell cycle dependent manner to allow mitotic PCM accumulation. We used synchronized RPE-1 cells to assess TRIM37 levels at different stages of the cell cycle and found that TRIM37 levels peak in early S phase and reduce significantly by late-S/G2 (**Fig. 30A-E**). TRIM37 levels continue to decline and reach the lowest levels in mitosis, which corresponds with the time of PCM expansion. To test if low-levels of TRIM37 are required for the sharp increase in centrosome-driven microtubule nucleation in late G2, we examined the effect of TRIM37 expression levels on the timing of centrosome-mediated microtubule nucleation in late G2 phase. Overexpression of TRIM37 in RPE-1 cells delayed the time of centrosome activation from 30 ±5 mins to 13 ±5 min prior to nuclear envelope breakdown (NEBD). Moreover, the timing of centrosome activation in MCF-7 cells occurred 20 ±10 mins earlier in cells depleted of TRIM37 compared with control cells (**Fig. 31A-D**). These data suggest that high levels of TRIM37 at G2/M phase delay the onset of microtubule nucleation by the centrosome.

4.11 TRIM37 overexpression drives genomic instability

We noticed that overexpression of TRIM37 in RPE-1 cells led to striking increase in the DNA damage marker γH2A.X and stabilization of p53 and p21 (**Fig. 32A**). Consequently, TRIM37 overexpression caused a cell cycle arrest that was overcome by p53 loss. This suggests that rather than being a passive passenger in the 17q23 amplicon, increased TRIM37 copy number may confer oncogenic properties that contribute to genome instability and tumor evolution. Supporting this hypothesis, cytogenetic analyses of RPE-1 cells show that acute overexpression TRIM37 increases the incidence of abnormally separated sister chromatids from ~15% to ~60% (**Fig. 32B**). To assess whether mitotic errors caused by TRIM37 overexpression could be propagated and promote genome instability, we analyzed the short-term effect of TRIM37 overexpression on chromosome segregation errors in $p53^{-/-}$ RPE-1 cells using time-lapse microcopy. Although all of the $p53^{-/-}$ RPE-1 control cells analyzed (n=91) underwent successful divisions, we observed a dramatic increase in the incidence of mitotic slippage in cells overexpressing TRIM37 (**Fig. 32C**). 70% of the cells that failed mitosis progressed through the cell cycle and divided a second time (**Fig. 32C**), suggesting that TRIM37 overexpression drives whole-genome duplication events that can be propagated in subsequent divisions.

To more directly test whether elevated levels of TRIM37 contribute to the genetic instability observed in MCF-7 cells, we examined the effect of TRIM37 knockdown on the fidelity of cell division in $p53^{-/-}$ MCF-7 cells. Knockdown of TRIM37 reduced the rate of mitotic errors from 7.5% (n=84 cells) down to 0% (n=110 cells) (**Fig. 25C**), indicating that reduced TRIM37 levels increase mitotic fidelity in MCF-7 cells. This suggests that high TRIM37 levels promote mitotic errors that result in whole-genome duplication, a phenomenon that often occurs early in tumor

evolution and serves as a precursor for subsequent subclonal diversification (Bielski et al., 2018; Ganem et al., 2007).

4.13 Discussion

While most cancer cell lines are able to proliferate robustly in the absence of centrosomes (Wong et al., 2015b) here, we show that breast cancer cells with amplification of the chromosomal region 17q23 are an exception. These cells undergo dramatic growth arrest following centrosome loss, an effect is dependent upon the high levels of TRIM37 in the 17q23 amplicon. How does TRIM37 overexpression result in vulnerability to centrosome loss? We propose a model in which high levels of TRIM37 suppress CEP192 below a critical threshold, preventing its ability to facilitate microtubule nucleation and bipolar spindle assembly in the absence of centrosomes (**Fig. 32D**). This model is consistent with the identification of CEP192 as a strong proximity-interactor with TRIM37, and the recapitulation of the synthetic lethal phenotype by CEP192-shRNA functional assays. Normally, cells depleted of centrosomes depend on non-centrosomal pathways to assemble a bipolar mitotic spindle. These include contributions of microtubule (MT) nucleation from existing MTs and the chromatin-generated RanGTP gradient (Prosser and Pelletier, 2017). Importantly, all three MT nucleation pathways share a requirement for γ-tubulin ring complexes (γTuRCs) to serve as MT nucleation sites (Luders et al., 2006), and γTuRCs themselves rely on a CEP192 scaffold for their activation (Gomez-Ferreria et al., 2007; Joukov et al., 2014; Kollman et al., 2011; Yang and Feldman, 2015). Our results suggest that in MCF-7s, high TRIM37 levels suppress CEP192 and thereby suppress the activation of γTuRCs, preventing the nucleation of non-centrosomal MTs. Supporting this hypothesis, siRNA-mediated CEP192 depletion was reported to result in “disorganized spindles” and delayed centrosome

maturation (Gomez-Ferreria et al., 2007), which are identical phenotypes to those seen following TRIM37 overexpression. Taken together, these results suggest that CEP192 is a major TRIM37 target underlying the synthetic lethal effect with centrosome loss in 17q23-amplified cancer cells. However, TRIM37 has many other putative interacting partners that may contribute to this phenotype, so a true test of this model depends on phenotypic rescue by CEP192 overexpression.

Cancers harboring the 17q23 amplicon are associated with higher genome instability and poor prognosis (Curtis et al., 2012; Hermsen et al., 1998; Isola et al., 1995). The results presented here show a synthetic lethal effect between centrosome loss and cancers containing the 17q23 amplicon, which suggest a new mechanism-based approach for treatment of this subset of tumors. The use of Plk4 inhibitors in clinical trials is already underway (Bedard et al., 2016), and have been well-tolerated and show favorable pharmacokinetic profiles, supporting the possibility of centrosome depletion as a therapeutic strategy. Future work exploring the responsiveness of cancer cell line and patient-derived xenografts to Plk4 inhibition will be an important next step in testing this therapeutic strategy.

4.14 Figures and Legends

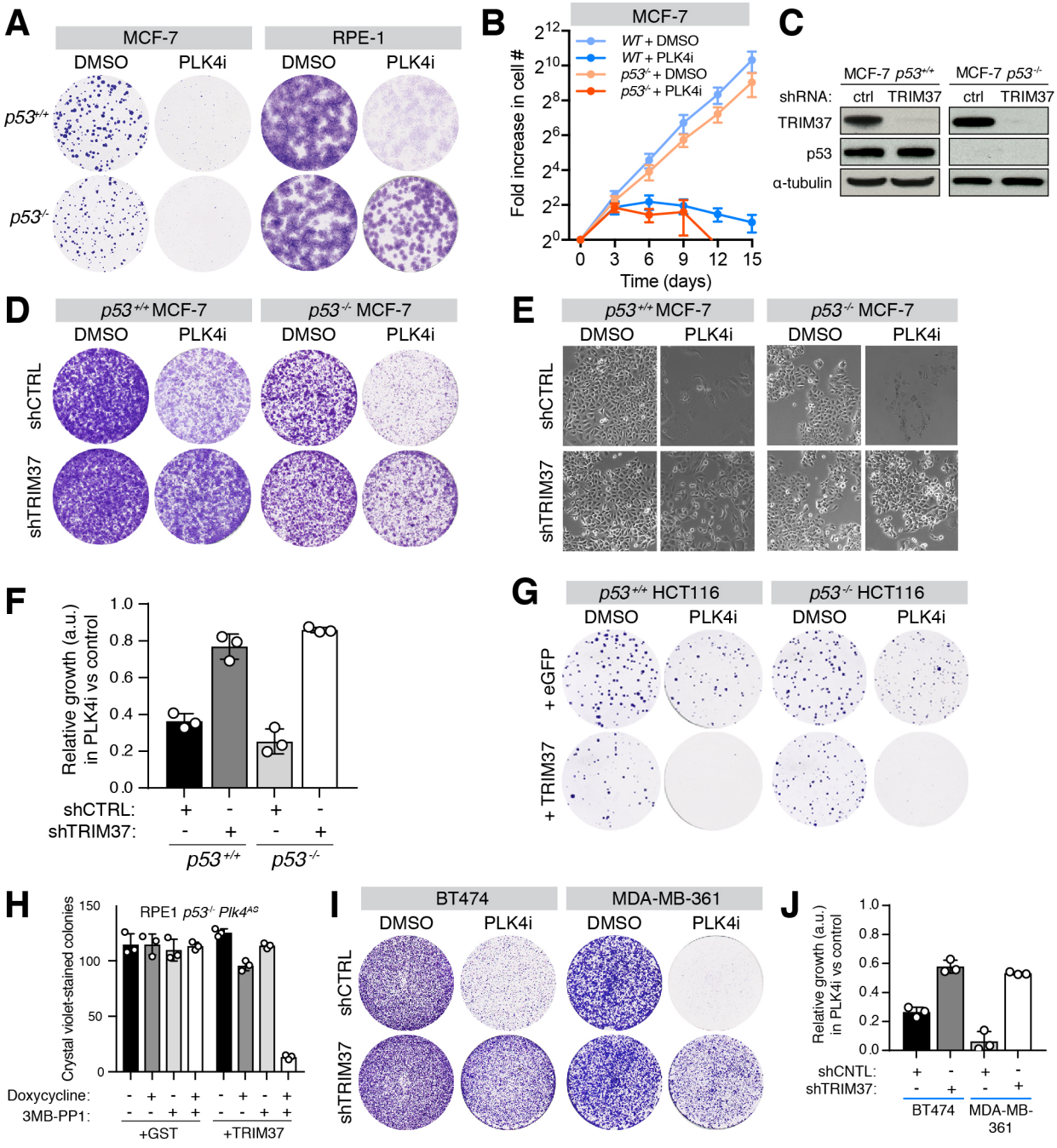

Figure 22. PLK4 inhibition is synthetic lethal with TRIM37 amplification in 17q23-amplified breast cancer cells.

(A) Long-term clonogenic survival assay of MCF-7 and RPE1 cells with indicated genotypes treated with DMSO (control) or Plk4 inhibitor centrinone (125 nM). After 14 days, colonies were fixed and stained with crystal violet.

(B) Graph showing the fold increase in cell number after centrinone addition. Centriole loss leads to an irreversible cell-cycle arrest. Points show the mean of three independent experiments.

(C) Western blot analysis of TRIM37 protein levels in $p53^{+/+}$ *and* $p53^{-/-}$ MCF-7 cells transduced with *TRIM37*-targeting shRNAs or vector control. Tubulin served as loading control. Representative data; n = 3 independent experiments.

(D) MCF-7 cells characterised in (C) were treated with DMSO (control) or Plk4 inhibitor centrinone for 10 days, fixed, and stained with crystal violet.

(E) Representative images of fields of centrinone or DMSO-treated MCF-7 cells in (D).

(F) Quantification of data in (D)**.** Data normalized to DMSO control for each group. n = 3 independent experiments. Mean ± s.d.

(G) Long-term clonogenic survival assay of centrinone-treated HCT116 cells of indicated genotypes transduced with lentivirus expressing eGFP (control) or TRIM37 protein. n = 3 independent experiments.

(H) Long-term colony survival assay of $p53^{-/-}$ $Plk4^{AS}$ hTERT-RPE1 cells expressing GST (control) or TRIM37 under a doxycycline-inducible system treated with DMSO (control) or ATP analogue 3MB-PP1. n = 3 independent experiments. Mean ± s.d. AS, analogue sensitive.

(I) 17q23-amplified cell lines BT474 and MDA-MB-361 transduced with *TRIM37*-targeting shRNAs or vector control were similarly treated as in (D).

(J) Quantification of data in (I). n = 3 independent experiments. Mean ± s.d.

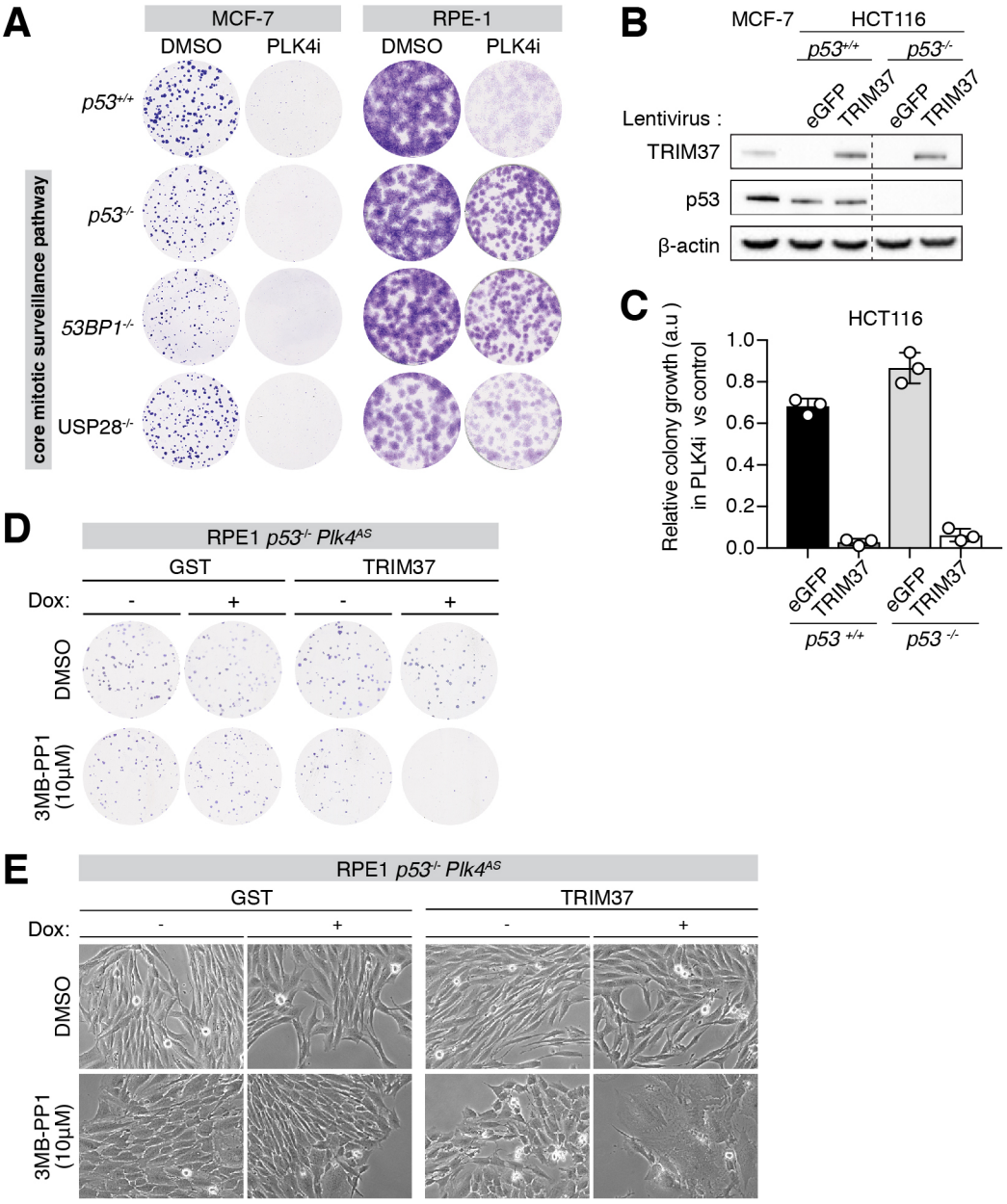

Figure 23. TRIM37 overexpression in HCT116s and RPE-1s recapitulates synthetic lethality with centrosome loss.

(A) Long-term clonogenic survival assay of MCF-7 and RPE1 cells with indicated genotypes treated with DMSO (control) or PLK4 inhibitor centrinone.

(B) Western blot characterization of HCT116 $p53^{+/+}$ and $p53^{-/-}$ cells transduced with lentiviral constructs to allow for constitutive eGFP or TRIM37 overexpression. β-Actin was used as a loading control.

(C) Quantification of data in Fig. 1g. Data normalized to DMSO control for each group. n = 3 independent experiments. Mean ± s.d.

(E) Long-term colony survival assay of $p53^{-/-}$ $Plk4^{AS}$ hTERT-RPE1 cells expressing GST (control) or TRIM37 under a doxycycline-inducible system treated with DMSO (control) or ATP analogue 3MB-PP1. AS, analogue sensitive.

(F) Representative images of fields of $p53^{-/-}$ $Plk4^{AS}$ hTERT-RPE1 cells treated as in (E).

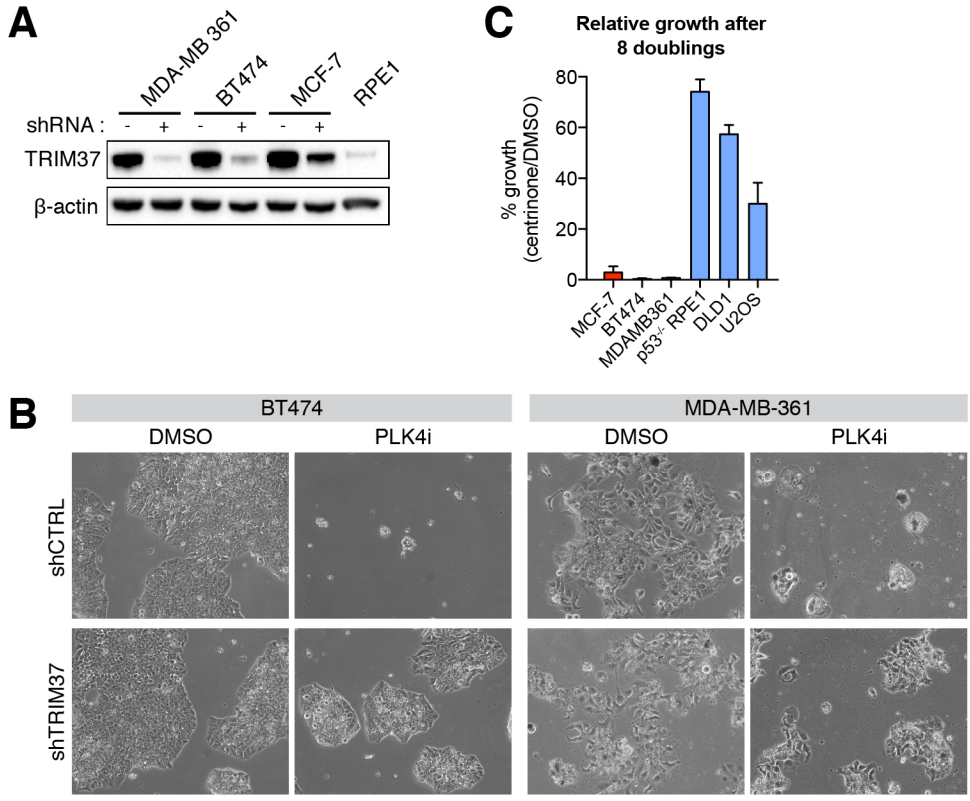

Figure 24. Additional characterization of TRIM37 expression and synthetic lethality in 17q23 cell lines.

(A) WB of a panel of 17q23 amplified (MDA-MB 361, BT474, MCF-7) and non-amplified (RPE1) cell lines expressing control (CNTL) or TRIM37 shRNA. β-Actin was used as a loading control.

(B) Growth assay counted at day 8, performed over three independent replicates.

(C) Representative images of fields of DMSO or PLK4i treated MDA-MB 361 and BT474 cells expressing control or TRIM37 shRNA.

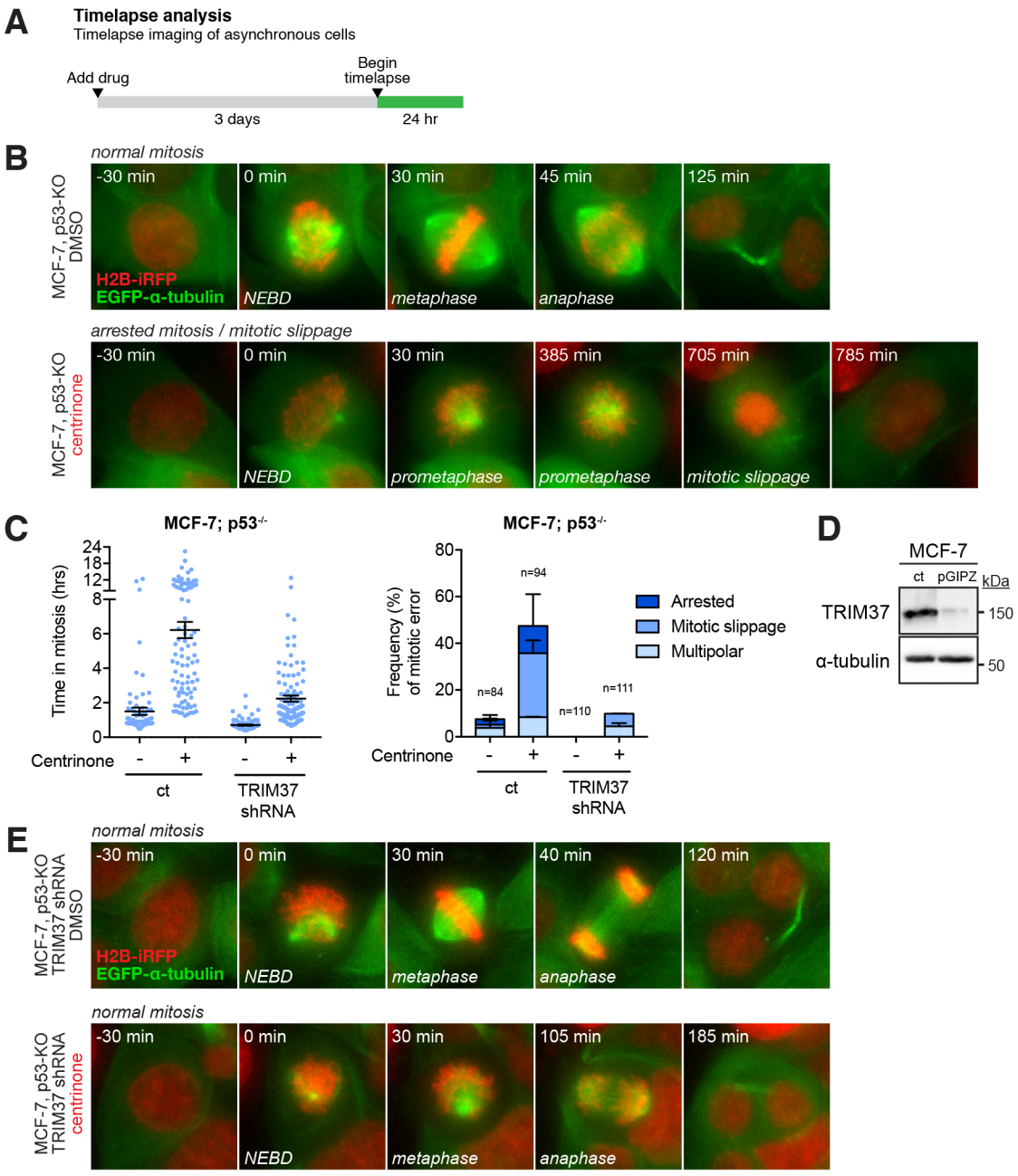

Figure 25. PLK4 inhibition triggers mitotic catastrophe in TRIM37 amplified cancer.

(A) Experimental schematic.

(B) Representative timelapse images of mitotic progression in DMSO- and centrinone-treated MCF-7s labeled with H2B-iRFP and EGFP-tubulin.

(C) Quantification mitotic duration and mitotic phenotype in ctrl MCF-7s compared to those expressing TRIM37-shRNA. Data acquired over of two independent timelapses, number of cells labeled above bars.

(D) Example of the efficiency of TRIM37 knockdown in MCF-7s expressing constitutive TRIM37-shRNA.

(E) Representative timelapse images of mitotic progression in DMSO- and centrinone-treated MCF-7s expressing TRIM37-shRNA, and labeled with H2B-iRFP and TagRFP-T-tubulin.

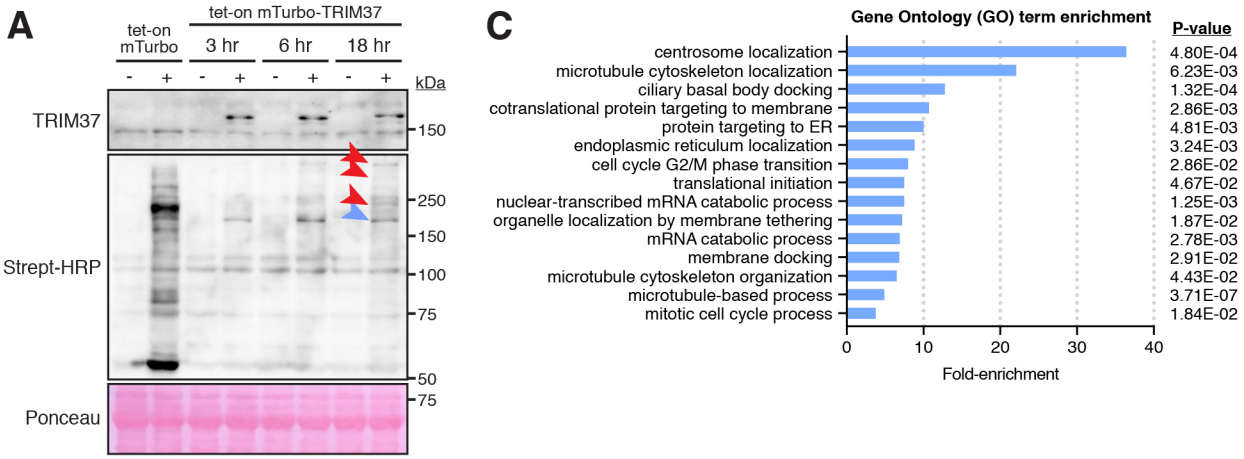

B

Filtered Rank	Gene Symbol	Size	Ctrl (int)	Ctrl (mit)	TRIM (int)	TRIM (mit)
1	**CEP170**	176 kDa	15	24	142	76
2	**TRIM37**	**108 kDa**	**0**	**0**	**115**	**66**
3	LRP1	505 kDa	7	0	52	21
4	TJP1	197 kDa	0	0	52	13
5	NCOR2	268 kDa	0	1	41	5
6	**CEP350**	351 kDa	3	4	28	17
7	**MAP4**	247 kDa	0	0	31	19
8	XRN1	193 kDa	0	2	23	19
9	**CEP192**	279 kDa	0	0	29	5
10	JMJD1C	263 kDa	0	1	28	2
11	SIPA1L3	195 kDa	2	2	25	4
12	EDC3	56 kDa	2	4	5	10
13	TNRC6B	183 kDa	0	1	20	7
14	**ARHGAP29**	142 kDa	1	2	14	4
15	ZNF281	97 kDa	3	0	12	7
16	SF3B3	136 kDa	0	0	12	8
17	NCOR1	279 kDa	0	0	19	2
18	CNBP	19 kDa	3	1	7	7
19	SNW1	61 kDa	0	0	1	10
20	**CEP152**	196 kDa	0	0	13	3
21	**SPATA2**	58 kDa	1	4	3	9
22	LDLR	95 kDa	0	1	5	10
23	MT2A	6 kDa	0	3	3	12
24	HSPA8	71 kDa	2	2	6	6
25	PCCB	58 kDa	2	0	8	3
26	HRNR	282 kDa	0	1	1	7
27	FBN1	312 kDa	0	0	8	5
28	NOTCH2	265 kDa	0	0	3	8
29	ALB	69 kDa	0	0	0	13
30	**PCM1**	228 kDa	1	0	10	3

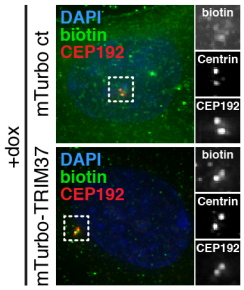

Figure 26. mTurbo identifies putative proximity interactors of TRIM37

(A) Western blot for TRIM37 and biotinylated proximity interactors. Ponceau stain was used to gauge relative loading.

(B) Thresholded mass spectrometry results, displaying the top 30 proximity interactors by spectral count and filtered for those with >2x more peptides in the mTurbo-TRIM37 sample compared to control.

(C) Gene ontology analysis of mass spectrometry data.

(D) Immunofluorescence of biotin-labeled mTurbo cell lines.

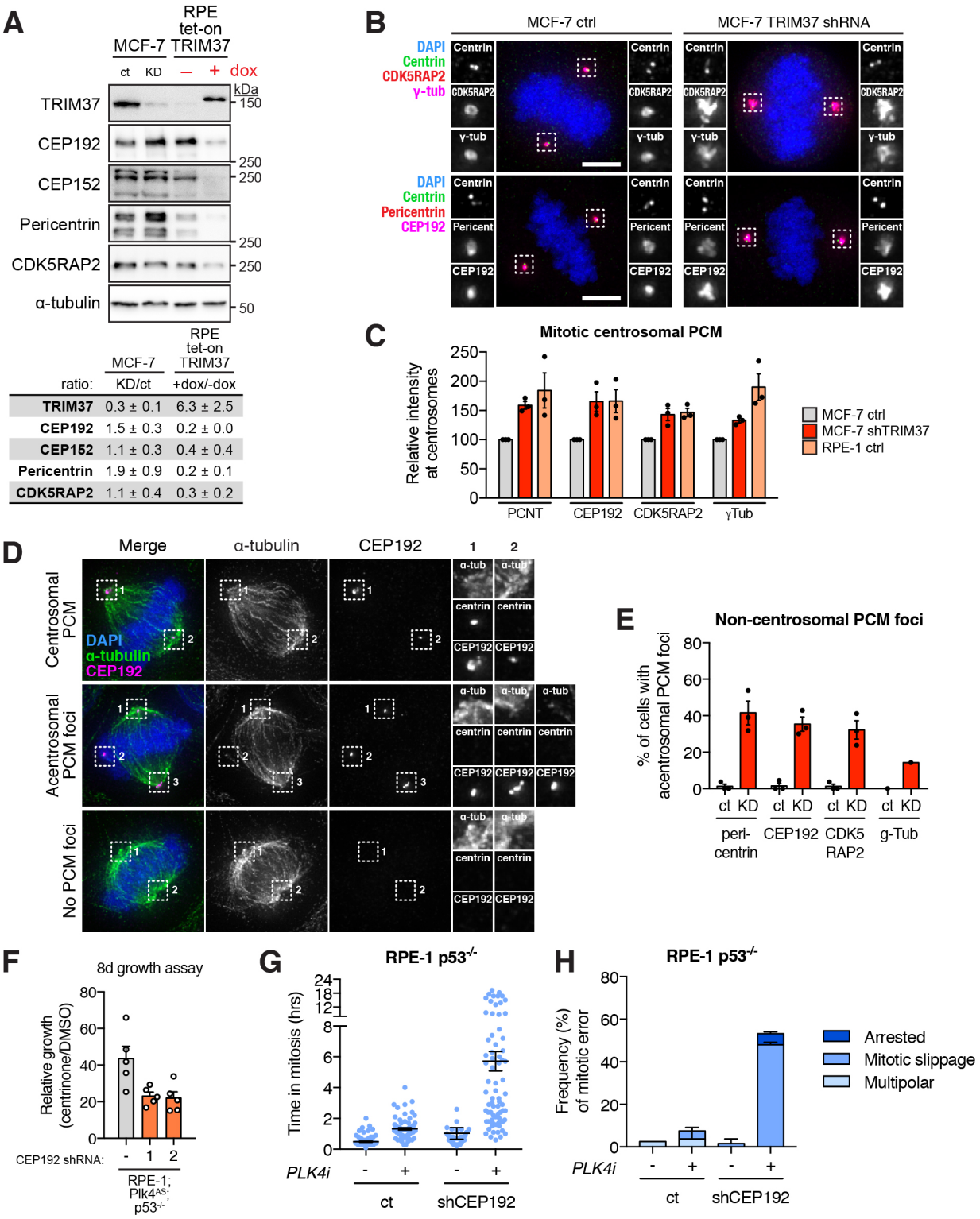

ratio:	MCF-7 KD/ct	RPE tet-on TRIM37 +dox/-dox
TRIM37	0.3 ± 0.1	6.3 ± 2.5
CEP192	1.5 ± 0.3	0.2 ± 0.0
CEP152	1.1 ± 0.3	0.4 ± 0.4
Pericentrin	1.9 ± 0.9	0.2 ± 0.1
CDK5RAP2	1.1 ± 0.4	0.3 ± 0.2

Figure 27. Depleted PCM upon TRIM37-amplification is responsible for mitotic catastrophe in the absence of centrosomes.

(A) Immunoblot showing levels of TRIM37 and PCM components in MCF-7 and RPE-1 following TRIM37 knockdown or overexpression, respectively. Normalized levels, averaged over three independent replicates, are shown in table format.

(B) Representative images of centrosomal PCM levels in control and TRIM37-shRNA expressing MCF-7 mitotic cells.

(C) Quantification of centrosomal PCM signal in mitotic cells, comparing MCF-7 control, MCF-7 TRIM37-shRNA, and RPE-1 control samples.

(D) Example images of centrinone-treated MCF-7s, illustrating the different observed distributions of PCM foci in centrinone-treated cells.

(E) Quantification of PCM foci distribution in mitotic, centrinone-treated MCF-7s that lacked centrosomes (n = 3, >25 cells per experiment).

(F) Relative growth after an 8 d growth assay with control and CEP192-shRNA expressing RPE-1 $Plk4^{AS}$ $p53^{-/-}$ cells, showing a ratio of growth in PLK4i over DMSO.

(G) Mitotic duration in RPE-1; $p53^{-/-}$; $Plk4^{AS}$ cells expressing H2B-EGFP and TagRFP-tubulin, either control or expressing CEP192-shRNA, grown in either DMSO or 3MB-PP1 for 3 d. Data are means ± SEM (n = 2, >30 cells per experiment).

(H) Quantification of frequency of mitotic errors in of the same samples as described in (G). Bars represent the mean of >80 cells from two independent experiments.

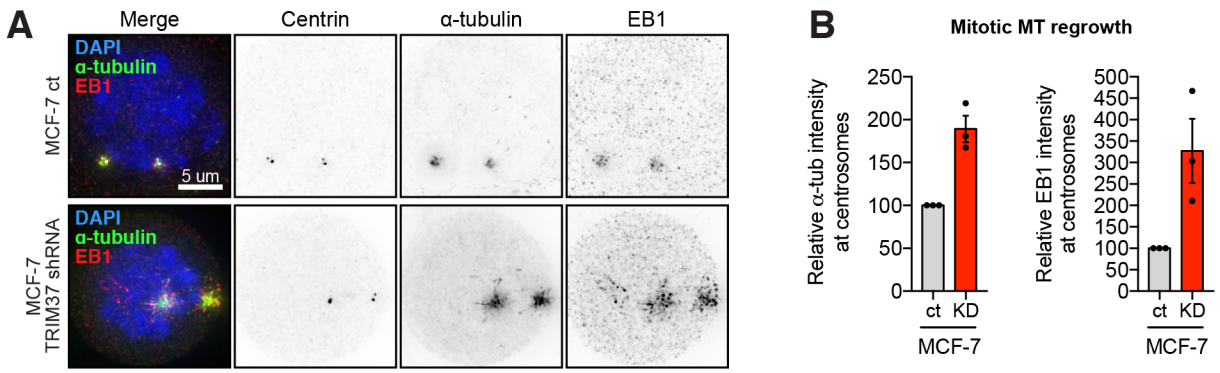

Figure 28. TRIM37 suppresses microtubule organizing capacity of the centrosome.

(A) Representative images of microtubule regrowth following nocodazole washout in control and TRIM37-shRNA expressing MCF-7 mitotic cells.

(B) Quantification of microtubule regrowth following nocodazole washout in control and TRIM37-shRNA expressing MCF-7 mitotic cells. (*n* = 3, >25 cells per experiment).

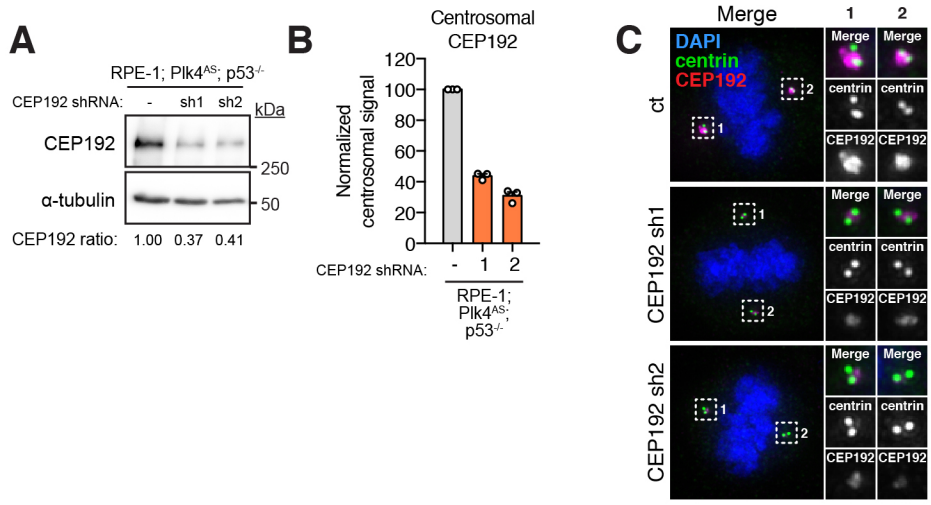

Figure 29. CEP192 is depleted following stable shRNA expression.

(A) Immunoblot showing the CEP192 levels in RPE-1; $p53^{-/-}$; $Plk4^{AS}$ cells, comparing parental control cells with those expressing CEP192-shRNA.

(B) Quantification of mitotic centrosomal CEP192 signal in the same cells as described in (A).

(C) Representative images of centrosomal CEP192 signal in the same cells as described in (A).

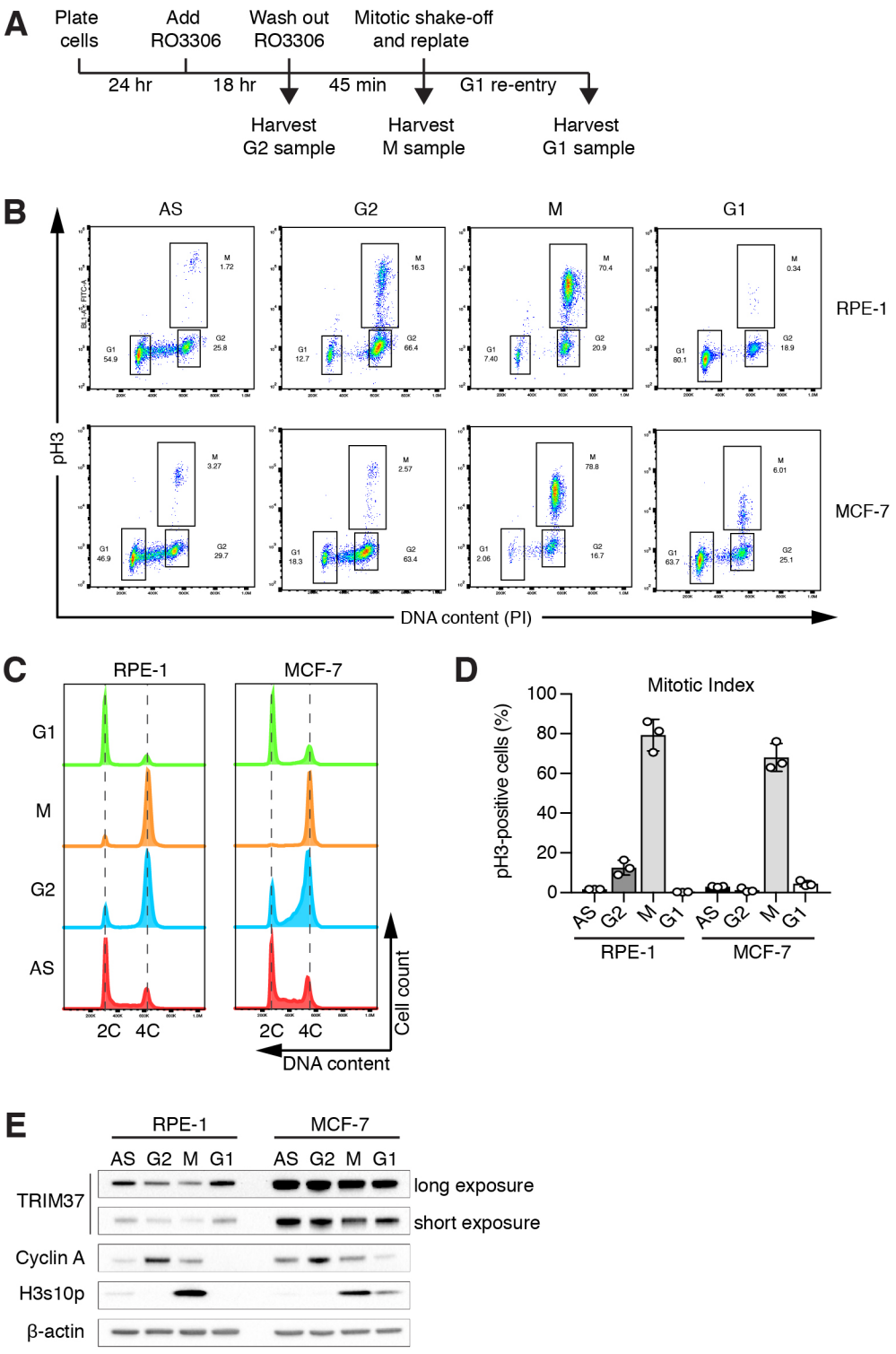

Figure 30. TRIM37 protein levels are downregulated during mitosis.

(A) Schematic of the experimental protocol used for cell cycle synchronization. M, mitotic phase

(B) Representative flow cytometry plots of synchronized cell cycle samples harvested according to a. Samples were subjected to dual flow cytometry staining of pH3 (mitotic cells) and propidium iodide (PI) to determine synchronization efficiency. Top, RPE-1; Bottom, MCF-7. N = 3 independent experiments. AS, asynchronous.

(C) DNA content analysis of samples from b by flow cytometry. Left, RPE-1; Right, MCF-7.

(D) Mitotic Index of cell cycle samples was determined by quantification of the percentage of pH3-positive cells with 4N DNA content from the analysis in (B). Mean ± s.d.

(E) Western blot analysis of endogenous TRIM37, cyclin A and phospho-histone H3 in samples analyzed in (B). β-actin was used as a loading control. N = 3 independent experiments. AS, asynchronous.

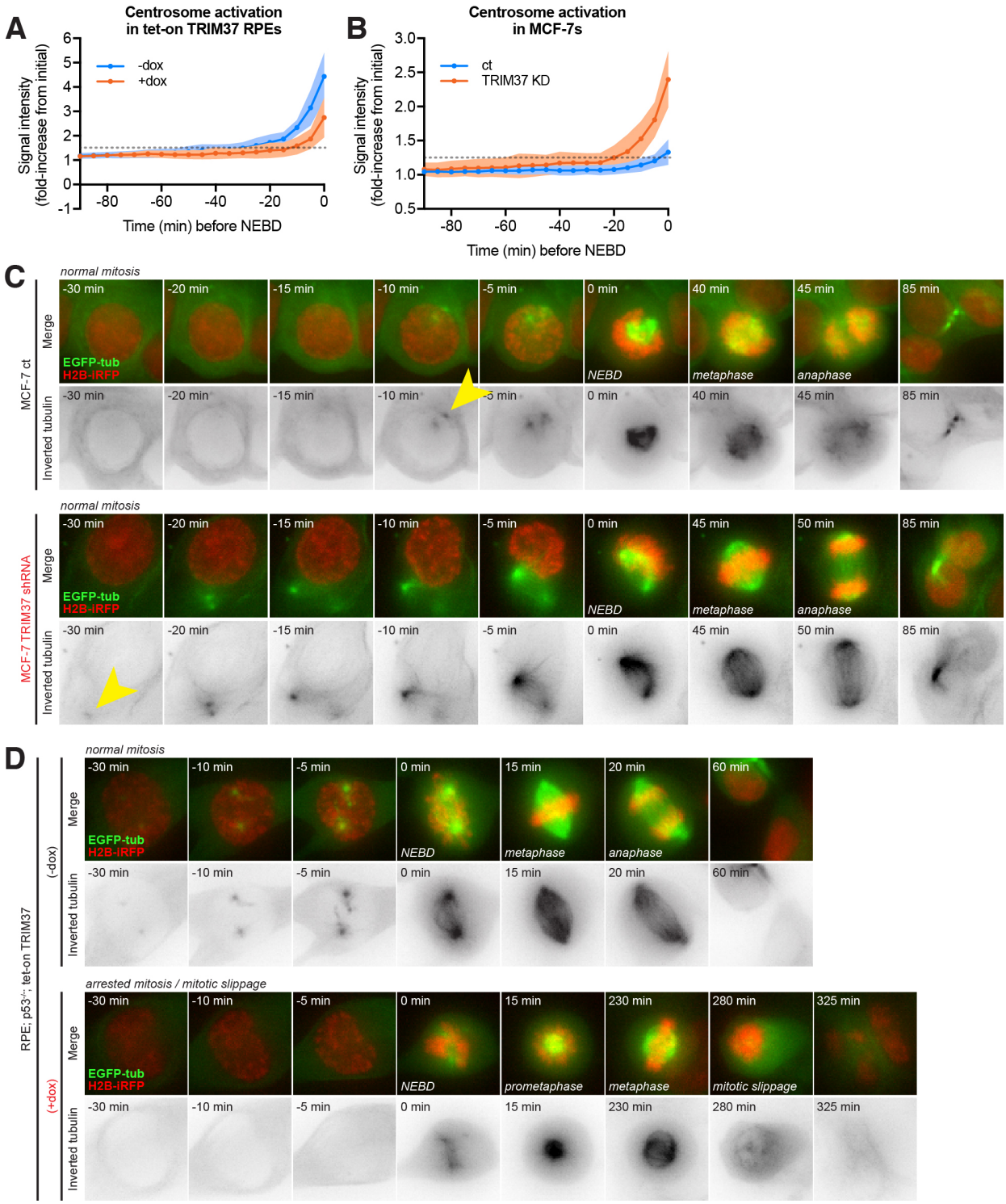

Figure 31. TRIM37 overexpression results in delayed centrosome maturation during mitotic entry.

(A) Quantification of centrosomal alpha-tubulin intensity from timelapse movies of dividing cells, in RPE-1 tet-on TRIM37 cells in minus- or plus-dox conditions. (n = 1, >20 cells).

(B) Quantification of centrosomal alpha-tubulin intensity from timelapse movies of dividing cells, in MCF-7 cells expressing either control or TRIM37 shRNA. (n = 1, >20 cells).

(C) Representative timelapse images of centrosome maturation in MCF-7 cells.

(D) Representative timelapse images of centrosome maturation in RPE-1 tet-on TRIM37 cells.

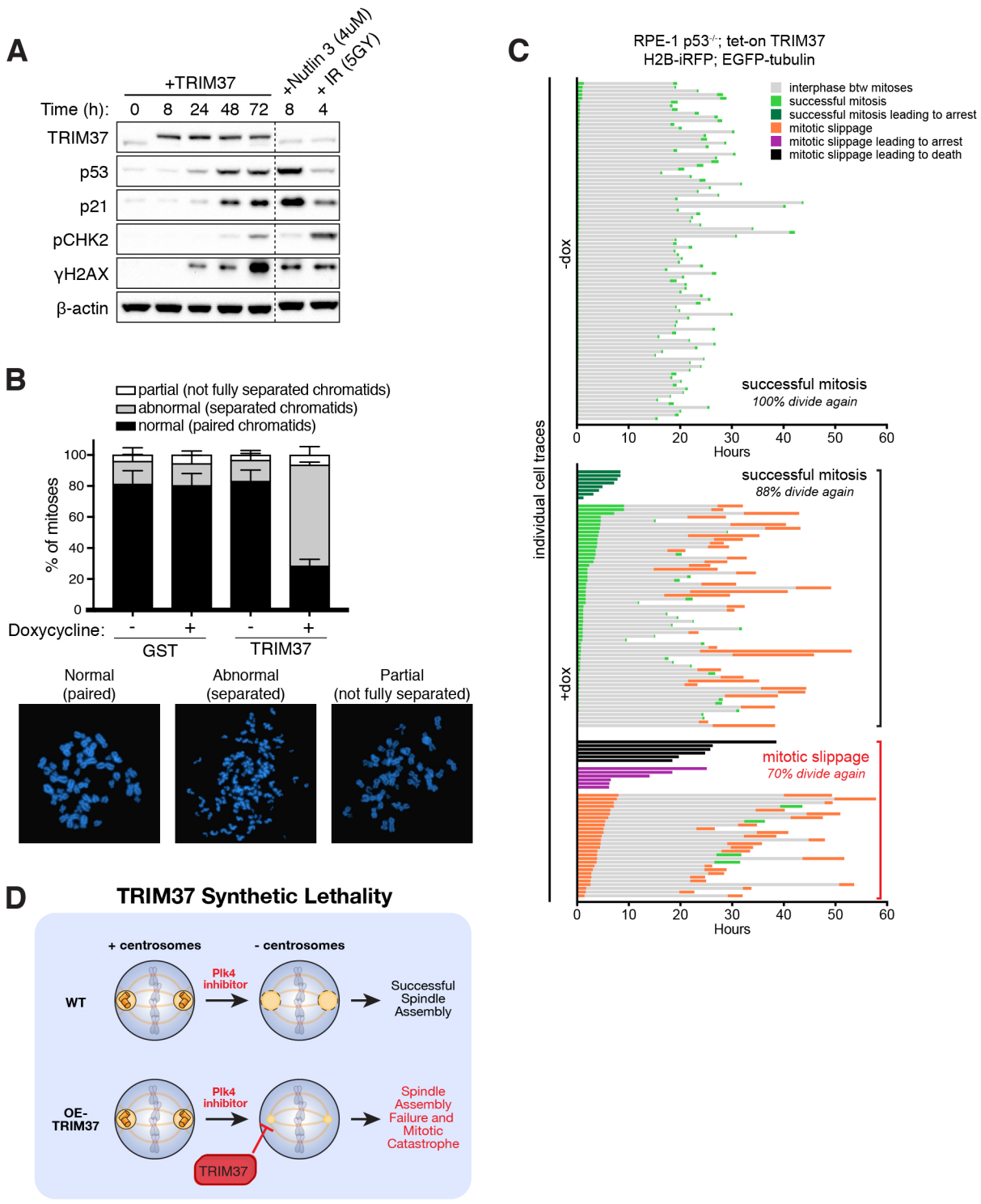

Figure 32. TRIM37 overexpression promotes genome instability.

(A) Western blot analysis of RPE1 $p53^{+/+}$ cells overexpressing TRIM37 under a doxycycline-inducible system. Samples were taken at 8, 24, 48 and 72 hours (h) post doxycycline addition. 5

Gy irradiation (IR) and 4 μM Nutlin-3 (N3) treatment were used as positive controls for the induction of DNA damage and p53 responses respectively. β-Actin was used as a loading control.

(B) Bottom; Representative metaphase images of sister chromatid pairing phenotypes (normal, abnormal and partial) observed in spreads of RPE1 $p53^{-/-}$ cells overexpressing GST (control) or TRIM37 for 48 h. Top; Quantification of the phenotypes observed in each condition. n = 3 independent experiments, between 106 and 137 metaphases were analysed in each experiment. Mean ± s.d.

(C) An analysis of mitotic duration and cell fate over the course of a 60-hour timelapse. (*n* = 2, >90 cells total).

(D) A model for the synthetic lethality seen in 17q23 amplified breast cancers.

Chapter 5

Materials and Methods

Cell culture

hTERT-RPE-1 cells were grown in DMEM:F12 medium (Corning Cellgro) containing 10% fetal bovine serum (Sigma), 0.348% sodium bicarbonate, 100 U/ml penicillin, 100 U/ml streptomycin and 2 mM L-glutamine. HEK293FT cells were grown in DMEM medium (Corning Cellgro) containing 10% fetal bovine serum (Sigma), 100 U/ml penicillin, 100 U/ml streptomycin and 2 mM L-glutamine. Cells were maintained at 37°C in a 5% CO_2 atmosphere with 21% oxygen. Nocodazole (Sigma) was dissolved in DMSO and used at a final concentration of 3.3 μM, Mimosine (Sigma) was dissolved in dilute HCl and used at a final concentration of 250 μM, PD0332991 (PD, Sigma) was dissolved in DMSO and used at a final concentration of 1 μM, SB203580 (Sigma) was dissolved in DMSO and used at a final concentration of 10 μM, doxorubicin (Sigma) was dissolved in water and used at a final concentration of 200 ng/mL, and indole-3-acetic acid (IAA, Sigma) was dissolved in water and used at 500 μM unless otherwise stated. 3MB-PP1 (Millipore) was dissolved in DMSO and used at a final concentration of 10 μM, centrinone (a kind gift from Karen Oegema, Ludwig Institute for Cancer Research, CA) was dissolved in DMSO and used at a final concentration of 125 nM, cycloheximide (Sigma) was

dissolved in water and used at a final concentration of 50 μg/ml, KU-55933 (TOCRIS) was dissolved in DMSO and used at a final concentration of 10 μM, and Nutlin-3 (Cayman Chemical) was dissolved in DMSO and used at a final concentration of 10 μM unless otherwise stated.

Creation of Plk4$^{AID/AID}$ hTERT-RPE-1 cells

Gene targeting was performed using Adeno-Associated Virus (AAV) (Berdougo et al., 2009; Holland et al., 2012b). To generate the Plk4 targeting construct we cloned an AID degron followed by a 3xFLAG epitope tag, a translational stop codon, the Plk4 3′ UTR and 150 bp's of adjacent genomic sequence into the pBluescript derivative pNY to create the AID-3xFLAG-3′UTR, *loxP*-Neo^{R}-*loxP* vector. 5′ and 3′ homology arms were PCR amplified from genomic RPE1 DNA and cloned on either side of the central AID-3xFLAG-3′UTR, *loxP*-Neo^{R}-*loxP* cassette. The entire insert was transferred into the pAAV vector backbone and fully sequenced to verify its integrity. hTERT-RPE1 cells were transduced with infectious AID-3xFLAG-3′UTR;*loxP*-Neo^{R}-*loxP*-containing AAV particles. Plk4$^{AID/+}$ cells were isolated by selection in G418 and resistant clones screened by PCR using primers binding in Neo^{R} and a genomic sequence adjacent to the targeting construct. A second targeting construct was created containing a HA tag in place of the FLAG epitope tag and a Blast^{R} in place of Neo^{R}. An additional round of gene targeting was performed in Plk4$^{AID/+}$ cells using AID-HA-3'UTR;*loxP*-Blast^{R}-*loxP* AAV particles. The intergenic position of the Neo^{R} and Blast^{R} cassettes reduces the likelihood that their presence will disrupt the function of the Plk4 gene. This facilitates the isolation of homozygous targeted alleles by allowing concurrent selection for both markers. Plk4$^{AID/AID}$ cells were isolated by co-selection in G418 and Blasticidin and resistant clones screened by PCR

using primers that bind in Blast^{R} and a genomic sequence adjacent to the targeting construct. Two independent Plk4$^{AID/AID}$ clones were created and the targeted Plk4-AID-3xFLAG and Plk4-AID-3xHA alleles were sequenced to verify their integrity. osTIR1-9xMyc was cloned into the pBabe backbone under the control of the gag promoter and introduced into Plk4$^{AID/AID}$ cells using retroviral delivery. Stable integrants were selected in 5 μg/ml puromycin and single clones isolated by limiting dilution. EGFP-tagged Cep63 was cloned into the FUGW backbone under the control of the Ubiquitin promoter, while EGFP-tagged histone H2B and TagRFP-Tubulin were cloned into the FUGW backbone under the control of the CMV promoter. All three constructs were introduced into Plk4$^{AID/AID}$ cells using lentiviral delivery and single clones isolated by limiting dilution. A p53 shRNA was introduced into cells using lentiviral delivery and single clones isolated using fluorescence activated cell sorting (Tiscornia et al., 2003).

Creation of Plk4^{AS} hTERT-RPE-1 cells

To facilitate genome editing, we set out to knockout out the puromycin acetyltransferase (PAC) expressed in hTERT-RPE-1 cells. An sgRNA targeting PAC (TGTCGAGCCCGACGCGCGTG) was cloned into the px458 expression vector (Addgene #48138) that coexpresses the sgRNA from a U6 promoter and SpCas9-2A-GFP from a CMV promoter. Cells were transfected with the px458 plasmid and GFP-positive single cells isolated by FACS. Clones were split into duplicate wells and one well received 3 μg/ml puromycin. A clone that showed complete cell death after 3 days of puromycin treatment was selected and used in all experiments described in the manuscript.

Plk4 gene targeting was performed in hTERT-RPE-1 cells using CRISPR/Cas9. In brief, a sgRNA targeting Plk4 (AGATAGCAATTATGTGTATC) was cloned into the px459 expression vector (Addgene #48139) that coexpresses the sgRNA from a U6 promoter and SpCas9-2A-puromycin from a CMV promoter. Cells were cotransfected with a 1:20 molar ratio of the px459 plasmid and a 160-bp single-stranded oligonucleotide repair template. The repair template introduced the L89G mutation, a silent AflIII restriction site, and a mutation in the SpCas9 protospacer adjacent motif (PAM) to prevent recutting after homology-directed repair. Transfected cells were selected for 3 days with 3 μg/ml puromycin and single clones were isolated by limiting dilution. Genomic DNA was isolated from single clones and subjected to PCR using the following primers (forward, GCAGGAATGGTACAGAGAGTCC; reverse, GCAAAACTTTTATCCACCCAAA). PCR products were digested with AflIII for 2 h. Clones with digested PCR products were sequenced to verify insertion of the L89G mutation. A single clone was identified that possessed the L89G mutation in one allele and a frameshift single basepair insertion in the second allele that led to the creation of a premature stop codon at amino acid 94.

L89G donor oligonucleotide:

CTGAATTTTTGTATATTTTAATTTATTATGCCCTTTCACATTTCAGCTTTATAACTAT TTTGAAGATAGCAATTACGTGTATCTAGTAGGAGAAATGTGCCATAATGGAGAAAT GAACAGGTATCTAAAGAAT AGAGTGAAACCCTTCTCAGAAAATGAAG

Antibody Production

A C-terminal Plk4 fragment (amino acid 510-970) was cloned into a pET-23b bacterial expression vector (Novagen) containing a C-terminal 6xHis tag. Recombinant protein was

purified from *E. coli* using Ni–NTA beads (QIAGEN) and used for immunization (ProSci). A STIL C-terminal peptide VGTFLDVKRLRQLPKLF (amino acid 1271-1287) was synthesized and conjugated to KLH for immunization. Rabbit immune sera were affinity purified using standard procedures. Affinity purified antibodies were directly conjugated to DyLight 550 and DyLight 650 fluorophores (Thermo Scientific) for use in immunofluorescence.

Immunoprecipitation of FLAG-Plk4

To purify Plk4-AID-3xFLAG, cells were lysed in lysis buffer (10 mM Tris pH 7.5, 0.1% Triton X-100, 100 mM NaCl, 1 mM EDTA, 1 mM EGTA, 50 mM NaF, 20 mM, β-glycerophosphate, 0.1 mM DTT, 200 nM microcystin, 1 mM PMSF and 1 mM LPC), sonicated and soluble extracts prepared. The supernatant was incubated with anti-FLAG M2 magnetic beads (Sigma). Beads were washed 5 times in lysis buffer and immunopurified protein analyzed by immunoblot.

Western Blotting

For immunoblot analysis protein samples were separated by SDS-PAGE, transferred onto nitrocellulose membranes with a Trans-Blot Turbo Transfer System (BioRad) and then probed with the following antibodies: DM1A (mouse anti-α-tubulin, Sigma, 1:5000), Plk4 (rabbit, this study, 1:3200), FLAG M2 (mouse, Sigma, 1:1000), STIL (rabbit, Bethyl, 1:2500), Yap (rabbit, Cell Signaling, 1:1000), p-Yap Ser127 (rabbit, Cell Signaling, 1:1000), LATS2 (rabbit, Cell Signaling, 1:1000), p-LATS S1077 (rabbit, (Yu et al., 2010), a kind gift of Duojia Pan, Johns Hopkins School of Medicine, 1:500), p-Histone H2A.X (Ser139) (rabbit, Cell Signaling, 1:1000), YL1/2 (rat anti-α-tubulin, Pierce Antibodies, 1:3000), p53 (mouse, CalBiochem, 1:1000), 53BP1 (rabbit, Novus Biologicals, 1:2000), MDM2 (mouse, Thermo Fisher Scientific,

1:1000), Chk2 (mouse, EMD Millipore, 1:500), phospho-KAP1 (Ser824) (rabbit, Bethyl, 1:1000), phospho-p53 (Ser15) (rabbit, Cell Signaling, 1:1000), CDKN1A (rabbit, NeoBioLab, 1:1000), RNF168 (rabbit, Millipore, 1:1000), and LATS1 (rabbit, Cell Signaling, 1:1000).

Immunofluorescence

For immunofluorescence, cells were grown on 18-mm glass coverslips and fixed for 10 min in either 4% formaldehyde at room temperature, or 100% ice cold methanol at -20°C for 10 minutes. Cells were blocked in 2.5% FBS, 200 mM glycine, and 0.1% Triton X-100 in PBS for 1 hour. Antibody incubations were conducted in the blocking solution for 1 hour. DNA was detected using DAPI and cells were mounted in Prolong Antifade (Invitrogen). Staining was performed with the following primary antibodies: GTU-88 (mouse anti-γ-tubulin, Abcam, 1:250), Centrin (mouse, Millipore, 1:1000), CNAP1 (guinea pig, raised against the CNAP1 peptide sequence SPTQQDGRGQKNSDAKC, a kind gift from Olaf Stemmann, University of Bayreuth, Germany, 1:1000), CEP152 (rabbit, Bethyl, 1:5000), Plk4-650 (directly labeled rabbit, this study, 1:1000), STIL-550 (directly labeled rabbit, this study, 1:1000), CEP135 (rabbit, raised against CEP135 a.a. 695-838, a kind gift from Anthony Hyman, Max Planck Institute for Molecular Cell Biology and Genetics, Germany, 1:1000), CEP192-Cy3 (directly-labeled rabbit, raised against CEP192 a.a. 1-211, a kind gift from Karen Oegema, Ludwig Institute for Cancer Research, CA, 1:1000), SAS6-Cy3 (directly-labeled rabbit, raised against SAS6 a.a. 501-657, a kind gift from Karen Oegema, Ludwig Institute for Cancer Research, CA, 1:1000), SAS6 (mouse, Santa Cruz Biotechnology, 1:1000), CPAP-Cy3 (directly-labeled rabbit, a kind gift from Karen Oegema, Ludwig Institute for Cancer Research, CA, 1:1000), CENP-F (sheep, raised against CENP-F a.a. 1363-1640, a kind gift from Stephen Taylor, the University of Manchester,

UK, 1:1000), HA (rat anti-HA High Affinity, Roche, 1:200), FLAG (mouse anti-FLAG M2, Sigma, 1:1000), p53 (mouse, CalBiochem, 1:1000), 53BP1 (rabbit, Novus Biologicals, 1:2000), 53BP1 (mouse, Millipore, 1:1000), USP28 (rabbit, Proteintech, 1:1000), p-Histone H2A.X (Ser139) (rabbit, Cell Signaling, 1:1000), CEP192-Cy5 (directly-labeled goat, raised against CEP192 a.a. 1-211, this study, 1:1000), and BUB1 (sheep, raised against BUB1 a.a. 336-489, a kind gift from Stephen Taylor, the University of Manchester, UK, 1:1000). Secondary donkey antibodies were conjugated to Alexa Fluor® 488, 555 or 650 (Life Technologies).

For the cell cycle analysis of Plk4 levels shown in Figure 1E, cells were pulsed with EdU for 1 hour prior to fixation in 100% ice cold methanol at -20°C for 10 minutes. Cells were washed three times with 0.1% Triton X-100, stained using a Click-It EdU Alexa Fluor 555 imaging kit (Life Technologies) and blocked in 2.5% FBS, 200 mM glycine, 0.1% Triton X-100 in PBS for 1 hour. Immunofluorescence microscopy was performed using the following antibodies: CENP-F (sheep, raised against CENP-F a.a. 1363-1640, a kind gift from Stephen Taylor, the University of Manchester, UK, 1:1000), GTU-88 (mouse anti-γ-tubulin, Abcam, 1:250), and Plk4-650 (directly labeled rabbit, this study, 1:1000). G1 phase cells were classified as CENP-F and EdU negative, S phase cells were classified as EdU positive, and G2 phase cells were classified as CENP-F positive and EdU negative. The γ-tubulin staining was used to define the position of the centrosome.

For EdU analysis of cell cycling, cells were pulsed with EdU for 12 hours prior to fixation in 100% ice cold methanol at -20°C for 10 minutes. Cells were washed three times with PBST and stained using a Click-It EdU Alexa Fluor 555 imaging kit (Life Technologies).

Immunofluorescence microscopy and image analysis

Immunofluorescence images were collected using a Deltavision Elite system (GE Healthcare) controlling a Scientific CMOS camera (pco.edge 5.5). Acquisition parameters were controlled by SoftWoRx suite (GE Healthcare). Images were collected at room temperature (25°C) using an Olympus 40x 1.35 NA, 60x 1.42 NA or Olympus 100x 1.4 NA oil objective at 0.2 μm z-sections and subsequently deconvolved in SoftWoRx suite. Images were acquired using Applied Precision immersion oil (N=1.516). For quantitation of signal intensity at the centrosome, deconvolved 2D maximum intensity projections were saved as 16-bit TIFF images. Signal intensity was determined using ImageJ, by drawing a circular region of interest (ROI) around the centriole (ROI S). A larger concentric circle (ROI L) was drawn around ROI S. ROI S and L were transferred to the channel of interest and the signal in ROI S was calculated using the following formula:

$$IS - [(IL-IS/AL-AS) \times AS]$$

A = Area, I = Integrated pixel intensity.

For quantitation of nuclear p53 signal intensity, 2D maximum intensity projections were saved as 16-bit TIFF images, and DAPI signal was used to threshold nuclei as regions of interest. For each nucleus, the integrated density of p53 signal was divided by nuclear area to give a signal/area value. Data were averaged over all cells in the panel, and normalized to untreated population.

Live cell microscopy

Cells were seeded into 4-chamber, 35 mm glass bottom culture dishes (Greiner) and maintained at 37°C in an environmental control station. Images were collected using a Deltavision Elite system (GE Healthcare) controlling a Scientific CMOS camera (pco.edge 5.5.). Images were acquired with a Olympus 40x 1.35 NA oil lens using Applied Precision immersion oil (N=1.526). Every 5 minutes, 7 x 3 μm z-sections were acquired for EGFP and RFP and maximum intensity projection created using softWoRx (Applied Precision). Alternatively, cells were imaged using a Zeiss 40x 1.4 NA PlanApochromat oil-immersion objective on a Zeiss LSM 780 confocal equipped with a solid-state 488 nm and 514 nm laser and a spectral GaAsP detector. Images were acquired using Carl Zeiss immersion oil (N=1.518). Acquisition parameters, shutters, and focus were controlled by ZEN black software (Zeiss). 15 X 1.6 μm z-sections were acquired simultaneously for EGFP and/or RFP at 5 or 10 min time intervals. Maximum intensity projections were created using ZEN black. Movies were assembled and analyzed using FIJI. Mitotic duration was calculated as the time taken from nuclear envelope breakdown to mitotic exit.

Mitotic timer experiments and cell lineage tracing

For nocodazole treatment, coverslips were assembled into observation chambers with medium containing 0.08 μM nocodazole and fields of cells were continuously followed by video time-lapse microscopy at 37°C for 6 hours. After 6 hours, the field of view was marked with a diamond scribe; the bottom of the observation chamber was removed and washed out with fresh medium several times before being reassembled with fresh medium as previously described (Uetake and Sluder, 2012). The previously marked fields were continuously followed for at least 96 hours. Lineage tracing of individual cells was performed as previously described (Uetake et

al., 2007). For IAA and SB203580 treatment, cells were exposed to the drug for the duration of imaging. Images were collected using a Leica DMRXE microscope equipped with phase-contrast optics and a Leica 10x 0.3 NA objective. Images were captured with an Orca ER (Hamamatsu) camera using HCT software (Hamamatsu) and exported as AVI movies to be viewed with QuickTime (Apple).

Electron Microcopy

Cells were grown on 35 mm Nunclon Delta-treated culture dishes (Thermo Scientific) and fixed (2.5% glutaraldehyde, 3 mM $MgCl_2$, 0.1 M sodium cacodylate, pH 7.2) for one hour at room temperature. Cells were rinsed with 0.1 M sodium cacodylate, and post-fixed with 0.5% OsO_4 for one hour on ice. Following a dH_2O rinse, plates were stained with 0.1% tannic acid, rinsed twice with dH2O, and stained en bloc with 2% aqueous uranyl acetate. Samples were dehydrated in a graded series of ethanol, embedded in Eponate 12 resin (Ted Pella), and polymerized at 60°C overnight. Ultrathin 60 nm sections were cut, mounted, and stained with 1% tannic acid, followed by 2% uranyl acetate and lead citrate. Images were acquired using a Hitachi 7600 TEM equipped with an AMT CCD 2080x2048 pixel camera (Advanced Microscopy Techniques).

Flow cytometry

To prepare cells for flow cytometry, cell pellets were fixed in cold 70% EtOH for 24 hours, washed once in PBS and resuspended in PBS supplemented with 0.5 mg/ml RNAse A and 50 mg/ml Propidium Iodide (PI). Samples were incubated at room temperature for 30 minutes and analyzed on a flow cytometer (FACSCalibur; Becton Dickinson). For RNA interference, 2 x 10^5

cells were seeded in a 6-well plate and duplexed siRNAs introduced using RNAiMax (Life Technologies). siRNA directed against STIL (5' GCUCCAAACAGUUUCUGCUGGAAU-3') was purchased from Dharmacon.

Cell clonogenic and growth assays

For clonogenic assays, 500 cells were seeded in a 10 cm^2 culture dish and left to grow for ~10 days until colonies were visible by eye. Cells were fixed in methanol for 30 min at room temperature and colonies were stained with crystal violet (Sigma-Aldrich). Plates were imaged on a G:BOX Chemi XX6 (Syngene) and the fraction of the dish upon which growth occurred was determined using GeneSys software (Syngene). The percentage clonogenic survival was calculated by dividing the area of growth in the presence of 3MB-PP1 by the area of growth of control DMSO-treated cells multiplied by 100.

Lentiviral production and transduction

The lentiCas9-Blasticidin (Addgene #52962), lentiGuide-Puromycin (Addgene #52963) or lentiGuide-Neomycin (this study) plasmid was co-transfected into 293FT cells with the lentiviral packaging plasmids psPAX2 and pMD2.G (Addgene 12260 and 12259). Briefly, 8 x 10^6 293FT cells were seeded into a Poly-L-Lysine coated 15 cm culture dish the day before transfection. For each 15 cm dish the following DNA was diluted in 1.2 ml of OptiMEM (Thermo Fisher Scientific): 9 µg of lentiviral vector, 12 µg of psPAX2 and 3 µg of pMD2.G. Separately, 72 µl of 1 µg/µl 25 kDa polyethylenimine (PEI; Sigma) was diluted into 1.2 ml of OptiMEM, briefly vortexed, and incubated at room temperature for 5 min. After incubation, the DNA and PEI mixtures were combined, briefly vortexed, and incubated at room temperature for 20 min.

During this incubation, the culture media was replaced with 17 ml of pre-warmed DMEM + 1 % FBS. The transfection mixture was then added drop-wise to the 15 cm dish. Viral particles were harvested 48 hr after the media change and filtered through a 0.45 μm PVDF syringe filter. The filtered supernatant was either concentrated in 100 kDa Amicon Ultra Centrifugal Filter Units (Millipore) or used directly to infect cells. Aliquots were snap-frozen and stored at –80°C. For transduction, lentiviral particles were diluted in complete growth media supplemented with 10 μg/ml polybrene (Sigma) and added to cells.

CRISPR/Cas9 GeCKO screen

CRISPR/Cas9 pooled, knockout screens were performed essentially as described (Chen et al., 2015; Shalem et al., 2014). Briefly, PAC knockout hTERT-RPE1 or Plk4^{AS} hTERT-RPE1 cells were transduced with the lentiCas9-Blasticidin virus and single cells sorted into 96-well plates to isolate clonal cell lines. Multiple clones were screened by immunoblot for the FLAG epitope fused to the Cas9 protein. A SpCas9-hTERT-RPE1 and Plk4^{AS}-SpCas9-hTERT-RPE1 cell line with a high level of SpCas9 expression was selected for further use.

The human GeCKO v2 plasmid library was purchased from Addgene (#1000000049) and plasmid DNA amplified according to the manufacturers instructions. To produce virus, the GeCKO pooled plasmid library and the lentiviral packaging plasmids psPAX2 and pMD2.G were co-transfected into 40x 15 cm culture dishes of 293FT cells. Transfections were performed as described above and viral particles harvested, filtered and concentrated. Aliquots were stored at –80°C.

Cells were transduced with the GeCKO library via spinfection. To find the optimal virus volumes for achieving an MOI ~ 0.1, each new batch of virus was titered by spinfecting 3 x 10^6 cells with several different volumes of virus. Briefly, 3 x 10^6 cells per well were seeded into a 12 well plate in growth media supplemented with 10 μg/ml polybrene. Each well received a different titrated virus amount (between 5 and 50 μl) along with a no-transduction control. The plate was centrifuged at 2,000 rpm for 2 hr at room temperature. After the spin, media was aspirated and fresh growth media was added. The following day, cells were counted and each well was split into duplicate wells. One well received 3 μg/ml puromycin (Sigma) for 3 days. Cells were counted and the percent transduction calculated as the cell count from the replicate with puromycin divided by the cell count from the replicate without puromycin multiplied by 100. The virus volume yielding a MOI closest to 0.1 was chosen for large-scale transductions. An MOI of 0.1 - 0.2 corresponds to a single transduction percentage of 95% at 10% survival and 90% at 20% survival, respectively.

For the pooled screen a total of 12 x 10^7 SpCas9-hTERT-RPE1 or Plk4^{AS}-SpCas9-hTERT-RPE1 cells were infected at MOI ~0.1 and selected with puromycin at 3 μg/ml for 3 days. MOI was calculated using a control well infected in parallel following the same procedure outlined above. Infected cells were expanded under puromycin selection for 7 days to allow editing to proceed to completion. After 7 days, 2 x 10^7 cells were spun down and frozen for genomic DNA extraction. In addition, 12 x 10^6 cells were seeded into each of two 15 cm culture dishes. One dish was treated with DMSO and the other with either centrinone (SpCas9-hTERT-RPE1 cells) or 3MB-PP1 (Plk4^{AS}-SpCas9-hTERT-RPE1 cells). Cells were either passaged or fresh media was added

every 3-4 days. Cell pellets with a minimum of 2 x 10^7 cells were taken at 42 days after drug addition at which point the screen was terminated.

Frozen cell pellets were thawed and genomic DNA was extracted with a GenElute Mammalian Genomic DNA extraction kit (Sigma). The sgRNA library for each sample was amplified and prepared for Illumina sequencing using a two-step PCR procedure, where the first PCR includes enough genomic DNA to preserve full library complexity and the second PCR adds appropriate sequencing adapters to the products from the first PCR. For the first PCR, a region containing the sgRNA cassette was amplified using primers specific to the sgRNA-expression vector:
lentiGuide-PCR-F: AATGGACTATCATATGCTTACCGTAACTTGAAAGTATTTCG
lentiGuide-PCR1-R: CTTTAGTTTGTATGTCTGTTGCTATTATGTCTACTATTCTTTCC

The thermocycling parameters for the first PCR were: 98°C for 30 s, 18-24 cycles of (98°C for 1 s, 62°C for 5 s, 72°C for 35 s), and 72°C for 1 min. 1.5 µg of DNA was used in each PCR reaction. Assuming 6.6 pg of DNA per cell, ~100x representation of the GeCKO library required ~80 µg of DNA per sample (54 PCR reactions). The resulting amplicons for each sample were pooled, gel purified and used for amplification with barcoded second PCR primers. For each sample we performed 14 reactions.
Primers for the second PCR include both a variable length sequence to increase library complexity and an 8 bp barcode for multiplexing of different biological samples:
F2:
AATGATACGGCGACCACCGAGATCTACACTCTTTCCCTACACGACGCTCTTCCGATC
T(4-7 bp random nucleotides)(8 bp barcode)TCTTGTGGAAAGGACGAAACACCG

R2:

CAAGCAGAAGACGGCATACGAGATGTGACTGGAGTTCAGACGTGTGCTCTTCCGAT

CTTCTACTATTCTTTCCCCTGCACTGT

5 µl of the product from the first PCR reaction were used and the thermocycling parameters for the second PCR were: 98°C for 30 s, 18-24 cycles of (98°C for 1 s, 70°C for 5 s, 72°C for 35 s). Second PCR products were pooled, gel purified and quantified using the Next Library Quantification Kit (NEB). Diluted libraries with 5% PhiX were sequenced with MiSeq (Illumina).

Sequencing data were processed for sgRNA representation using custom scripts. Briefly, sequencing reads were first demultiplexed using the barcodes in the forward primer and then trimmed to leave only the 20 bp sgRNA sequences. The spacer sequences were then mapped to the spacers of the designed sgRNA library using Bowtie (Langmead et al., 2009). For mapping, a maximum of one mismatch was allowed in the 20 bp sgRNA sequence. Mapped sgRNA sequences were then quantified by counting the total number of reads. The total numbers of reads for all sgRNAs in each sample were normalized. Genes were ranked using the MaGeCK algortihm which takes into account sgRNA enrichment as well as the number of sgRNAs targeting a particular gene (Li et al., 2014).

Statistics

Differences were determined by one-tailed *t* test, and annotated following the nomenclature: ns ($p > 0.05$), * ($p \leq 0.05$), ** ($p \leq 0.01$), *** ($p \leq 0.001$).

References

Arquint, C., and E.A. Nigg. 2014. STIL microcephaly mutations interfere with APC/C-mediated degradation and cause centriole amplification. *Curr Biol*. 24:351-360.

Arquint, C., K.F. Sonnen, Y.D. Stierhof, and E.A. Nigg. 2012. Cell-cycle-regulated expression of STIL controls centriole number in human cells. *J Cell Sci*. 125:1342-1352.

Balestra, F.R., P. Strnad, I. Fluckiger, and P. Gonczy. 2013. Discovering regulators of centriole biogenesis through siRNA-based functional genomics in human cells. *Dev Cell*. 25:555-571.

Banin, S., L. Moyal, S. Shieh, Y. Taya, C.W. Anderson, L. Chessa, N.I. Smorodinsky, C. Prives, Y. Reiss, Y. Shiloh, and Y. Ziv. 1998. Enhanced phosphorylation of p53 by ATM in response to DNA damage. *Science*. 281:1674-1677.

Basto, R., J. Lau, T. Vinogradova, A. Gardiol, C.G. Woods, A. Khodjakov, and J.W. Raff. 2006. Flies without centrioles. *Cell*. 125:1375-1386.

Bazzi, H., and K.V. Anderson. 2014. Acentriolar mitosis activates a p53-dependent apoptosis pathway in the mouse embryo. *Proc Natl Acad Sci U S A*. 111:E1491-1500.

Bedard, P.L., D.W. Cescon, G. Fletcher, T. Denny, R. Brokx, P. Sampson, M.R. Bray, D.J. Slamon, T.W. Mak, and Z.A. Wainberg. 2016. Abstract CT066: First-in-human phase I trial of the oral PLK4 inhibitor CFI-400945 in patients with advanced solid tumors. *Cancer Research*. 76:CT066.

Berdougo, E., M.E. Terret, and P.V. Jallepalli. 2009. Functional dissection of mitotic regulators through gene targeting in human somatic cells. *Methods Mol Biol*. 545:21-37.

Bettencourt-Dias, M., A. Rodrigues-Martins, L. Carpenter, M. Riparbelli, L. Lehmann, M.K. Gatt, N. Carmo, F. Balloux, G. Callaini, and D.M. Glover. 2005. SAK/PLK4 is required for centriole duplication and flagella development. *Curr Biol*. 15:2199-2207.

Bielski, C.M., A. Zehir, A.V. Penson, M.T.A. Donoghue, W. Chatila, J. Armenia, M.T. Chang, A.M. Schram, P. Jonsson, C. Bandlamudi, P. Razavi, G. Iyer, M.E. Robson, Z.K. Stadler, N. Schultz, J. Baselga, D.B. Solit, D.M. Hyman, M.F. Berger, and B.S. Taylor. 2018. Genome doubling shapes the evolution and prognosis of advanced cancers. *Nature Genetics*. 50:1189-1195.

Branon, T.C., J.A. Bosch, A.D. Sanchez, N.D. Udeshi, T. Svinkina, S.A. Carr, J.L. Feldman, N. Perrimon, and A.Y. Ting. 2018. Efficient proximity labeling in living cells and organisms with TurboID. *Nature biotechnology*. 36:880.

Brownlee, C.W., J.E. Klebba, D.W. Buster, and G.C. Rogers. 2011. The Protein Phosphatase 2A regulatory subunit Twins stabilizes Plk4 to induce centriole amplification. *J Cell Biol*. 195:231-243.

Canman, C.E., D.S. Lim, K.A. Cimprich, Y. Taya, K. Tamai, K. Sakaguchi, E. Appella, M.B. Kastan, and J.D. Siliciano. 1998. Activation of the ATM kinase by ionizing radiation and phosphorylation of p53. *Science*. 281:1677-1679.

Chen, S., N.E. Sanjana, K. Zheng, O. Shalem, K. Lee, X. Shi, D.A. Scott, J. Song, J.Q. Pan, R. Weissleder, H. Lee, F. Zhang, and P.A. Sharp. 2015. Genome-wide CRISPR screen in a mouse model of tumor growth and metastasis. *Cell*. 160:1246-1260.

Coelho, P.A., L. Bury, B. Sharif, M.G. Riparbelli, J. Fu, G. Callaini, D.M. Glover, and M. Zernicka-Goetz. 2013. Spindle formation in the mouse embryo requires Plk4 in the absence of centrioles. *Dev Cell*. 27:586-597.

Cunha-Ferreira, I., I. Bento, A. Pimenta-Marques, S.C. Jana, M. Lince-Faria, P. Duarte, J. Borrego-Pinto, S. Gilberto, T. Amado, D. Brito, A. Rodrigues-Martins, J. Debski, N. Dzhindzhev, and M. Bettencourt-Dias. 2013. Regulation of autophosphorylation controls PLK4 self-destruction and centriole number. *Curr Biol*. 23:2245-2254.

Cunha-Ferreira, I., A. Rodrigues-Martins, I. Bento, M. Riparbelli, W. Zhang, E. Laue, G. Callaini, D.M. Glover, and M. Bettencourt-Dias. 2009. The SCF/Slimb ubiquitin ligase limits centrosome amplification through degradation of SAK/PLK4. *Curr Biol*. 19:43-49.

Curtis, C., S.P. Shah, S.-F. Chin, G. Turashvili, O.M. Rueda, M.J. Dunning, D. Speed, A.G. Lynch, S. Samarajiwa, Y. Yuan, S. Gräf, G. Ha, G. Haffari, A. Bashashati, R. Russell, S. McKinney, M. Group, C. Caldas, S. Aparicio, C. Curtis†, S.P. Shah, C. Caldas, S. Aparicio, J.D. Brenton, I. Ellis, D. Huntsman, S. Pinder, A. Purushotham, L. Murphy, C. Caldas, S. Aparicio, C. Caldas, H. Bardwell, S.-F. Chin, C. Curtis, Z. Ding, S. Gräf, L. Jones, B. Liu, A.G. Lynch, I. Papatheodorou, S.J. Sammut, G. Wishart, S. Aparicio, S. Chia, K. Gelmon, D. Huntsman, S. McKinney, C. Speers, G. Turashvili, P. Watson, I. Ellis, R. Blamey, A. Green, D. Macmillan, E. Rakha, A. Purushotham, C. Gillett, A. Grigoriadis, S. Pinder, E. de Rinaldis, A. Tutt, L. Murphy, M. Parisien, S. Troup, C. Caldas, S.-F. Chin, D. Chan, C. Fielding, A.-T. Maia, S. McGuire, M. Osborne, S.M. Sayalero, I. Spiteri, J. Hadfield, S. Aparicio, G. Turashvili, L. Bell, K. Chow, N. Gale, D. Huntsman, M. Kovalik, Y. Ng, L. Prentice, C. Caldas, S. Tavaré, C. Curtis, M.J. Dunning, S. Gräf, A.G. Lynch, O.M. Rueda, R. Russell, S. Samarajiwa, D. Speed, F. Markowetz, Y. Yuan, J.D. Brenton, S. Aparicio, S.P. Shah, A. Bashashati, et al. 2012. The genomic and transcriptomic architecture of 2,000 breast tumours reveals novel subgroups. *Nature*. 486:346.

Dammermann, A., T. Muller-Reichert, L. Pelletier, B. Habermann, A. Desai, and K. Oegema. 2004. Centriole assembly requires both centriolar and pericentriolar material proteins. *Dev Cell*. 7:815-829.

Debec, A., W. Sullivan, and M. Bettencourt-Dias. 2010. Centrioles: active players or passengers during mitosis? *Cell Mol Life Sci*. 67:2173-2194.

Doil, C., N. Mailand, S. Bekker-Jensen, P. Menard, D.H. Larsen, R. Pepperkok, J. Ellenberg, S. Panier, D. Durocher, J. Bartek, J. Lukas, and C. Lukas. 2009. RNF168 binds and amplifies ubiquitin conjugates on damaged chromosomes to allow accumulation of repair proteins. *Cell*. 136:435-446.

Dzhindzhev, N.S., G. Tzolovsky, Z. Lipinszki, S. Schneider, R. Lattao, J. Fu, J. Debski, M. Dadlez, and D.M. Glover. 2014. Plk4 Phosphorylates Ana2 to Trigger Sas6 Recruitment and Procentriole Formation. *Curr Biol*. 24:2526-2532.

Eckerdt, F., T.M. Yamamoto, A.L. Lewellyn, and J.L. Maller. 2011. Identification of a polo-like kinase 4-dependent pathway for de novo centriole formation. *Curr Biol*. 21:428-432.

Fong, C.S., G. Mazo, T. Das, J. Goodman, M. Kim, B.P. O'Rourke, D. Izquierdo, and M.-F.B. Tsou. 2016a. 53BP1 and USP28 mediate p53-dependent cell cycle arrest in response to centrosome loss and prolonged mitosis. *eLife*. 5:e16270.

Fong, C.S., G. Mazo, T. Das, J. Goodman, M. Kim, B.P. O'Rourke, D. Izquierdo, and M.F. Tsou. 2016b. 53BP1 and USP28 mediate p53-dependent cell cycle arrest in response to centrosome loss and prolonged mitosis. *Elife*. 5.

Fry, D.W., P.J. Harvey, P.R. Keller, W.L. Elliott, M. Meade, E. Trachet, M. Albassam, X. Zheng, W.R. Leopold, N.K. Pryer, and P.L. Toogood. 2004. Specific inhibition of cyclin-dependent kinase 4/6 by PD 0332991 and associated antitumor activity in human tumor xenografts. *Mol Cancer Ther*. 3:1427-1438.

Ganem, N.J., H. Cornils, S.Y. Chiu, K.P. O'Rourke, J. Arnaud, D. Yimlamai, M. Thery, F.D. Camargo, and D. Pellman. 2014. Cytokinesis failure triggers hippo tumor suppressor pathway activation. *Cell*. 158:833-848.

Ganem, N.J., S.A. Godinho, and D. Pellman. 2009. A mechanism linking extra centrosomes to chromosomal instability. *Nature*. 460:278-282.

Ganem, N.J., Z. Storchova, and D. Pellman. 2007. Tetraploidy, aneuploidy and cancer. *Current Opinion in Genetics & Development*. 17:157-162.

Gomez-Ferreria, M.A., U. Rath, D.W. Buster, S.K. Chanda, J.S. Caldwell, D.R. Rines, and D.J. Sharp. 2007. Human Cep192 Is Required for Mitotic Centrosome and Spindle Assembly. *Current Biology*. 17:1960-1966.

Gonczy, P. 2012. Towards a molecular architecture of centriole assembly. *Nat Rev Mol Cell Biol*. 13:425-435.

Graser, S., Y.D. Stierhof, S.B. Lavoie, O.S. Gassner, S. Lamla, M. Le Clech, and E.A. Nigg. 2007. Cep164, a novel centriole appendage protein required for primary cilium formation. *J Cell Biol*. 179:321-330.

Guderian, G., J. Westendorf, A. Uldschmid, and E.A. Nigg. 2010. Plk4 trans-autophosphorylation regulates centriole number by controlling betaTrCP-mediated degradation. *J Cell Sci*. 123:2163-2169.

Habedanck, R., Y.D. Stierhof, C.J. Wilkinson, and E.A. Nigg. 2005. The Polo kinase Plk4 functions in centriole duplication. *Nat Cell Biol*. 7:1140-1146.

Heald, R., R. Tournebize, A. Habermann, E. Karsenti, and A. Hyman. 1997. Spindle Assembly in Xenopus Egg Extracts: Respective Roles of Centrosomes and Microtubule Self-Organization. *The Journal of Cell Biology*. 138:615.

Hermsen, M.A., J.P. Baak, G.A. Meijer, J.M. Weiss, J.W. Walboomers, P.J. Snijders, and P.J. van Diest. 1998. Genetic analysis of 53 lymph node-negative breast carcinomas by CGH and relation to clinical, pathological, morphometric, and DNA cytometric prognostic factors. *The Journal of pathology*. 186:356-362.

Holland, A.J., and D.W. Cleveland. 2014. Polo-like kinase 4 inhibition: a strategy for cancer therapy? *Cancer Cell*. 26:151-153.

Holland, A.J., D. Fachinetti, S. Da Cruz, Q. Zhu, B. Vitre, M. Lince-Faria, D. Chen, N. Parish, I.M. Verma, M. Bettencourt-Dias, and D.W. Cleveland. 2012a. Polo-like kinase 4 controls centriole duplication but does not directly regulate cytokinesis. *Mol Biol Cell*. 23:1838-1845.

Holland, A.J., D. Fachinetti, Q. Zhu, M. Bauer, I.M. Verma, E.A. Nigg, and D.W. Cleveland. 2012b. The autoregulated instability of Polo-like kinase 4 limits centrosome duplication to once per cell cycle. *Genes Dev*. 26:2684-2689.

Holland, A.J., W. Lan, S. Niessen, H. Hoover, and D.W. Cleveland. 2010a. Polo-like kinase 4 kinase activity limits centrosome overduplication by autoregulating its own stability. *J Cell Biol*. 188:191-198.

Holland, A.J., W. Lan, S. Niessen, H. Hoover, and D.W. Cleveland. 2010b. Polo-like kinase 4 kinase activity limits centrosome overduplication by autoregulating its own stability. *J Cell Biol*. 188:191-198.

Huen, M.S., R. Grant, I. Manke, K. Minn, X. Yu, M.B. Yaffe, and J. Chen. 2007. RNF8 transduces the DNA-damage signal via histone ubiquitylation and checkpoint protein assembly. *Cell*. 131:901-914.

Hussein, D., and S.S. Taylor. 2002. Farnesylation of Cenp-F is required for G2/M progression and degradation after mitosis. *J Cell Sci*. 115:3403-3414.
Insolera, R., H. Bazzi, W. Shao, K.V. Anderson, and S.H. Shi. 2014. Cortical neurogenesis in the absence of centrioles. *Nat Neurosci*. 17:1528-1535.
Isola, J.J., O.P. Kallioniemi, L.W. Chu, S.A. Fuqua, S.G. Hilsenbeck, C.K. Osborne, and F.M. Waldman. 1995. Genetic aberrations detected by comparative genomic hybridization predict outcome in node-negative breast cancer. *The American journal of pathology*. 147:905-911.
Iwabuchi, K., P.L. Bartel, B. Li, R. Marraccino, and S. Fields. 1994. Two cellular proteins that bind to wild-type but not mutant p53. *Proc Natl Acad Sci U S A*. 91:6098-6102.
Izquierdo, D., W.J. Wang, K. Uryu, and M.F. Tsou. 2014. Stabilization of cartwheel-less centrioles for duplication requires CEP295-mediated centriole-to-centrosome conversion. *Cell Rep*. 8:957-965.
Joo, W.S., P.D. Jeffrey, S.B. Cantor, M.S. Finnin, D.M. Livingston, and N.P. Pavletich. 2002. Structure of the 53BP1 BRCT region bound to p53 and its comparison to the Brca1 BRCT structure. *Genes Dev*. 16:583-593.
Joukov, V., Johannes C. Walter, and A. De Nicolo. 2014. The Cep192-Organized Aurora A-Plk1 Cascade Is Essential for Centrosome Cycle and Bipolar Spindle Assembly. *Molecular Cell*. 55:578-591.
Jullien, D., P. Vagnarelli, W.C. Earnshaw, and Y. Adachi. 2002. Kinetochore localisation of the DNA damage response component 53BP1 during mitosis. *J Cell Sci*. 115:71-79.
Kallioniemi, A., O.P. Kallioniemi, J. Piper, M. Tanner, T. Stokke, L. Chen, H.S. Smith, D. Pinkel, J.W. Gray, and F.M. Waldman. 1994. Detection and mapping of amplified DNA sequences in breast cancer by comparative genomic hybridization. *Proceedings of the National Academy of Sciences of the United States of America*. 91:2156-2160.
Khodjakov, A., R.W. Cole, B.R. Oakley, and C.L. Rieder. 2000. Centrosome-independent mitotic spindle formation in vertebrates. *Current Biology*. 10:59-67.
Khodjakov, A., and C.L. Rieder. 2001. Centrosomes enhance the fidelity of cytokinesis in vertebrates and are required for cell cycle progression. *J Cell Biol*. 153:237-242.
Khodjakov, A., C.L. Rieder, G. Sluder, G. Cassels, O. Sibon, and C.L. Wang. 2002. De novo formation of centrosomes in vertebrate cells arrested during S phase. *J Cell Biol*. 158:1171-1181.
Kitagawa, D., I. Vakonakis, N. Olieric, M. Hilbert, D. Keller, V. Olieric, M. Bortfeld, M.C. Erat, I. Fluckiger, P. Gonczy, and M.O. Steinmetz. 2011. Structural basis of the 9-fold symmetry of centrioles. *Cell*. 144:364-375.
Kittaneh, M., A.J. Montero, and S. Glück. 2013. Molecular Profiling for Breast Cancer: A Comprehensive Review. *Biomarkers in Cancer*. 5:BIC.S9455.
Klebba, J.E., D.W. Buster, A.L. Nguyen, S. Swatkoski, M. Gucek, N.M. Rusan, and G.C. Rogers. 2013. Polo-like kinase 4 autodestructs by generating its Slimb-binding phosphodegron. *Curr Biol*. 23:2255-2261.
Knobel, P.A., R. Belotserkovskaya, Y. Galanty, C.K. Schmidt, S.P. Jackson, and T.H. Stracker. 2014. USP28 is recruited to sites of DNA damage by the tandem BRCT domains of 53BP1 but plays a minor role in double-strand break metabolism. *Mol Cell Biol*. 34:2062-2074.
Ko, M.A., C.O. Rosario, J.W. Hudson, S. Kulkarni, A. Pollett, J.W. Dennis, and C.J. Swallow. 2005. Plk4 haploinsufficiency causes mitotic infidelity and carcinogenesis. *Nat Genet*. 37:883-888.

Kolas, N.K., J.R. Chapman, S. Nakada, J. Ylanko, R. Chahwan, F.D. Sweeney, S. Panier, M. Mendez, J. Wildenhain, T.M. Thomson, L. Pelletier, S.P. Jackson, and D. Durocher. 2007. Orchestration of the DNA-damage response by the RNF8 ubiquitin ligase. *Science*. 318:1637-1640.

Kollman, J.M., A. Merdes, L. Mourey, and D.A. Agard. 2011. Microtubule nucleation by γ-tubulin complexes. *Nature Reviews Molecular Cell Biology*. 12:709.

Kuukasjarvi, T., R. Karhu, M. Tanner, M. Kahkonen, A. Schaffer, N. Nupponen, S. Pennanen, A. Kallioniemi, O.P. Kallioniemi, and J. Isola. 1997. Genetic heterogeneity and clonal evolution underlying development of asynchronous metastasis in human breast cancer. *Cancer research*. 57:1597-1604.

La Terra, S., C.N. English, P. Hergert, B.F. McEwen, G. Sluder, and A. Khodjakov. 2005. The de novo centriole assembly pathway in HeLa cells: cell cycle progression and centriole assembly/maturation. *J Cell Biol*. 168:713-722.

Lambrus, B.G., V. Daggubati, Y. Uetake, P.M. Scott, K.M. Clutario, G. Sluder, and A.J. Holland. 2016. A USP28-53BP1-p53-p21 signaling axis arrests growth after centrosome loss or prolonged mitosis. *J Cell Biol*. 214:143-153.

Lambrus, B.G., Y. Uetake, K.M. Clutario, V. Daggubati, M. Snyder, G. Sluder, and A.J. Holland. 2015. p53 protects against genome instability following centriole duplication failure. *J Cell Biol*. 210:63-77.

Langmead, B., C. Trapnell, M. Pop, and S.L. Salzberg. 2009. Ultrafast and memory-efficient alignment of short DNA sequences to the human genome. *Genome Biol*. 10:R25.

Lecland, N., A. Debec, A. Delmas, S. Moutinho-Pereira, N. Malmanche, A. Bouissou, C. Dupre, A. Jourdan, B. Raynaud-Messina, H. Maiato, and A. Guichet. 2013. Establishment and mitotic characterization of new Drosophila acentriolar cell lines from DSas-4 mutant. *Biol Open*. 2:314-323.

Leidel, S., M. Delattre, L. Cerutti, K. Baumer, and P. Gonczy. 2005. SAS-6 defines a protein family required for centrosome duplication in C. elegans and in human cells. *Nat Cell Biol*. 7:115-125.

Li, W., H. Xu, T. Xiao, L. Cong, M.I. Love, F. Zhang, R.A. Irizarry, J.S. Liu, M. Brown, and X.S. Liu. 2014. MAGeCK enables robust identification of essential genes from genome-scale CRISPR/Cas9 knockout screens. *Genome Biol*. 15:554.

Liu, L., C.Z. Zhang, M. Cai, J. Fu, G.G. Chen, and J. Yun. 2012. Downregulation of polo-like kinase 4 in hepatocellular carcinoma associates with poor prognosis. *PLoS One*. 7:e41293.

Luders, J., U.K. Patel, and T. Stearns. 2006. GCP-WD is a gamma-tubulin targeting factor required for centrosomal and chromatin-mediated microtubule nucleation. *Nature cell biology*. 8:137-147.

Mailand, N., S. Bekker-Jensen, H. Faustrup, F. Melander, J. Bartek, C. Lukas, and J. Lukas. 2007. RNF8 ubiquitylates histones at DNA double-strand breaks and promotes assembly of repair proteins. *Cell*. 131:887-900.

Mallette, F.A., F. Mattiroli, G. Cui, L.C. Young, M.J. Hendzel, G. Mer, T.K. Sixma, and S. Richard. 2012. RNF8- and RNF168-dependent degradation of KDM4A/JMJD2A triggers 53BP1 recruitment to DNA damage sites. *Embo J*. 31:1865-1878.

Mallette, F.A., and S. Richard. 2012. K48-linked ubiquitination and protein degradation regulate 53BP1 recruitment at DNA damage sites. *Cell Res*. 22:1221-1223.

Marshall, W.F., Y. Vucica, and J.L. Rosenbaum. 2001. Kinetics and regulation of de novo centriole assembly. Implications for the mechanism of centriole duplication. *Curr Biol*. 11:308-317.

Mason, J.M., D.C. Lin, X. Wei, Y. Che, Y. Yao, R. Kiarash, D.W. Cescon, G.C. Fletcher, D.E. Awrey, M.R. Bray, G. Pan, and T.W. Mak. 2014. Functional characterization of CFI-400945, a Polo-like kinase 4 inhibitor, as a potential anticancer agent. *Cancer Cell*. 26:163-176.

Massard, C., S. Michiels, C. Ferté, M.-C. Le Deley, L. Lacroix, A. Hollebecque, L. Verlingue, E. Ileana, S. Rosellini, S. Ammari, M. Ngo-Camus, R. Bahleda, A. Gazzah, A. Varga, S. Postel-Vinay, Y. Loriot, C. Even, I. Breuskin, N. Auger, B. Job, T. De Baere, F. Deschamps, P. Vielh, J.-Y. Scoazec, V. Lazar, C. Richon, V. Ribrag, E. Deutsch, E. Angevin, G. Vassal, A. Eggermont, F. André, and J.-C. Soria. 2017. High-Throughput Genomics and Clinical Outcome in Hard-to-Treat Advanced Cancers: Results of the MOSCATO 01 Trial. *Cancer Discovery*. 7:586.

Meitinger, F., J.V. Anzola, M. Kaulich, A. Richardson, J.D. Stender, C. Benner, C.K. Glass, S.F. Dowdy, A. Desai, A.K. Shiau, and K. Oegema. 2016a. 53BP1 and USP28 mediate p53 activation and G1 arrest after centrosome loss or extended mitotic duration. *The Journal of Cell Biology*. 214:155-166.

Meitinger, F., J.V. Anzola, M. Kaulich, A. Richardson, J.D. Stender, C. Benner, C.K. Glass, S.F. Dowdy, A. Desai, A.K. Shiau, and K. Oegema. 2016b. 53BP1 and USP28 mediate p53 activation and G1 arrest after centrosome loss or extended mitotic duration. *J Cell Biol*. 214:155-166.

Miki-Noumura, T. 1977. Studies on the de novo formation of centrioles: aster formation in the activated eggs of sea urchin. *J Cell Sci*. 24:203-216.

Monni, O., M. Barlund, S. Mousses, J. Kononen, G. Sauter, M. Heiskanen, P. Paavola, K. Avela, Y. Chen, M.L. Bittner, and A. Kallioniemi. 2001. Comprehensive copy number and gene expression profiling of the 17q23 amplicon in human breast cancer. *Proceedings of the National Academy of Sciences of the United States of America*. 98:5711-5716.

Moyer, T.C., K.M. Clutario, B.G. Lambrus, V. Daggubati, and A.J. Holland. 2015. Binding of STIL to Plk4 activates kinase activity to promote centriole assembly. *J Cell Biol*. 209:863-878.

Nigg, E.A., and J.W. Raff. 2009. Centrioles, centrosomes, and cilia in health and disease. *Cell*. 139:663-678.

Nishimura, K., T. Fukagawa, H. Takisawa, T. Kakimoto, and M. Kanemaki. 2009. An auxin-based degron system for the rapid depletion of proteins in nonplant cells. *Nat Methods*. 6:917-922.

Ohta, M., T. Ashikawa, Y. Nozaki, H. Kozuka-Hata, H. Goto, M. Inagaki, M. Oyama, and D. Kitagawa. 2014. Direct interaction of Plk4 with STIL ensures formation of a single procentriole per parental centriole. *Nat Commun*. 5:5267.

Palazzo, R.E., E. Vaisberg, R.W. Cole, and C.L. Rieder. 1992. Centriole duplication in lysates of Spisula solidissima oocytes. *Science*. 256:219-221.

Parssinen, J., T. Kuukasjarvi, R. Karhu, and A. Kallioniemi. 2007. High-level amplification at 17q23 leads to coordinated overexpression of multiple adjacent genes in breast cancer. *Br J Cancer*. 96:1258-1264.

Peel, N., N.R. Stevens, R. Basto, and J.W. Raff. 2007. Overexpressing centriole-replication proteins in vivo induces centriole overduplication and de novo formation. *Curr Biol*. 17:834-843.

Pellegrino, R., D.F. Calvisi, S. Ladu, V. Ehemann, T. Staniscia, M. Evert, F. Dombrowski, P. Schirmacher, and T. Longerich. 2010. Oncogenic and tumor suppressive roles of polo-like kinases in human hepatocellular carcinoma. *Hepatology*. 51:857-868.

Prosser, S.L., and L. Pelletier. 2017. Mitotic spindle assembly in animal cells: a fine balancing act. *Nature Reviews Molecular Cell Biology*. 18:187.

Rodrigues-Martins, A., M. Riparbelli, G. Callaini, D.M. Glover, and M. Bettencourt-Dias. 2007. Revisiting the role of the mother centriole in centriole biogenesis. *Science*. 316:1046-1050.

Rogers, G.C., N.M. Rusan, D.M. Roberts, M. Peifer, and S.L. Rogers. 2009. The SCF Slimb ubiquitin ligase regulates Plk4/Sak levels to block centriole reduplication. *J Cell Biol*. 184:225-239.

Roux, K.J., D.I. Kim, M. Raida, and B. Burke. 2012. A promiscuous biotin ligase fusion protein identifies proximal and interacting proteins in mammalian cells. *The Journal of Cell Biology*. 196:801.

Shalem, O., N.E. Sanjana, E. Hartenian, X. Shi, D.A. Scott, T.S. Mikkelsen, D. Heckl, B.L. Ebert, D.E. Root, J.G. Doench, and F. Zhang. 2014. Genome-scale CRISPR-Cas9 knockout screening in human cells. *Science*. 343:84-87.

Silkworth, W.T., I.K. Nardi, L.M. Scholl, and D. Cimini. 2009. Multipolar spindle pole coalescence is a major source of kinetochore mis-attachment and chromosome mis-segregation in cancer cells. *PLoS One*. 4:e6564.

Sinclair, C.S., M. Rowley, A. Naderi, and F.J. Couch. 2003. The 17q23 Amplicon and Breast Cancer. *Breast Cancer Research and Treatment*. 78:313-322.

Sir, J.H., A.R. Barr, A.K. Nicholas, O.P. Carvalho, M. Khurshid, A. Sossick, S. Reichelt, C. D'Santos, C.G. Woods, and F. Gergely. 2011. A primary microcephaly protein complex forms a ring around parental centrioles. *Nat Genet*. 43:1147-1153.

Sir, J.H., M. Putz, O. Daly, C.G. Morrison, M. Dunning, J.V. Kilmartin, and F. Gergely. 2013. Loss of centrioles causes chromosomal instability in vertebrate somatic cells. *J Cell Biol*. 203:747-756.

Strnad, P., S. Leidel, T. Vinogradova, U. Euteneuer, A. Khodjakov, and P. Gonczy. 2007. Regulated HsSAS-6 levels ensure formation of a single procentriole per centriole during the centrosome duplication cycle. *Dev Cell*. 13:203-213.

Suh, M.R., J.W. Han, Y.R. No, and J. Lee. 2002. Transient concentration of a gamma-tubulin-related protein with a pericentrin-related protein in the formation of basal bodies and flagella during the differentiation of Naegleria gruberi. *Cell motility and the cytoskeleton*. 52:66-81.

Szollosi, D., P. Calarco, and R.P. Donahue. 1972. Absence of centrioles in the first and second meiotic spindles of mouse oocytes. *J Cell Sci*. 11:521-541.

Szollosi, D., and J.P. Ozil. 1991. De novo formation of centrioles in parthenogenetically activated, diploidized rabbit embryos. *Biology of the cell / under the auspices of the European Cell Biology Organization*. 72:61-66.

Tang, C.J., R.H. Fu, K.S. Wu, W.B. Hsu, and T.K. Tang. 2009. CPAP is a cell-cycle regulated protein that controls centriole length. *Nat Cell Biol*. 11:825-831.

Tang, C.J.C., S.Y. Lin, W.B. Hsu, Y.N. Lin, C.T. Wu, Y.C. Lin, C.W. Chang, K.S. Wu, and T.K. Tang. 2011. The human microcephaly protein STIL interacts with CPAP and is required for procentriole formation. *Embo J*. 30:4790-4804.

Tang, P., J. Wang, and P. Bourne. 2008. Molecular classifications of breast carcinoma with similar terminology and different definitions: are they the same? *Human pathology*. 39:506-513.

Thompson, S.L., and D.A. Compton. 2010. Proliferation of aneuploid human cells is limited by a p53-dependent mechanism. *J Cell Biol*. 188:369-381.

Tiscornia, G., O. Singer, M. Ikawa, and I.M. Verma. 2003. A general method for gene knockdown in mice by using lentiviral vectors expressing small interfering RNA. *Proc Natl Acad Sci U S A*. 100:1844-1848.

Tsou, M.F., and T. Stearns. 2006. Controlling centrosome number: licenses and blocks. *Curr Opin Cell Biol*. 18:74-78.

Uetake, Y., J. Loncarek, J.J. Nordberg, C.N. English, S. La Terra, A. Khodjakov, and G. Sluder. 2007. Cell cycle progression and de novo centriole assembly after centrosomal removal in untransformed human cells. *J Cell Biol*. 176:173-182.

Uetake, Y., and G. Sluder. 2010. Prolonged prometaphase blocks daughter cell proliferation despite normal completion of mitosis. *Curr Biol*. 20:1666-1671.

Uetake, Y., and G. Sluder. 2012. Practical Methodology for Long-Term Recordings of Live Human Cells. Academic Press. 43–52 pp.

van Breugel, M., M. Hirono, A. Andreeva, H.A. Yanagisawa, S. Yamaguchi, Y. Nakazawa, N. Morgner, M. Petrovich, I.O. Ebong, C.V. Robinson, C.M. Johnson, D. Veprintsev, and B. Zuber. 2011. Structures of SAS-6 suggest its organization in centrioles. *Science*. 331:1196-1199.

van Breugel, M., R. Wilcken, S.H. McLaughlin, T.J. Rutherford, and C.M. Johnson. 2014. Structure of the SAS-6 cartwheel hub from Leishmania major. *eLife*. 3:e01812.

Vulprecht, J., A. David, A. Tibelius, A. Castiel, G. Konotop, F. Liu, F. Bestvater, M.S. Raab, H. Zentgraf, S. Izraeli, and A. Kramer. 2012. STIL is required for centriole duplication in human cells. *J Cell Sci*. 125:1353-1362.

Wang, W.J., R.K. Soni, K. Uryu, and M.F. Tsou. 2011. The conversion of centrioles to centrosomes: essential coupling of duplication with segregation. *J Cell Biol*. 193:727-739.

Watson, P.A., H.H. Hanauske-Abel, A. Flint, and M. Lalande. 1991. Mimosine reversibly arrests cell cycle progression at the G1-S phase border. *Cytometry*. 12:242-246.

White, D.E., D. Negorev, H. Peng, A.V. Ivanov, G.G. Maul, and F.J. Rauscher, 3rd. 2006. KAP1, a novel substrate for PIKK family members, colocalizes with numerous damage response factors at DNA lesions. *Cancer Res*. 66:11594-11599.

Wong, Y.L., J.V. Anzola, R.L. Davis, M. Yoon, A. Motamedi, A. Kroll, C.P. Seo, J.E. Hsia, S.K. Kim, J.W. Mitchell, B.J. Mitchell, A. Desai, T.C. Gahman, A.K. Shiau, and K. Oegema. 2015a. Cell biology. Reversible centriole depletion with an inhibitor of Polo-like kinase 4. *Science (New York, N.Y.)*. 348:1155-1160.

Wong, Y.L., J.V. Anzola, R.L. Davis, M. Yoon, A. Motamedi, A. Kroll, C.P. Seo, J.E. Hsia, S.K. Kim, J.W. Mitchell, B.J. Mitchell, A. Desai, T.C. Gahman, A.K. Shiau, and K. Oegema. 2015b. Reversible centriole depletion with an inhibitor of Polo-like kinase 4. *Science*. 10.1126/science.aaa5111.

Wong, Y.L., J.V. Anzola, R.L. Davis, M. Yoon, A. Motamedi, A. Kroll, C.P. Seo, J.E. Hsia, S.K. Kim, J.W. Mitchell, B.J. Mitchell, A. Desai, T.C. Gahman, A.K. Shiau, and K. Oegema.

2015c. Reversible centriole depletion with an inhibitor of Polo-like kinase 4. *Science*. 348:1155-1160.
Woodruff, J.B., O. Wueseke, and A.A. Hyman. 2014. Pericentriolar material structure and dynamics. *Philosophical Transactions of the Royal Society B: Biological Sciences*. 369.
Yang, R., and Jessica L. Feldman. 2015. SPD-2/CEP192 and CDK Are Limiting for Microtubule-Organizing Center Function at the Centrosome. *Current Biology*. 25:1924-1931.
Yu, J., Y. Zheng, J. Dong, S. Klusza, W.M. Deng, and D. Pan. 2010. Kibra functions as a tumor suppressor protein that regulates Hippo signaling in conjunction with Merlin and Expanded. *Dev Cell*. 18:288-299.
Zhang, D., K. Zaugg, T.W. Mak, and S.J. Elledge. 2006. A role for the deubiquitinating enzyme USP28 in control of the DNA-damage response. *Cell*. 126:529-542.
Ziv, Y., D. Bielopolski, Y. Galanty, C. Lukas, Y. Taya, D.C. Schultz, J. Lukas, S. Bekker-Jensen, J. Bartek, and Y. Shiloh. 2006. Chromatin relaxation in response to DNA double-strand breaks is modulated by a novel ATM- and KAP-1 dependent pathway. *Nat Cell Biol*. 8:870-876.

Curriculum Vitae

Bram G. Lambrus

Contact Information
- **email:** elambrus@gmail.com
- **phone:** 405-742-7961
- **address:** 13 N Collington Avenue, Baltimore, MD 21231

EDUCATION

Johns Hopkins School of Medicine // Baltimore, MD **2013-2019**
- Ph.D. Candidate in Department of Molecular Biology and Genetics
- GRE: Quantitative 800/800, Verbal 720/800 (98th percentile)

University of Illinois at Urbana-Champaign (UIUC) // Urbana, IL **2008-2011**
- B.S. in Biochemistry, Minor in Chemistry
- GPA: 3.98/4.0, Graduated *summa cum laude*

RESEARCH EXPERIENCE

Graduate Research Assistant, Johns Hopkins School of Medicine 2013-present
- Optimized and performed cutting-edge genome-wide CRISPR/cas9 knockout screen in human cells, resulting in the identification of 3 critical factors that enable cells to sense problems in cell division – the first known components of the "mitotic surveillance pathway"
- Demonstrated strong organizational and writing skills through a successful NSF fellowship application, two first-author papers, a first-author review, and a co-first-author methods chapter
- Presented research regularly at group meetings, departmental seminars, and both regional and national conferences
- Mentored 2 rotation and 3 undergraduate students, leading 2 students to earn summer undergraduate research fellowships
- Initiated collaboration with cell-sorting lab that resulted in savings of >$3000 and tripled efficiency of procedure
- Supervised lab data management and adoption of digital tools, resulting in 5-fold increase in image analysis efficiency

Research Specialist, University of Illinois at Urbana-Champaign **2012-2013**
- Responsible for schistosome parasite harvesting and coordinating a targeted screen to identify druggable vulnerabilities
- Tested new transgenics methods in an experimentally intractable organism

Research Specialist, Princeton University **2011-2012**
- Member of interdisciplinary team, teaching non-biology peers the principles of molecular biology to overcome experimental issues
- Supervised two undergraduate students on their research project, culminating in successful completion of semester reports

Undergraduate Researcher, University of Illinois at Urbana-Champaign **2008-2011**
- Trained in the prestigious lab of Phillip Newmark (Howard Hughes Medical Institute) for 6 semesters and 3 summers
- Studies on eye regeneration resulted in 1 first-author paper, and award for most outstanding senior thesis
- Collaborated with behavioral lab in the Engineering Dept. to develop automated video-analytics that contributed to publication

LEADERSHIP EXPERIENCE

Workshop Instructor, Johns Hopkins School of Medicine (SOM) **2016-2018**
- Initiated and developed interactive workshops to teach Adobe Illustrator skills, recruiting TAs and organizing two sessions to teach 60+ attendees, who have applied the experience to produce significantly improved diagrams and data figures
- Recruited and trained new student instructors to co-teach and run future interactive workshops
- Currently organizing expansion of the workshop to be offered across Johns Hopkins graduate programs

Teaching Assistant (Introductory Genetics), Johns Hopkins SOM **2016-2017**
- Developed lecture, homework, and exam material for Introductory Genetics course, and guided problem-solving sessions in class
- Wrote, illustrated, and recorded webcasts from scratch, in the shift towards developing digital material for the course

Graduate Policy Committee Student Representative, Johns Hopkins SOM **2015-2017**
- Spearheaded search committee of 8 members to select and recruit distinguished keynote speaker for program retreat
- Co-organized retirement celebration of 12-year program director, resulting in attendance of 120+ students, faculty, and alumni

Teaching Assistant (Organic Chemistry), University of Illinois (UIUC) **2009-2010**
- Led weekly discussion sections, and organized and presented exam review sessions attended by 200+ students

- Developed the course by evaluating class strengths and weaknesses in weekly meetings with other course leaders

SELECTED AWARDS & HONORS

2019 Weintraub Graduate Student Award
2018 DiMaio Departmental Award for Distinguished Graduate Student
2017 Journal of Cell Biology - Alan Hall Travel Award
2016 Johns Hopkins Young Investigator's Award
2014 National Science Foundation Graduate Research Fellows Program Fellowship
2013 Kelly Award for Distinguished First Year Graduate Student
2011 Bronze Tablet Honors *(awarded to top 3% of graduates – highest UIUC honor)*
2011 Thomas O. Sidebottom Award for Most Outstanding Senior Thesis
2011 Highest Departmental Distinction
2007 Oklahoma Academic All-State Award *(top 100 students selected out of 544 nominees)*
2007 National Merit Scholar Finalist *(awarded to top 0.5% of students)*

PUBLICATIONS

Lambrus BG, Moyer TC, Holland AJ. (2018) Applying the auxin-inducible degradation system for rapid protein depletion in mammalian cells. ***Methods in Cell Biology***. doi: 10.1016/bs.mcb.2018.03.004.

Lambrus BG, Holland AJ. (2017) A New Mode of Mitotic Surveillance. ***Trends in Cell Biology***. doi: 10.1016/j.tcb.2017.01.004. Cover image.

Lambrus BG*, Daggubati V*, Uetake Y, Scott PM, Clutario KM, Sluder G, Holland AJ. (2016) A USP28–53BP1–p53–p21 signaling axis arrests growth after centrosome loss or prolonged mitosis. ***Journal of Cell Biology***. doi: 10.1083/jcb.201604054. (*Co-first authors). Cover image. **Previewed in *Nature Reviews Molecular Cell Biology*, "Signaling to cell cycle arrest"

Lambrus BG, Uetake Y, Clutario KM, Daggubati V, Snyder M, Sluder G, Holland AJ. (2015) p53 protects against genome instability following centriole duplication failure. ***Journal of Cell Biology***. doi: 10.1083/jcb.201502089. **Highlighted in the JCB 2017 Special Collection on Cell Biology in Cancer

Moyer TC, Clutario KM, **Lambrus BG**, Daggubati V, Holland AJ. (2015) STIL binding to Plk4 activates kinase activity to promote centriole duplication. ***Journal of Cell Biology***. doi: 10.1083/jcb.201502088.

Lambrus BG, Cochet-Escartin O, Collins EM, Newmark PA, Collins JJ. (2015) Tryptophan hydroxylase is required for eye pigmentation in planarian *Schmidtea mediterranea*. ***PLoS One***. doi: 10.1371/journal.pone.0127074.

Wang JT, Smith J, Chen BC, Schmidt H, Rasoloson D, Paix A, **Lambrus BG**, Calidas D, Betzig E, Seydoux G. (2014) Regulation of RNA granule dynamics by phosphorylation of serine-rich, intrinsically disordered proteins in C. elegans. ***Elife***. doi: 10.7554/eLife.04591.

Collins JJ, Wang B, **Lambrus BG**, Tharp M, Iyer H, Newmark PA. (2013) Neoblast-like somatic stem cells in the human parasite Schistosoma mansoni. ***Nature***. doi: 10.1038/nature11924.

Collins JJ, Hou X, Romanova EV, **Lambrus BG**, Miller CM, Saberi A., Sweedler JV, Newmark PA. (2010) Genome-Wide Analyses Reveal a Role for Peptide Hormones in Planarian Germline Development. ***PLoS Biology***. doi: 10.1371/journal.pbio.1000509.

PRESENTATIONS

A new mode of mitotic surveillance: centrosome loss and prolonged mitosis trigger cell cycle arrest. ***Mid-Atlantic Mitosis Meeting***. April 2017. (Presentation)

Identification of a "centrosome surveillance pathway. ***National Cancer Institute Centrosome Meeting***. January 2017. (Presentation)

A new mode of mitotic surveillance: centrosome loss and prolonged mitosis trigger cell cycle arrest. ***American Society for Cell Biology***. December 2016. (Poster)

Centrosome loss activates a protective p53-dependent cell cycle arrest. ***BCMB program retreat***. October 2015. (Presentation)

Characterizing centriole biogenesis with auxin-inducible degradation of Plk4. ***National Cancer Institute Centrosome Meeting***. March 2015. (Presentation)

Characterizing centriole biogenesis with auxin-inducible degradation of Plk4. ***NIH Mitosis Meeting***. January 2015. (Presentation)

Characterizing centriole biogenesis with auxin-inducible degradation of Plk4. ***American Society for Cell Biology***. December 2015. (Poster)

Tryptophan hydroxylase is required for proper eye function in planarians. ***Princeton University, Integrated Science Shorts Seminar***. May 2012. (Presentation)